Characteristics and Genesis of Gold Mineralization in the Salu Bulo Prospect, Sulawesi, Indonesia

インドネシア、スラウエシ島、Salu Bulo 鉱徴地における金鉱化作用の特徴と成因

Muhammad Zain Tuakia

ID No.9514252

Department of Geosciences, Geotechnology, and Materials Engineering for Resources,

Graduate School of Engineering and Resource Science,

Akita University, JAPAN

2019

Characteristics and Genesis of Gold Mineralization in the Salu Bulo Prospect, Sulawesi, Indonesia

Muhammad Zain Tuakia, ID # 9514252

Abstract

Several significant gold deposits hosted in metamorphic rocks have been discovered in Sulawesi, Indonesia, namely Paboya, Awak Mas, Palopo and Bombana. The Salu Bulo prospect is one of the gold prospects in the Awak Mas project in the central part of the Western Metallogenic Province, Sulawesi, Indonesia. The four domains in the Salu Bulo prospect (Biwa, Lelating, Bandoli and Freddie) has been explored by Placer Dome Inc., in 1999 and One Asia Resource Ltd., in 2011 to 2013 through 132 drilled holes with an average length of 100 m. The resource was measured and indicated about 5.6 million tons at 2.2 g/t Au with a cut-off grade at 0.5 g/t Au as well as an additional 0.5 million tons at 1.1 g/t Au as an inferred resource, reported by Tetra Tech in 2013. The Salu Bulo prospect is hosted by the cover sequence of Latimojong Metamorphic Complex. Within the prospect, the Latimojong Metamorphic Complex consists of meta-dark (graphitic), green (chloritic) and red (hematitic) mudstone, siltstone, sandstone and intercalated meta-volcanic and volcaniclastic rocks along with phyllite. The ore bodies in the Salu Bulo prospect are north-south trending and dipping steeply eastward, approximately three meters thick which are associated with veins, stockwork and breccias with an orientation sub-parallel and discordant to the foliation of the host rocks. The veins can be classified in three stages namely early, main and late stages and gold mineralization is related to the main stage. The veins formed during the main stage are composed of quartz, carbonate (mainly ankerite) and albite. The breccia formed mainly

during the main stage of mineralization. The breccia is associated with quartz, carbonate (mainly ankerite), albite and pyrite.

Sulfide minerals, native gold and electrum are lesser abundant or absent in the veins and stockwork. High grade gold ores in the Salu Bulo prospect are accompanied with intense alteration along the main stage veins and breccia. Alteration mineral assemblage includes ankerite ± calcite, quartz, albite and pyrite along with minor sericite. Pyrite is the most abundant sulfide mineral, which is spatially related to gold (<2-42 μm in size). It is more abundant as dissemination in the altered host rocks than those in veins, suggesting that water-rock interaction played a role to precipitate pyrite and gold in the Salu Bulo prospect. Pyrite shows several different morphologies and textures: fine-grained, porous, deformed and massive pyrites. Lesser amounts of tennantite-tetrahedrite, chalcopyrite, bornite, galena, hematite and rutile are also present as inclusions in pyrites, and as discrete disseminated minerals in altered host rocks, veinlets and matrix of breccia. Covellite and chalcocite occur on the rim of some chalcopyrite.

Correlation coefficients of whole-rock Ag, Ni, Mo and Na contents to whole-rock Au content are above 0.5 indicating that they are strongly correlated with gold. The Mo, Ni, Sb, Hg, Se, Sr and W contents are relatively elevated in altered host rocks and ores than in unaltered host rocks, whereas the Cs, Rb and V contents are relatively depleted. The K_2O content is depleted in hydrothermally altered host rocks and ores indicating absence of potassic alteration and decomposition of K-bearing mineral in host rocks during hydrothermal alteration. Various elevated and depleted of MgO, Fe_2O_3, Al_2O_3 and MnO contents in hydrothermally altered host rocks and ores are related to inherited host rocks composition (i.e. mineral composition). PAAS normalized REE plots of unaltered and altered host rocks and ores are relatively similar patterns which are depleted of LREE and sub-horizontal HREE with various Eu positive anomalous (Eu/Eu* varying from 0.1 to 0.9).

ΣREE of unaltered host rocks is relatively similar and higher than hydrothermally altered host rocks and ore indicating evidence for mobility and fractionation of REE during hydrothermal alteration. Gold was introduced as electrum and native gold with Au / (Au + Ag) ratio ranging from 66.2 to 78.5 atomic % and from 81.4 to 82.3 atomic %, respectively as fracture filling and inclusion in pyrites. The Ni and Co concentrations of pyrite are high, 10 - 7780 ppm and 390 - 2710 ppm, respectively, in edges, cores and rims of pyrite with Co/Ni ratio of pyrite ranging from 0.09 to 63.

Fluid inclusions in quartz in the veins of the main stage and the matrix of breccia are mainly two-phase liquid-rich inclusions with minor two-phase vapor-rich and single-phase liquid or vapor inclusions. CO_2 and N_2 are detected in the fluid inclusions by Laser Raman microspectrometry. Raman spectrum of CO_2 clearly shows strong bands at ~ 1285 cm-1 ($v1$) cm−1 and ~ 1388 cm−1 ($2v2$) in mineralized vein and at ~ 1282 cm-1 ($v1$) and ~ 1385 cm−1 ($2v2$) in the matrix of breccia, N_2 and graphite at ~ 2328 cm−1 and ~ 1617 cm−1 respectively in mineralized vein and at ~ 2327 cm−1 and ~ 1606 cm−1 respectively in matrix of breccia. Homogenization temperature (Th) of fluid inclusions in the veins ranges from 132 to 357 °C and that in the matrix of breccia ranges from 148 to 368 °C, which homogenized into a liquid phase. Salinity of fluid ranges from 3.5 to 8.0 wt% (average 6.3 wt%) NaCl equivalent in the veins and from 3.9 to 8.5 wt% (average 6.0 wt%) NaCl equivalent in the matrix of breccia. The wide range of homogenization temperature of fluid inclusions and the co-existence of two-phase liquid-rich and two-phase vapor-rich inclusions suggest boiling of fluid when they were trapped. The trapping temperature was 190 to 210 ^{o}C. Fluid boiling probably occurred when the fluid was trapped at approximately 120 to 190 meters below the paleo water table. $\delta^{18}O_{SMOW}$ values of fluid, +5.8 ‰ and +7.6 ‰ calculated from $\delta^{18}O_{SMOW}$ of quartz (+17.2 ‰ and +19 ‰) at 205^{o}C from the main stage vein indicate oxygen isotopic exchange with wall rocks during deep circulation. $\delta^{34}S_{CDT}$ of pyrite narrowly ranges from -2.0 to +3.4 ‰

suggesting a single source of sulfur. Gold mineralization in the Salu Bulo prospect occurred in an epithermal condition, after the metamorphism of the Latimojong Metamorphic Complex and emplacement of Palopo Granite or Enrekang Volcanic Series in the Late Miocene to Pliocene. It was formed at relatively shallow depth from CO_2-bearing sodic mineralizing fluid with low to moderate salinity (3.0 - 8.5 wt% NaCl equiv.). Temperature and pressure of ore formation range from 190 to 210 °C and 1.2 to 1.9 MPa, respectively.

ACKNOWLEDMENTS

First of all, I am very thankful to Allah Almighty who guided me to this opportunity. I would like to express my humble gratitude to my supervisor Prof. Akira Imai and Co-supervisor Dr. Ryohei Takahashi for guidance and discussion during my study, as well as Prof. Tsukasa Ohba as later my supervisor for administration arrangement. I extend my thanks to Dr. Hinako Sato and Dr. Takuya Echigo for their support to the analyses and Prof. Toshio Mizuta for constructive discussion. I thank to Japanese Government (MONBUKAGAKUSHO: MEXT) for providing me the scholarship and Akita University for acceptance my admission. Thank to Leading Program, Akita University for enrollment and financial support and PT Masmindo Dwi Area (One Asia Resources Ltd.) for providing data and accommodation during the field works. I am grateful to the Department of Geological Engineering, Hasanuddin University for their support during the field works.

Table of Contents

Page No.

Chapter 1

Chapter 2

Chapter 3

Chapter 4

Chapter 5

Ore Characteristics…………………………………………………………….. 37

Chapter 6

Alteration, Mineralization and Paragenesis…………………………………..……... 45

Chapter 7

Whole-rock Geochemistry and Mineral Chemistry…………………………………... 53

Chapter 8

Chapter 9

Chapter 10

List of Figures

List of Tables

Tables Page No.

List of Appendices

List of Units and Abbreviations

g/t	gramm per ton
g/cm^3	gram per centimeter cubic
m	meter
%	percent
‰	permil
Ma	mega annum (period of one million year)
^{o}C	degree celcius
kbar	kilobar
km	kilometer
m	meter
mm	milimeter
mol%	molarity
wt%	weight percent
ppm	part per million
Δ	delta
2θ	two tetta
α	alpha
Ǻ	angstrom
kV	kilovolt
mA	megaampere
nA	nannoampere
μA	microampere
s	second
n	number/quantity
(r)	correlation coefficient

nd	not detected
dl	detection limit

CHAPTER I: INTRODUCTION

1.1 Background

Several significant gold deposits hosted in metamorphic rocks have been discovered in Sulawesi, Indonesia, namely Paboya, Awak Mas, Palopo and Bombana. Previous studies suggest that these deposits vary in type of mineralization. The gold mineralization in Palopo was suggested to be related to granitic intrusion (Van Leeuwen & Pieters, 2011), that in Poboya is a low-sulfidation epithermal gold deposit (Wajdi et al., 2011), and that in Awak Mas was previously classified as mesothermal or orogenic-type (i.e., Archibald et al., 1996; White, 1999; Querubin & Walters 2011; Idrus et al., 2015; Harjanto et al., 2016; Hakim et al., 2018). In addition, the Bombana gold prospect which was reported as a placer gold deposit hosted in Pompangeo Complex and Langkowala Formation (Idrus et al., 2010).

The Awak Mas project consists of the Awak Mas, the Salu Bulo and the Tarra prospects. Available literature in the area focused on the Awak Mas prospect (Archibald et al., 1996; Smillie, 1996; Querubin & Walters 2011; Idrus et al., 2015; Harjanto et al., 2016; Harjanto, 2017; Hakim, 2017; Hakim et al., 2018), with few studies covering the Salu Bulo prospect (White, 1999; Hakim & Melcher, 2016; Hakim, 2017; Hakim et al., 2018). The latter has an estimated resource of 5.6 million tons at 2.2 g/t Au, with an additional 0.5 million tons of inferred resource at 1.1 g/t Au (Tetra Tech, 2013) (Table 1). The four domains in the Salu Bulo prospect (Biwa, Lelating, Bandoli and Freddie) have been explored by Placer Dome Inc., in 1999 and One Asia Resource Ltd., in 2011 to 2013 through 132 drilled holes with average length of 100 m. Despite more and detail information have been provided some questions are still considerable uncertainty particularly in origin of fluid and how the fluid migrates from depth level to form gold mineralization in the Awak Mas project. This study aims to further contribute to the understanding of the Salu Bulo prospect in terms of the source of the ore-forming fluids and gold precipitation mechanism.

1.2 Aims, objectives and significance of this study

The aims of this study are to define the type of the deposit and understand geology, characteristics and genesis of gold mineralization in the Salu Bulo prospect specifically. This study presents petrography of ores and host rocks, microthermometry and gas composition of fluid inclusions in the main stage veins and matrix breccia, bulk chemical composition of ores and host rocks, mineral chemistry of gold minerals and pyrite, and oxygen and sulfur isotopes, in order to:

1. Describe the geology of the study area;
2. Characterize ores and deposit type:
3. Document hydrothermal alteration, ore mineralogy and paragenesis;
4. Characterize ore-forming fluid and condition;
5. Describe gold precipitation mechanism;
6. Define deposit type; and
7. Establish a genetic model for gold mineralization in the Salu Bulo prospect.

This study will help in effective exploration method and target to find new resources in Indonesia; in understanding and contribution of characteristics and ore genesis of gold deposits in metamorphic terrain; and in understanding of geological setting of Sulawesi Island that related to gold mineralization.

1.3 Location, access and physiography

The study area is located at foothill of Latimojong Mountain in the Luwu District, South Sulawesi Province, Indonesia (Figs. 1, 2). The commercial air service can be used from Jakarta to reach Makassar, the capital city of South Sulawesi Province. The study area is about 412 km from Makassar driving toward northeast. It takes about 10 hours to arrive in the camp site from Makassar. The topography of the Awak Mas project ranges from 800 to 1,400 meters above sea level (Figs. 2). The highest level is the summit of Mount Rantemario, 3,478 meters above sea level, located in the western part of the Awak Mas project.

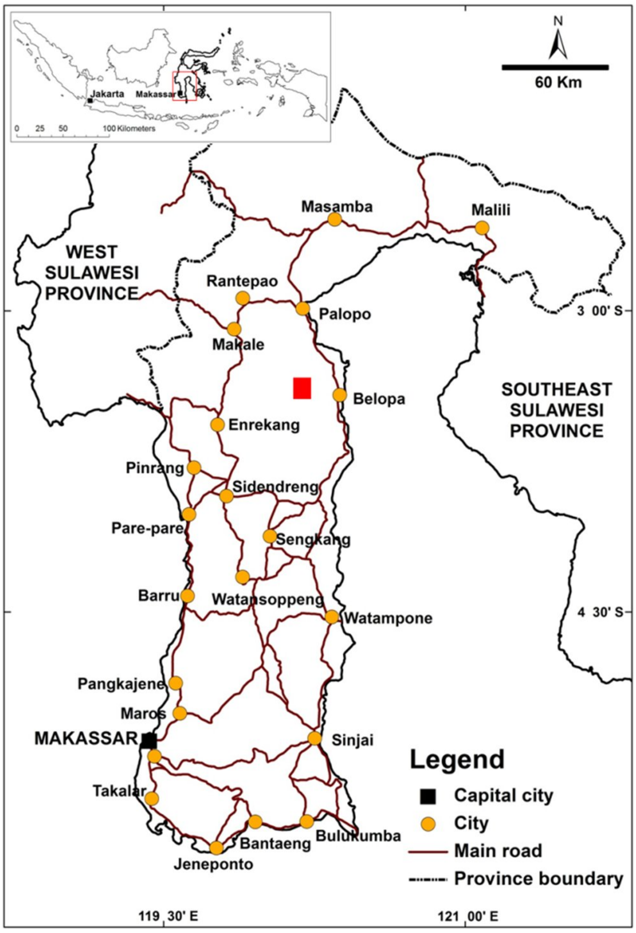

Figure 1. Location of study area (red square).

1.4 Organization of the thesis

The thesis is composed of 10 chapters. Chapter 1 is the outline of study background, aims and objectives of study and location of study area. Chapter 2 provides a background of regional geology and metallogenic province of Sulawesi. Chapter 3 describes methods and analytical techniques. Chapter 4 provides geology of the study area. Chapter 5 describes ore characteristics while the chapter 6 describes alteration, mineralogy and paragenesis. Chapter 7 provides the whole-rock geochemistry of the host rocks and ores and mineral chemistry of pyrite, native gold and electrum. Fluid inclusion and oxygen isotope in quartz in the veins of the main stage and sulfur isotope of pyrite from host rocks and ores are presented in Chapter 8. Chapter 9 is discussion on P-T condition, origin of mineralizing fluid, gold precipitation mechanism, genetic model and timing of gold mineralization and tectonic setting of the Salu Bulo prospect based on the data with some comparison with other deposits. And finally, chapter 10 provides conclusions of the study.

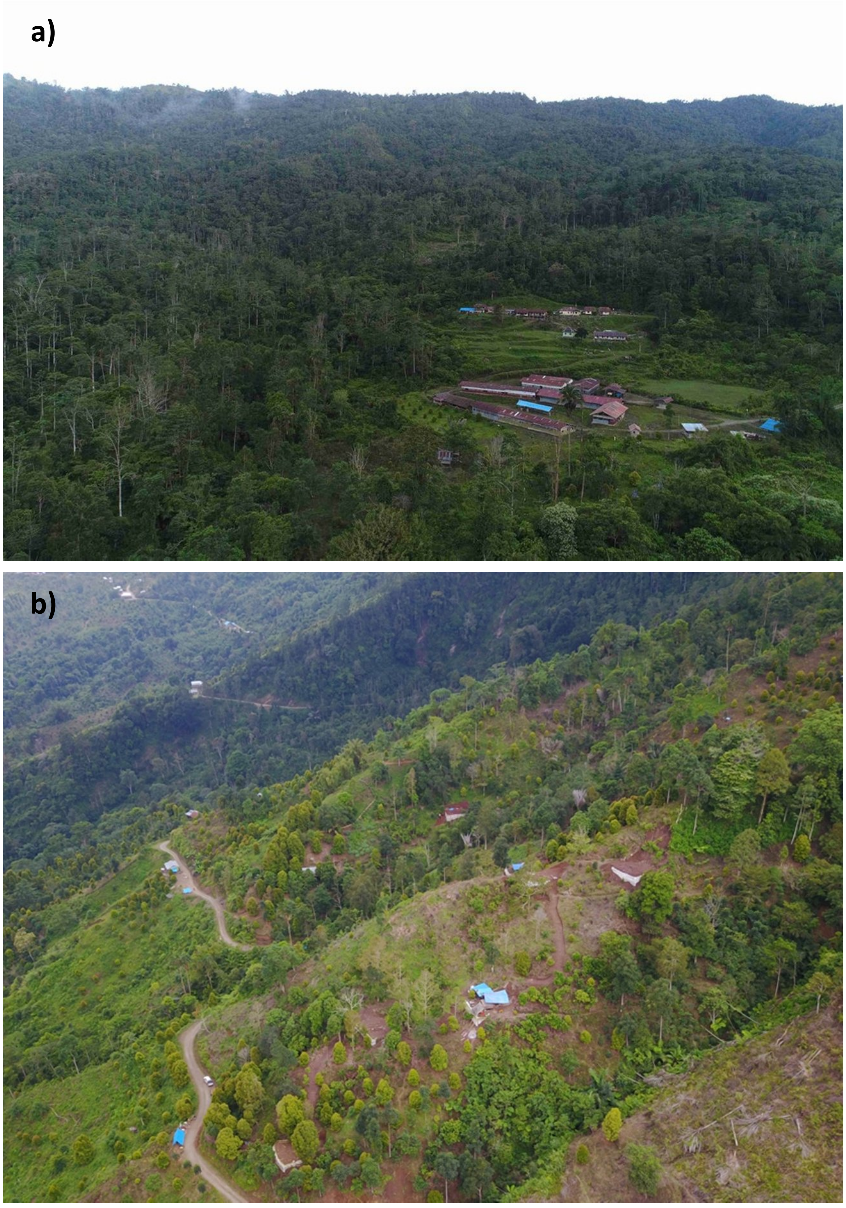

Figure 2. Photograph (a) of camp site of the Awak Mas project and (b) the Salu Bulo prospect, taken from high elevation (courtesy of PT Masmindo Dwi Area).

1.5 Previous works

Some previous studies have been done in the Awak Mas project during the exploration period by independent consultants and the company, and recently by academic staffs and some workers. Those were mainly focused on the Awak Mas prospect with lesser investigation in the Salu Bulo prospect. Early studies in 1990’s provided the geological overview of the Awak Mas project through surface and drill core observations and few petrography and XRD analyses (Archibald et al., 1996; Smillie, 1996; White, 1999). Late studies in 2000’s provided alteration and mineralogy, fluid characteristics and gold precipitation mechanism in the Awak Mas prospect with lesser studied in the Salu Bulo prospect (Querbin & Walters, 2011; Idrus et al., 2015; Harjanto et al., 2016; Hakim & Melcher, 2016; Harjanto, 2017; Hakim, 2017; Hakim et al., 2018).

1.6 Problems

Previous studies suggested that the type of gold deposit in the Awak Mas project is mesothermal or orogenic gold deposit based on 1) alteration and mineralogy of ore bodies that consist of albite, pyrite, silica and/or carbonate overprinted the ductile fabric of older basement lithologies in relatively late stage tectonic history; 2) formation temperature ranging from 175 to 350 °C in low salinity (i.e., 1.2-3 wt.% NaCl equiv.; 3) sulfur isotope values of pyrite ranging from +0.6 to +12.9 ‰ emphasizing the metamorphic character of the ore-forming fluid; 4) calculated oxygen isotope analysis of quartz veins yielded $\delta^{18}O$ values ranging from +17.9 to 20.6 ‰ suggesting that ore-forming fluid derived from metamorphic dewatering process; 5) gold occurs in pyrite as sub-microscopic inclusions and as fracture fillings of deformed pyrite with a gold fineness ranging from 925 to 935 and Au:Ag ratios between 12:1 and 14:1; 6) Br/Cl/I ratios of fluid halogen data appear to confirm the presence of a metamorphic fluid derived from original marine sediments with little or no magmatic signature; and 7) isothermal decompression during the retrogression stage mobilized large volumes of fluids to form gold mineralization in the Awak Mas project (i.e: Archibald et al., 1996; Smillie 1996; White, 1999; Querubin & Walters 2011; Idrus et al., 2015; Harjanto et al., 2016; Hakim & Melcher, 2016; Harjanto, 2017; Hakim, 2017; Hakim et al., 2018). No relationship between volcanic or magmatic activities and the deposits has been recognized so far. Not much detail study has described the characteristics of gold mineralization in the Salu Bulo prospect. However, several questions still remain from the previous studies to prove, i.e. the source of the ore-forming fluid and how the fluid migrated from a depth that still in debate

1.7 Exploration history

Originally partners in the Joint Venture of PT Masmindo Eka Sakti in the Awak Mas project were New Hope Consolidated Industries Pty. Ltd. and PT Asminco Bara Utama (Asminco). Reconnaissance surveys within Bajo River and Ulusalu area were initial exploration activities in the Awak Mas project. During 1996 to 1998, Masmindo continued exploration activities through sampling of infill and follow-up stream sediment, Wacka drill for soil, float and rock chip/channel.

In September 1998, Placer Dome entered into the Joint Venture in the Awak Mas project and acquired a 51% of interest. From September 1998 to June 1999, Placer Dome conducted geochemical surveys including trenching and surface traverse sampling and completed testing of diamond drilling in the Salu Bulo prospect through 30 drilled holes with 3,172 meters depth.

In December 2009, a new Joint Venture was started between Vista Gold and One Asia that allowed One Asia to acquire 60% of interest in PT Masmindo Dwi Area. Between 2011 and 2013, One Asia conducted resource definition drilling on a grid spacing of 50 m x 50 m with infill drilling on 25 m x 25 m grid spacing through 102 drilled holes with 9,738 meters long. Later the total 132 drilled holes were used for modeling and resource estimation of gold mineralization in the Salu Bulo prospect.

1.8 Resource/reserves

The original ore model was developed by Placer Dome in 1999 through 30 drilled holes. The model was later updated by One Asia by adding 102 drilled holes through resource definition drilling from 2011 to 2013. In 2013, Tetra Tech estimated the resource in the Salu Bulo prospect based on the latest model. The model was built by using the geological interpretation of vein, stockwork and breccia zones combined with assay data within Lelating, Biwa, Bandoli and Freddie domains.

Gold grade in the Salu Bulo prospect estimated using ordinary kriging (OK) within 4 m x 4 m x 4 m blocks. The resource categories were classified as measured and indicated and additional inferred based on drilling density and geostatisitical analysis of assay data concerning the mineralized wireframes and kriging error. Table 1 presents summary of resources in the Salu Bulo prospect at 0.5 g/t Au (Tetra Tech, 2013).

Table 1. Summary resources of Salu Bulo prospect at 0.5 g/t Au cut off (Tetra Tech, 2013).

Category	Tonnes (million)	Average grade (g/t Au)	Metals (million Oz Au)
Measured	2.2	2.3	0.17
Indicated	3.4	2.1	0.22
Total	5.6	2.2	0.39
Inferred	0.5	1.1	0.02

CHAPTER II: GEOLOGICAL SETTING AND METALLOGENY OF SULAWESI

2.1 Geology of Sulawesi

Regionally, Indonesia archipelago is divided into two regions namely western and eastern regions which are separated by Makassar Strait (Fig. 3). Western region, known as Sundaland consists of three big islands namely Sumatera, Java and Borneo Islands, whereas eastern region consists of two big islands namely Sulawesi and western part of New Guinea Islands, small islands namely Sumbawa, Flores, Banda, Buru, Seram and Halmahera Islands and micro-continent of Banggai-Sula and Tukang Besi (Figs. 3, 4).

Sulawesi Island is one of the five major islands of Indonesia situated in the central part of the Indonesian archipelago. The island was formed by the interaction and convergence among the Indo-Australian, Eurasian, Pacific and the Philippine Sea Plates between the Late Mesozoic and Cenozoic (Katili, 1978; Metcalfe, 2011; Hennig et al., 2016) (Fig. 3). During the time, three major tectonic events occurred to form the island namely, Early Cretaceous subduction complexes exposed in Bantimala Complex (Hamilton 1979); Mid-Oligocene collision event which is represented by blueschist and ophiolite complexes in Eastern Sulawesi (East and Southeast Arms) (Katili, 1978); and Lower Miocene calc-alkaline magmatic rocks in the North Arm of Sulawesi (Kavaleries et al., 1992) (Fig. 4). The complex geological history of the island is expressed by its four arms namely, North, South, East and Southeast Arms (Katili, 1978; Hamilton, 1979) (Fig. 4) and divided into Western Arc and Eastern Arc (Hamilton, 1979). The Western Arc consists of the North and South Arms and western part of central Sulawesi while the Eastern Arc consists of the East and Southeast Arms and the eastern part of central Sulawesi. In the Western Arc, Cretaceous subduction complexes are overlain by sediments deposited in an outer-arc basin which overlain by upper

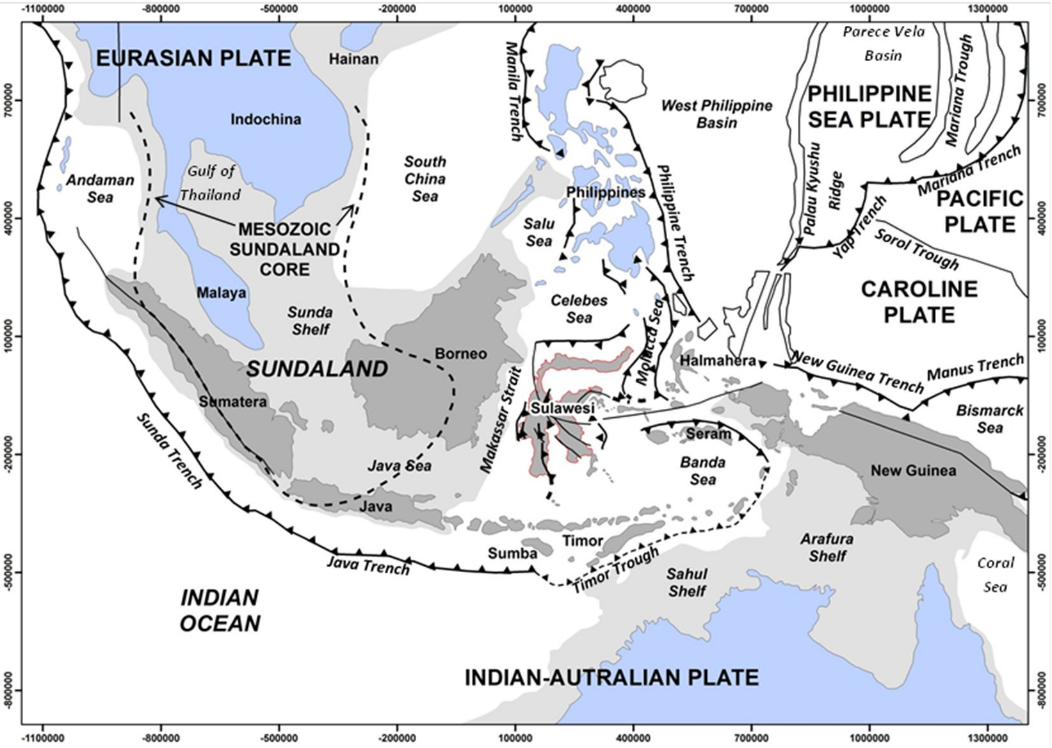

Figure 3. Tectonic setting of Indonesia (Modified from Hall, 2002).

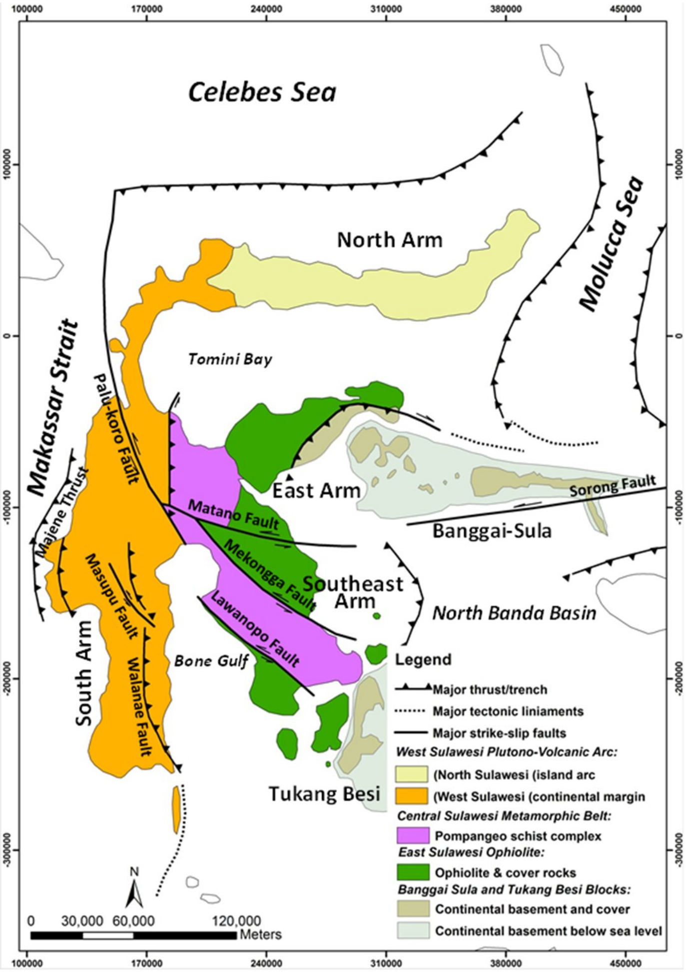

Figure 4. Tectonic setting of Sulawesi Island (modified from Jaya & Nishikawa, 2013).

Paleogene continental-shelf strata and later in turn by Neogene sedimentary and volcanic rocks and are intruded by Neogene granitic rocks (Hamilton, 1979). The Eastern Arc consists of fragments of ophiolites and of subduction complexes and latter likely becoming in general younger eastward to a limiting age of approximately Late Miocene (Hamilton, 1979).

2.2 Metallogeny of Sulawesi

Occurrences of mineral resources are mainly related to geological setting and the rock association of the region. The situation of Indonesia in the triple junction of three major plates, namely Indo-Australian, Pacific and Eurasian Plates gives more complexity of tectonic setting and variation of lithology. These endow Indonesia as one of the countries with big resource and reserve of mineral deposits, i.e., copper, gold, nickel, iron, tin, aluminum, manganese, zinc, etc (Fig. 5). All of the mineral deposits are distributed almost in all islands and related to Neogene magmatic arc and collision, pre-Tertiary intrusive rocks and ophiolite.

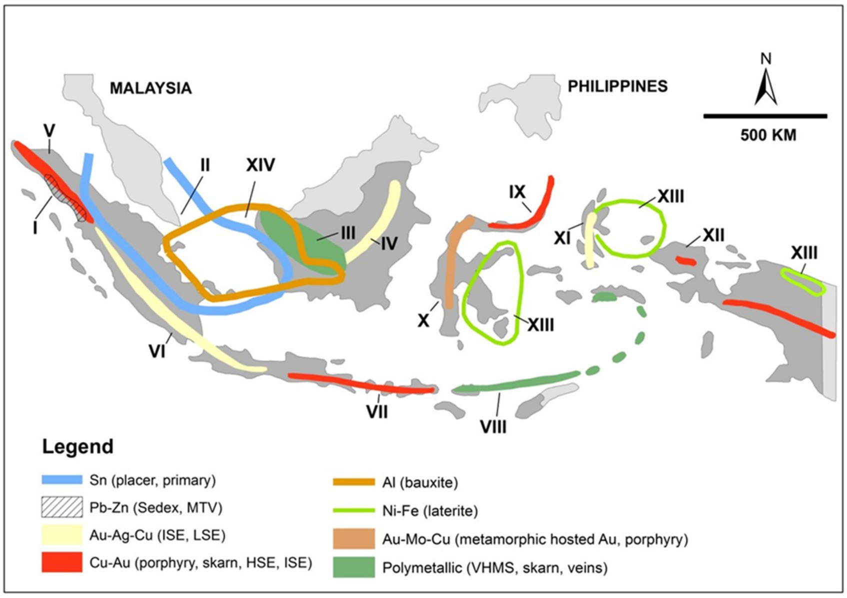

Remarks: I = Northern Sumatra Zn-Pb province; II = Western Indonesia Sn province; III = Central-West Kalimantan polymetallic province; IV = Central Kalimantan Au-Ag-Cu province; V = NW Sunda Arc Cu-Au province; VI = Central Sunda Arc Au-Ag province; VII = East Sunda Arc Cu-Au province; VIII = Banda Arc polymetallic province; IX = Northern Sulawesi Au-Cu province; X = Western Sulawesi Au-Mo-Cu province; XI = North Moluccas Au-Ag-Cu province; XII = Papua Cu-Au province; XIII = Eastern Indonesia Ni-Fe province; XIV = Western Indonesia Bauxite province.

Figure 5. Map of metallogenic province of Indonesia (Modified from Van Leeuwen, 2018).

Epithermal is the most contributors for mineral resources in Indonesia followed by placer deposits. Nevertheless, the big resources and reserves in million tonnages are coming from aluminum, copper, nickel and iron. The mineral resource in Indonesia is still improving and will be increased by the identification of new mineral deposits. From all islands of Indonesia, the potential distribution of mineral deposit in Sulawesi and Nusa Tenggara were spread evenly suggests that those islands give more opportunity for exploration targets.

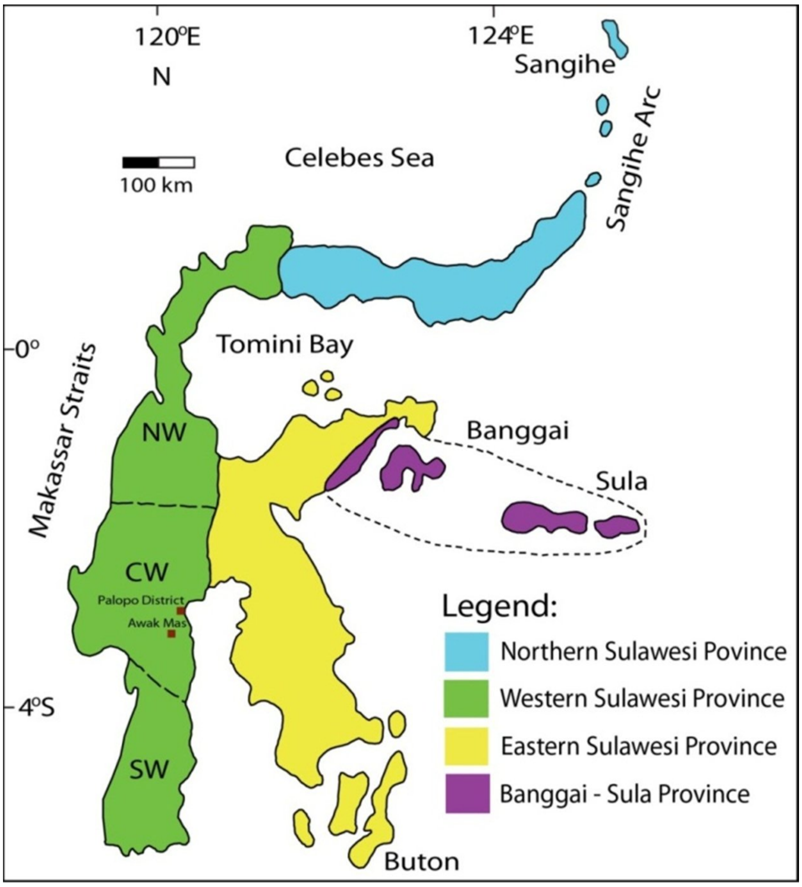

Figure 6. Geological-metallogenic province map of Sulawesi Island (Modified from Van Leeuwen & Pieters, 2011).

Van Leeuwen and Pieters (2011) and Idrus et al. (2011) divided Sulawesi Island into four geological-metallogenic provinces namely northern, western and eastern Sulawesi provinces, in addition to Banggai-Sula province (Fig. 6). Among the others, northern Sulawesi province appears to host numerous mineral deposits (Van Leeuwen & Pieters, 2011; Idrus et al., 2011). Several styles of mineralization were reported in this island, namely porphyry Cu-Au±Mo, high-, intermediate-, and low-sulfidation epithermal Au-Ag, Carlinstyle sediment-hosted Au, intrusion-related Au±base metals, skarn, Kuroko-type volcanogenic massive sulfide (VMS), Ni and Fe laterite deposits and uncertain gold mineralization hosted by metamorphic and post-orogenic sedimentary rocks (Van Leeuwen & Pieters, 2011; Idrus et al., 2011). In western Sulawesi province, several mineralization styles are present namely porphyry Mo, porphyry Cu±Mo, intrusion-related (?) Au and base metal±Au and volcanogenic massive sulfide (VMS) (Table 2, Fig. 7), hosted in Late Cenozoic high-K calc-alkaline to ultrapotassic igneous suites overlying a series of Early Cenozoic sedimentary rocks and subordinate calc-alkaline volcanic rocks deposited on a basement of metamorphic complexes and Late Cretaceous flysch deposits (Van Leeuwen & Pieters, 2011).

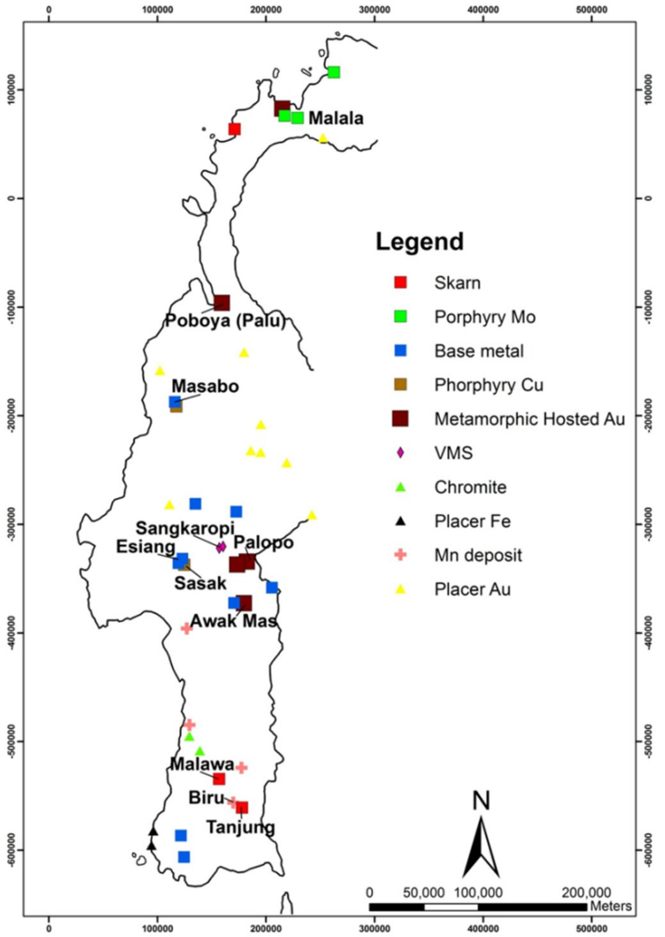

Figure 7. Distribution of mineral resources in the western Sulawesi province (Van Leeuwen & Pieters, 2011).

Table 2. Summary of mineralization styles in western Sulawesi province (Van Leeuwen & Pieters, 2011).

Deposit name	Mineralization style	Deposit style	Host rocks	Ag:Au ratio	Age (Ma)	Resources	Ore minerals	Alteration mineral assemblages
Malala	porphyry Mo	Qz-K-Fsp veins	quartz monzonite		4 Ma	100 Mt @ 0.14% MoS_2	Mo-Mag-Py-Sph-Gn-Ccp	1) Qz-Bt-K-Fsp 2) Cb-Ser/Ilt-Chl
Sasak	porphyry Cu-Au	1) disseminated Py and Ccp 2) Qz-K-Fsp-sulfide veins	monzonite stocks & dykes; breccia		Late Miocene		Py-Ccp-Bn-Mag	1) Bt-Mag 2) Ser-Ilt-Chl
Masabo	intrusion-related Au	1) disseminated ore 2) Qz veins, micro-fractures	syenite dykes; metabasalt		Late Miocene		Py-Ccp-Po	1) Act-Ab 2) Bt-Mag
Awak Mas	intrusion-related Au	Qz-Ab-Cb veins, partly sheeted, stockwork and breccia	meta-sedimentary rocks	<1	Pliocene (?)	41.7 Mt @ 1.23 g/t Au (2004) 20.4 Mt @ 0.82 g/t Au (2011)	Py (-Ccp-Sph)	Ab-Cb
Mangkaluku	intrusion-related Au	Qz-Cb veins	meta-sedimentary rocks; quartz monzonite	<3	Pliocene		electrum; Py-Apy (-Arg-Ccp-Cov)	1) K-Fsp-Bt-Act-Qz 2) Qz-Chl-Ser/Ilt 3) Qz-Chl-Ep-Act
Poboya	low-sulfidation	Qz-Cb veins	meta-monzonite, gneiss, schist	<1	Pliocene	18 Mt @ 3.4 g/t Au	Py	nearby zone of Kln-Dck-Qz-Alu
Esang	intrusion-related Au	Qz-Cb veins	meta-sedimentary rocks				Py, arsenian Py-Po-Ccp	Qz-Ser/Ilt-Py

Abbreviations: Act (actinolite); Alu (alunite); Ab (albite); Apy (arsenopyrite); Bn (bornite); Bt (biotite); Cb (carbonate mineral) Chl (chlorite); Cov (covellite); Ccp (chalcopyrite); ck (dickite); Ep (epidote); Gn (galena); Ilt (illite); Kln (kaolinite); K-Fsp (k-feldspar); Mag (magnetite); Mo (molybdenite); Py (pyrite); Po (pyrrhotite); Qz (quartz); Ser (sericite); Sph (sphalerite).

2.3 Regional geology

2.3.1 Latimojong region

In the South Arm, the Awak Mas project is located in the Latimojong Mountain Region (Figs. 8, 9). The deposits are hosted by Early Cretaceous (?) Latimojong Formation which is recently redefined as Latimojong Metamorphic Complex (White et al., 2017) (Figs. 8, 9). The complex is an accretionary complex consisting of low- to high-grade metamorphic rocks derived from alternating siliciclastic, calcareous and volcanic rocks (Fig. 10). These metamorphic rocks are tectonically mixed with cherts and ophiolitic rocks (Susilo, 1998; White et al., 2017). The Latimojong Metamorphic Complex was assumed to be equivalent to the early Late Cretaceous medium-high grade metamorphic rocks exposed in the Bantimala and Barru areas (White et al., 2017) (Fig. 8).

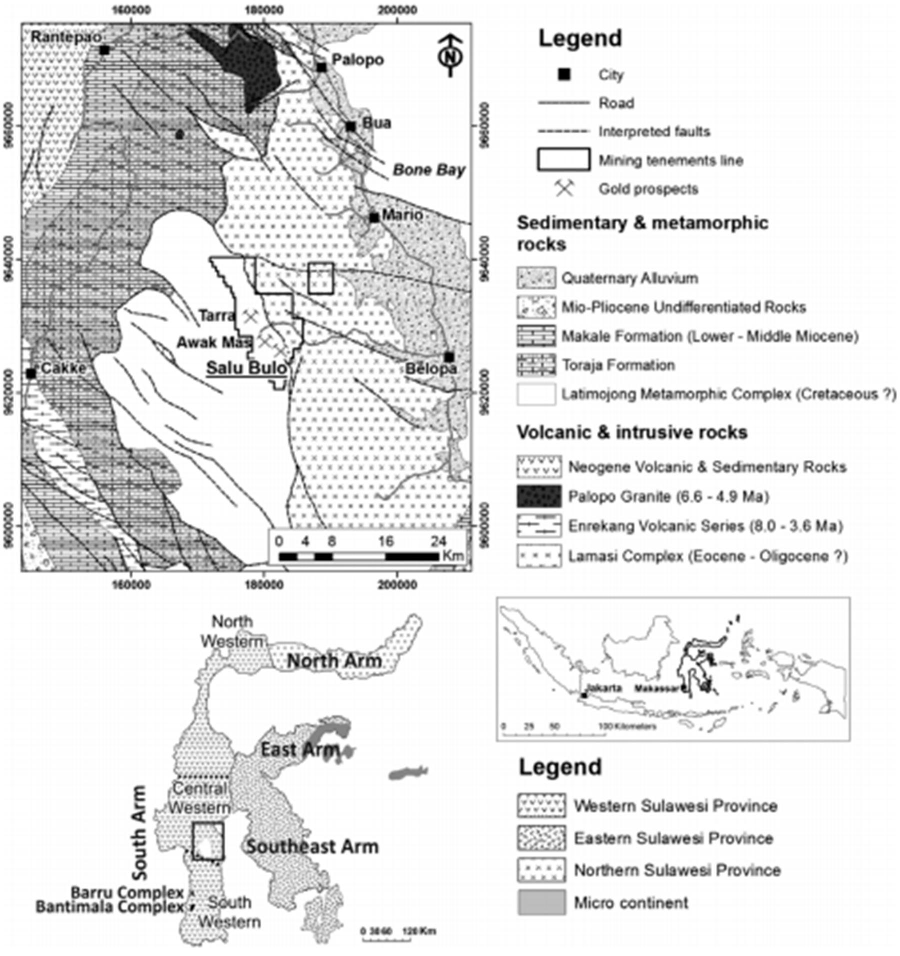

Figure 8. Regional geological map of the study area (modified from White et al., 2017).

Initial metamorphism of Latimojong Metamorphic Complex occurred in magmatic arc in an active margin in Middle Cretaceous, followed by progressive high-pressure condition at collisional zone (Susilo, 1998). Latimojong Metamorphic Complex underwent low to medium grade metamorphism, i.e., zeolite, actinolite-pumpellyite, greenschist with glaucophane and greenschist-amphibolite facies (Susilo, 1998) (Fig. 9). Zeolite facies was formed at temperature < 225 °C and pressure at 3 kbar while actinolite-pumpellyite facies was formed at temperature ± 310-350 °C and pressure at 3-4.5 kbar, in depth > 9 km. Greenschist facies with glaucophane was formed at temperature > 350 °C and pressure at > 8 kbar, in depth > 24 km while greenschist-amphibolite facies was formed at temperature 550 °C and pressure at > 6 kbar.

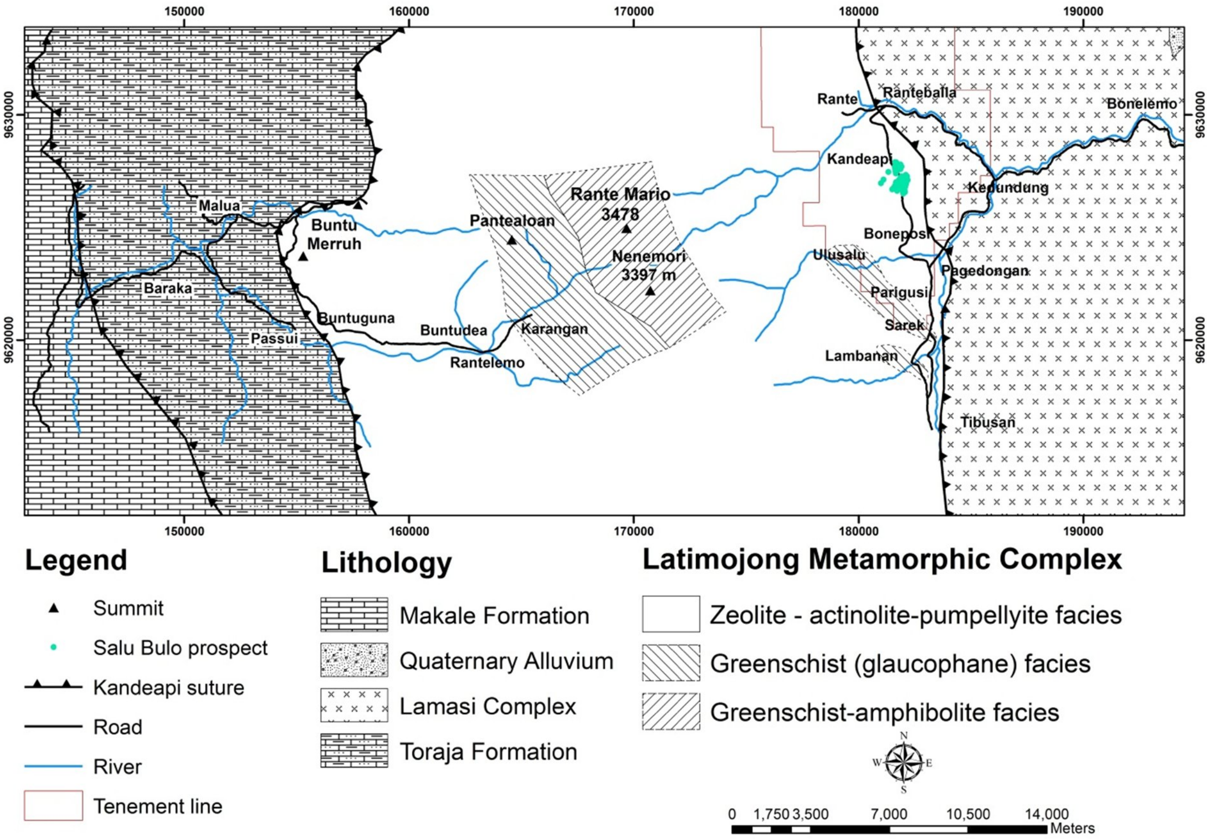

Figure 9. Metamorphic facies map of Latimojong Metamorphic Complex (after Susilo, 1998; Djuri et al., 1998; White et al., 2017).

The Latimojong Metamorphic Complex is unconformably overlain by the clastic rocks of the Eocene-Oligocene Toraja Formation and Lower-Middle Miocene Makale

Formation in the western part, while the Eocene-Oligocene (?) Lamasi Complex overlies the eastern part (Bergman et al., 1996; Djuri et al., 1998; Susilo, 1998; White et al., 2017) (Fig. 8). Lamasi Complex consists of intrusive rocks (i.e., sheared diorite plutons, amphibolite gneisses (metagabbros) and sheeted basalt dyke) and extrusive rocks (i.e., basaltic pillow lavas, basalt to andesite lava flows and agglomerates, and andesite, dacite and rhyolitic pyroclastic deposits that comprising of block breccias, tuff breccias and tuffs), which were intensely deformed, metamorphosed and bounded by thrust faults (Bergman et al., 1996) (Figs. 8, 9, 10a). The basaltic rocks were interpreted to represent obducted MORB or back-arc oceanic crust (Bergman et al., 1996). Eocene-Oligocene obduction of back arc rocks (Lamasi Complex) was interpreted to have been related to subsequently deformation and uplift of Latimojong Metamorphic Complex above sea level (White et al., 2017).

Toraja Formation is situated in the west of the Latimojong Metamorphic Complex (Figs. 8, 9). It consists of quartz sandstone, limestone, reddish purple shale, conglomerate, and locally coal (Coffield et al., 1993; Djuri et al. 1998; Susilo, 1998) (Fig. 10b). The large foraminifera fossils in limestone indicate Eocene-Miocene (Djuri et al., 1998) or Eocene-Oligocene age (Calvert & Hall, 2007). The Toraja Formation has been interpreted as a terrestrial deltaic sequence in the Latimojong and Makale region associated with rifting and was interspersed with periods of arc and back arc volcanism (e.g. Lamasi Complex) (White et al., 2017), deposited unconformably above Mesozoic basement rocks (Calvert & Hall, 2007). Toraja Formation is unconformably overlain by Makale Formation, a platform limestone platform, formed in more restricted a shallow marine environment during Late Eocene or Early Miocene to Middle Miocene (Coffield et al., 1993; Djuri et al., 1998) (Figs. 8, 9). Collision of the Sula Spur with Sulawesi's North Arm in the Early Miocene caused uplift and the development of another unconformity later related to the period of relative quiescence and growth of pinnacle and patch reefs (White et al., 2017). In Latimojong and Makale regions, it is found as cap in many summits showing steep cliffs and karst topography (White et al., 2017).

Figure 10. Photograph of various lithology in Latimojong Metamorphic Complex consisting of phyllite (a), meta-chloritic mudstone (b), quartz-muscovite schist (c), muscovite-garnet schist in Lambanan (d) boulder of actinolite-epidote schist (?) in Karangan (e), and meta-andesite (?) (f).

2.3.2 Magmatism in the central part of western Sulawesi

Magmatism in the central part of western Sulawesi occurred during the Eocene to Pleistocene and formed the calc-alkaline or island-arc tholeiitic, potassic calc-alkaline and shoshonitic rocks. The magmatism was caused by crustal thickening in a collision event and/or partial melting in active subduction environment (Priadi et al., 1994; Bergman et al., 1996; Elburg & Foden 1999; Maulana et al., 2016; White et al., 2017). The northern part of

Latimojong Metamorphic Complex was intruded by the Mio-Pliocene Palopo Granite (Figs. 11c, d). The Palopo Granite is characterized by potassium-rich calc-alkaline composition (Priadi et al., 1994; White et al., 2017). The intrusion was formed by continental crustal melting during plate collision (Priadi et al., 1994; Bergman et al., 1996) or by arc magmatism (White et al., 2017).

Kusnadi and Setiawan (2009) reported a Bittuang geothermal system which is related to Early Quaternary Karua volcano, located in Toraja District, South Sulawesi. The Karua volcano consists of andesitic lava and ended with dacitic igneous rocks. During Pleistocene, the volcanism formed an oxbow caldera structure open to northern area and lava dome in the middle of Karua volcano caldera. Two active geothermal manifestations are solfatara and hot spring, exist in Balla and Cepeng, respectively. The temperature of hot spring in Balla ranges from 48.1 to 96.7 ^{o}C with pH ranges from 5.4 to 8.4, whereas temperature of hot spring in Cepeng ranges from 37.6 to ^{o}C with pH ranges from 5.97 to 6.28. The result of the geochemical gas composition taken from solfatara shows that CO_2 ranges from 96.7 to 97.9 mol%, N_2 ranges from 1.79 to 2.68 mol%, O_2 + Ar ranges from 0.19 to 0.60 mol% and H_2 ranges from 0.019 to 0.02 mol %.

2.4 Geological framework of the Awak Mas project

The Latimojong Metamorphic Complex is locally divided into the basement and the cover sequences (Archibald et al., 1996; Smillie, 1996). The cover sequence consists of deep marine turbidites, volcanic and volcaniclastic rocks, which were metamorphosed to greenschist facies (Smillie, 1996). The basement sequence, on the other hand, is composed of Lower Cretaceous high-pressure blueschist, highly altered diorite and minor ultramafic rocks, which have been tectonically interleaved with the cover sequence (Archibald et al., 1996; Smillie, 1996). The Salu Bulo prospect is hosted by the cover sequence of Latimojong Metamorphic Complex. Within the prospect, the Latimojong Metamorphic Complex consists of meta-dark (graphitic), green (chloritic) and red (hematitic) mudstone, siltstone, sandstone and intercalated meta-volcanic and volcaniclastic rocks along with phyllite (Fig. 12a). The host rock foliation strike toward northwest dipping northeast. Higher grade metamorphic rocks are exposing in Ulusalu and Lambangan namely quartz-muscovite schist and locally muscovite-garnet schist, respectively that occurred as block in the cover sequence of Latimojong Metamorphic Complex (Figs. 10d, 12b).

Figure 11. Photograph of gabbro of Lamasi Complex (a), purple-red shale of Toraja Formation (b), and Palopo Granite in the road from Toraja to Palopo (c-d).

Diorite was observed during field works in the Awak Mas project and the surrounding area which shows parallel contact with meta-sedimentary rocks and not showing intrusive contact (Fig. 12c). This observation suggesting that diorite was formed before metamorphism of the host rocks and become part of Latimojong Metamorphic Complex (Archibald et al., 1996; White et al., 2017; this study). Diorite consists of quartz, plagioclase, calcite, chlorite, prehnite or pumpellyite and pyrite and cut by calcite veins. Limestone bodies containing large Foraminifera fossils were also observed as a giant boulder surrounding the Awak Mas project suggesting an uncertainty of age of Latimojong Metamorphic Complex

(Fig. 12d). Large foraminifera fossil was reported in a member of Toraja Formation indicating Eocene age (Djuri et al., 1998).

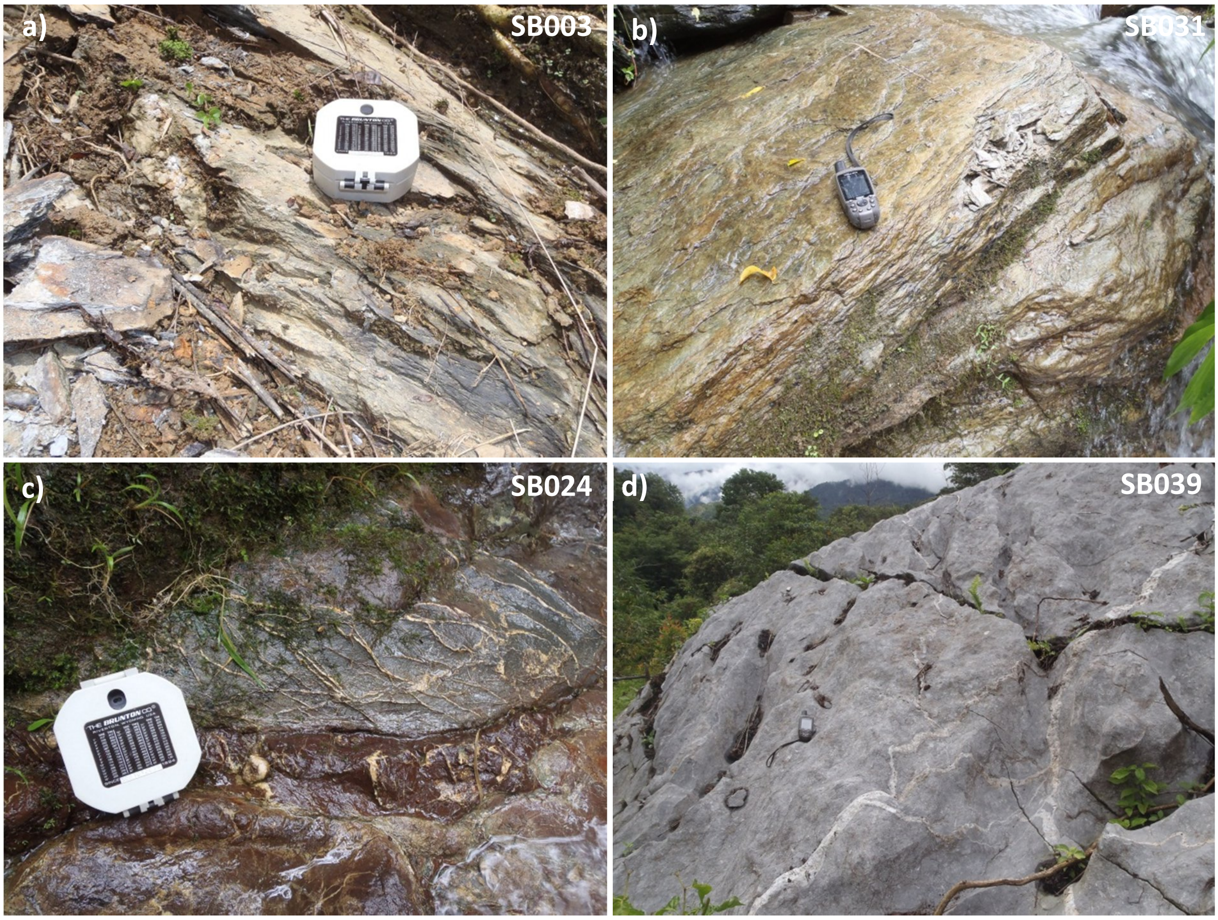

Figure 12. Photograph of various lithology of Latimojong Metamorphic Complex in surrounding the Awak Mas project. a) meta-graphitic mudstone; b) quartz-muscovite schist in Ulusalu; c) diorite showing contact to meta-(hematitic) mudstone; and d) boulder of limestone surrounding camp site.

Three main deformation events were recognized in the Latimojong Metamorphic Complex and particularly in the Awak Mas district which were classified into D1, D2 and D3 (Archibal et al., 1996; Smillie, 1996; Susilo, 1998). D1 (initial deformation) is early flattening fabrics (S1) in fine-grained cover sequence that is parallel to bedding (S0). D2 (ductile deformation) is major deformation event of thrusting and folding recognized by ductile deformation under microscope that was formed during obduction in Eocene-Oligocene (?). D3 (brittle deformation) is a major episode of late extension formed normal faulting and brecciation that was recognized as the occurrences of chlorite and calcite veins

(Susilo, 1998). Gold mineralization in the Awak Mas project appears to have occurred during this event.

CHAPTER III: ANALYTICAL METHODS

Samples were collected during field works in the Salu Bulo prospect and the surrounding area. 16 drill holes were selected to collect 179 drill core samples along with 39 outcrop samples representing host rocks and ores (i.e., veins and stockwork and breccia) (Fig. 14, Appendices 1-3). These samples were identified and analyzed by a combination of hand specimen observation, reflected and transmitted microscopy, powder X-ray diffraction, Scanning Electron Microscopy-Energy Dispersive X-ray Spectroscopy, Electron Microprobe Analyses, Inductively Coupled Plasma Mass Spectrometry, and fluid inclusion microthermometry and laser Raman microspectroscopy.

3.1 **Field**

Activities within the fieldwork consist of geological observation, sample collection and data measurements in field (outcrop) and drill cores. Outcrop observation aims to understand mineralization and lithological orientation and correlation to guide when conduct subsurface interpretation. Drill holes observation aims mainly to collect subsurface sample and understand the vertical characteristics of mineralization in detail. To obtain data and samples some geological equipment were used such as geological hammer, compass, magnetic susceptibility meter, loupe, camera and etc. The samples obtained from surface and drill holes observation consist of veins, breccia, host rocks (meta-sedimentary, -volcanic and –volcaniclastic rocks), intrusive rocks (diorite and gabbro) and sedimentary rocks. The samples were shipped to Akita University for laboratory analyses.

3.2 Laboratory Analyses

3.2.1 Optical microscopy

Thin and polished sections of host rocks and ores were prepared and observed under the microscope using a Nikon polarization optical microscope for petrography and fluid inclusions description.

3.2.2 X-ray Diffrcatiometer (XRD)

X-ray diffractiometer analysis for samples from ores and host rocks was conducted using a RIGAKU MultiFlex X-ray diffractometer in Akita University, Japan (Appendix 4). Scan ranged from 2° to 60° (2θ) for bulk and 2° to 40° (2θ) for clay analyses in steps of 0.01° at 2°/min scan speed, using a monochromated Cu Kα (λ= 1.54178 Å) radiation. The operating conditions were maintained at 30kV operating voltage and 16mA current.

3.2.3 Scanning Electron Microscope – Energy Dispersive X-ray Spectroscopy (SEM-EDX)

Detailed mineral identification was done by a JOEL JSM 6610 LV Scanning Electron Microscopy-Energy Dispersive Spectroscopy at Akita University. In advance, samples were carbon coated with a JEOL-560 Auto Carbon Coater. The measurement conditions were 15 kv of accelerating voltage = 15 kV, 60 μA of filament load current (L.C.) and spot size 10 mm of Z-axis distance with good beam stability.

3.2.4 Electron Microprobe Analyses (EPMA)

Chemical compositions of native gold, electrum and pyrite were analyzed using a JEOL JXA-8800R microprobe in Akita University, Japan with operating conditions with a voltage at 20 kV and a probe current at 20 nA. For native gold and electrum analysis, the elements were calibrated using native gold (Au), native silver (Ag) and native copper (Cu) as standard specimens and acquired using analyzing crystals: LiF for Cu Ka and PETJ for Au Ma and Ag La with counting time was 10 s on peak and 5 s on background position (Table 3). For pyrite, elements were calibrated using Ga As (S), FeS_2 (Fe, S), native nickel (Ni), native Cu (Cu), Native Co (Co), ZnS (Zn), native tungsten (W) and native gold (Au) as standard specimens and acquired using analyzing crystals: LiF for Fe Ka, Ni Ka, Cu Ka, Co Ka, W La, Zn Ka and Au La, TAP for As La and PETJ for S Ka (Table 3). All of the standards (natural and synthetic) were tested for homogeneity before their utilization for quantitative analysis.

Table 3. Standard materials for electron microprobe analyses of pyrite, native gold and electrum.

Observation minerals	Standard materials	Elements	X-ray	Diffracting Crystals	Peak counting time	Background counting time	Detection limit (PPM)
Pyrite	GaAs	As	La	TAP	50s	25s	143
	FeS2	Fe	Ka	LiF	10s	5s	0.02*
		S	Ka	PETJ	10s	5s	0.05*
	Native nickel	Ni	Ka	LiF	50s	25s	80
	Native Cu	Cu	Ka	LiF	10s	5s	242
	Native Co	Co	Ka	LiF	50s	25s	79
	Native tungsten	W	La	LiF	50s	25s	237
	ZnS	Zn	Ka	LiF	10s	5s	296
	Native gold	Au	La	LiF	200s	100s	194
Native gold, electrum	Native Cu	Cu	Ka	LiF	10s	5s	519
	Native silver	Ag	La	PETJ	10s	5s	435
	Native gold	Au	Ma	PETJ	10s	5s	0.2*

*) wt%

3.2.5 Inductively Coupled Plasma Mass Spectrometry (ICP-MS)

Bulk chemical compositions of 23 samples of unaltered host rocks, hydrothermally altered rocks and ores were analyzed using Inductively Coupled Plasma-Mass Spectrometry at Acme Laboratory in Vancouver, Canada. A proper amount of each rock sample was crushed and pulverized in agate mortar to clay size grain. Approximately 5 milligrams sample were sent to the laboratory. Of these, 23 samples were analyzed for major, trace and rare earth elements.

3.2.6 Microthermometry

Fluid inclusion studies were conducted on mineralizing vein and matrix of breccia. Doubly polished sections were prepared for fluid inclusion petrography, microthermometry and laser Raman microspectrometry analyses. Petrographic analysis was done using a Nikon polarization optical microscope for descriptive classifications of fluid inclusions to record distribution, size, types and textural relationships. Microthermometry was conducted using a LINKAM THM 600 heating-freezing stage equipped with a Nikon optic microscope to determine the homogenization and the melting temperatures. The heating rate to observe the phase change was 0.1–5 °C/min. Salinities were calculated from the final ice melting temperatures (Bodnar, 1993) and expressed as wt% NaCl equivalent.

3.2.7 Laser Raman microspectrometry

Volatile compositions of fluid inclusions (carbonic phase) and single mineral inclusion were determined using Renishaw Invia Raman Microspectrometer in Akita University, Japan with a 514 nm Argon laser for excitation. The calibration was made using the 520.7 cm^{-1} Raman line of silicon. Most of the spectra were obtained using a 100× objective lens with a counting time of 15 seconds with a 1μm laser beam in 1-5 accumulation for each spectral line. The results were obtained as a wide spectral range between 38 to 4600 cm^{-1} and narrow spectral range between 940 to 2500 cm^{-1} to identify CO_2, N_2 and graphite. Density of CO_2 was calculated using delta (Δ) value of Fermi doublet peaks of CO_2 by an equation from Yamamoto and Kagi (2006):

$$\text{Density} = -0.01917*(\Delta - 100)^3 + 0.1984*(\Delta - 100)^2 - 0.2410*(\Delta - 100) - 0.341.$$

3.2.8 Oxygen isotopes

Oxygen isotopic compositions of two quartz samples from quartz vein of the main stage vein (iii) were analyzed at the GNS Science Lab, Lower Hutt, New Zealand. Oxygen was extracted from sample powders for isotope analyses using a CO_2-laser and BrF_5. The results are presented in $\delta^{18}O$ (‰) relative to the standard mean ocean water (SMOW). The $\delta^{18}O$ values of quartz sample were corrected using NBS-28 with precision ±0.15 ‰.

3.2.9 Sulfur isotopes

Sulfur isotopic ratios of 23 pyrite samples were analyzed. Pyrites were prepared from host rocks and ores and weighted in approximately 10-20 milligrams of each sample. Pyrite was decomposed by nitric acid (HNO_3) and bromine (Br_2) and finally converted to barium sulfate ($BaSO_4$) which SO_2 gas was obtained for sulfur isotope measurement (Yanagisawa & Sakai, 1983). Approximately 0.5 milligrams of $BaSO_4$ was mixed and folded with 2-2.5 milligrams of V_2O_5 in a tin tube. The samples were measured using a Thermo Fisher Scientific Delta-V Advantage isotopic ratio mass spectrometer at Akita University, Japan with standard samples i.e., IAEA-SO-5, IAEA-SO-6 and NBS-127. The results are presented in $\delta^{34}S$ (‰) relative to Canyon Diablo Troilite (CDT). Analytical uncertainty is ±0.2.

CHAPTER IV: GEOLOGY OF THE STUDY AREA

4.1 Stratigraphy

Geological mapping, drill core observation, petrography and XRD analyses have been conducted to identify lithology in the Salu Bulo prospect. The Salu Bulo prospect consists of meta-sedimentary rocks and intercalated meta-volcanic and -volcaniclastic rocks. Gold mineralization was hosted by meta-dark (graphitic), green (chloritic) and red (hematitic) mudstone, siltstone, sandstone and intercalated meta-volcanic and volcaniclastic rocks along with phyllite (Fig. 13). The host rock foliation mainly strikes toward northwest dipping northeast (Fig. 13).

4.1.1 Meta-sedimentary rocks

Meta-(hematitic) mudstone

Meta-hematitic mudstone is easily recognized by red to dark red color in outcrop and drill cores which contains hematite (Fig. 14). It is composed of hematite, quartz, calcite and illite or muscovite along with pyrite showing various metamorphic grades (Fig. 14b). The mineralizing veins are hosted by this rock with or without alteration halo (Fig 14b). It is intercalated to meta-volcaniclastic rocks and meta-volcanic rocks with sharp contact in the outcrop and drill core (Fig. 14a). Meta-(hematitic) mudstone shows various metamorphic grades reflected by the presence of illite or muscovite in the higher metamorphic grade rocks. Hematite was formed during deposition of the rocks prior to metamorphism. Veins in meta-(hematitic) mudstone formed parallel and cross cut to the foliation. The rocks are often brecciated with various alterations intensity.

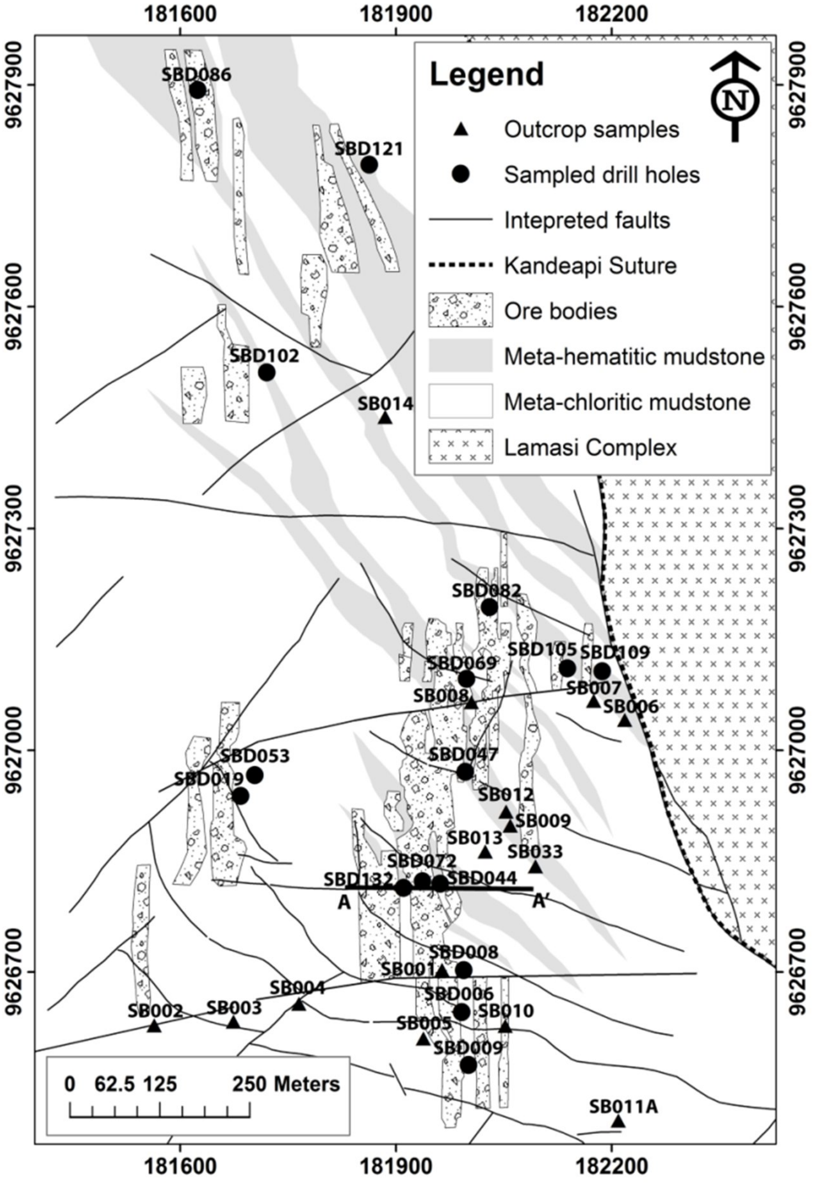

Figure 13. Geological map of the Salu Bulo prospect that shows north-south trending mineralized zones (modified from PT Masmindo Dwi Area). Location of the section line A-A' of Figure 22a is indicated.

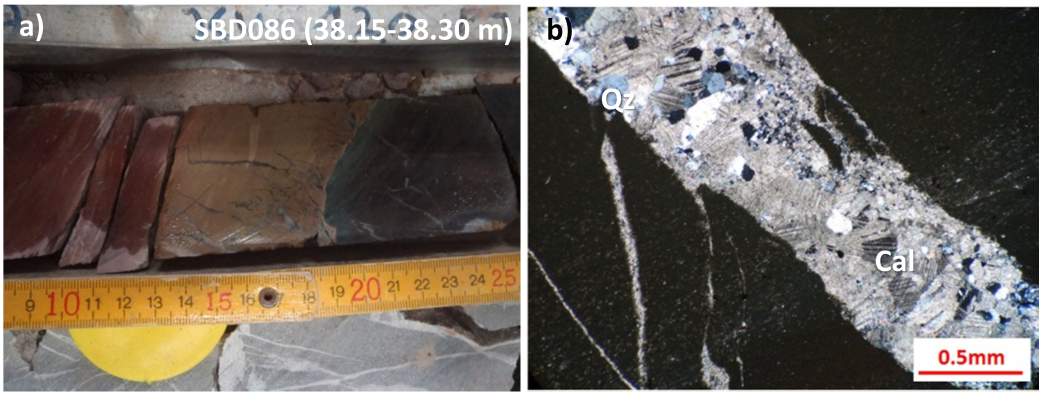

Figure 14. a) Photograph of meta-(hematitic) mudstone with sharp contact to meta-volcanic rock of drill core at SBD086; and b) photomicrograph of meta-(hematitic) mudstone that hosts a carbonate-quartz vein. Abbreviation: Qz (quartz); Cal (calcite).

Meta-(graphitic) mudstone

Meta-graphitic mudstone is characterized as dark (black) colored fine-grained rocks (Fig. 15a). Under the microscope, it consists of graphite, quartz, plagioclase, illite or muscovite and pyrite (Figs. 15b). It is intercalated with other meta-sedimentary rocks, meta-volcaniclastic rocks and meta-volcanic rocks in the section. Early quartz-calcite veins are mainly parallel to the foliation. The opaque mineral is mainly pyrite that shows framboidal texture in fine-grained size. The mineralizing veins were hosted by these rocks with or without alteration halo.

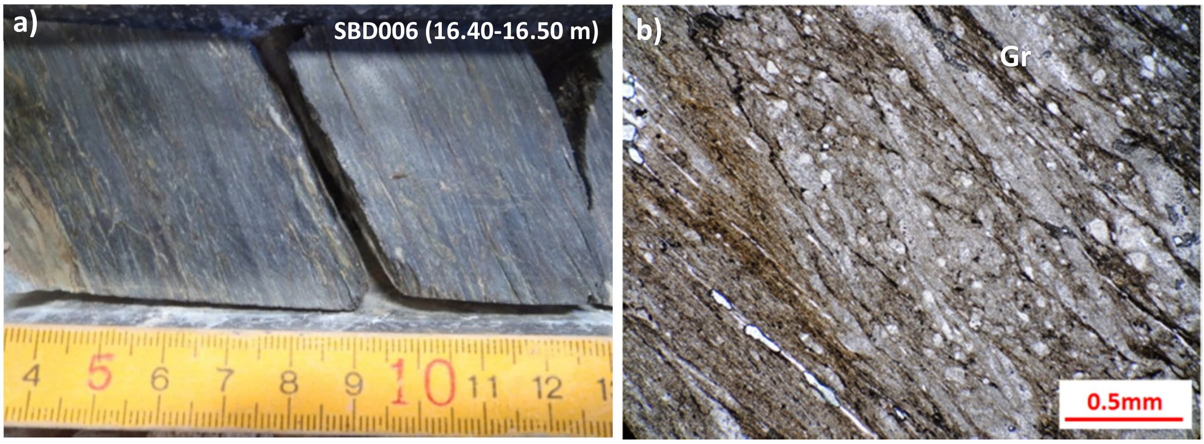

Figure 15. a) Photograph of meta-graphitic mudstone of drill core at SBD006; and b) photomicrograph of meta-graphitic mudstone showing graphite parallel to the foliation. Abbreviation: Gr (graphite).

Meta-(chloritic) mudstone

Meta-(chloritic) mudstone is likely a host rock to gold mineralization in the Salu Bulo prospect. It is easily recognized as a green color fine-grained rock in the outcrops and drill cores (Fig. 16a). It is composed of chlorite, quartz, calcite, illite or muscovite, pyrite and lesser prehnite or pumpellyite and epidote? along with pyrite (Fig. 16b). Pyrite commonly shows framboidal texture and is fine-grained in size. The early quartz-calcite vein is parallel to the foliation. The rocks are often brecciated and host various composition of veins that were related to gold mineralization.

Meta-siltstone – meta-sandstone

Meta-siltstone and meta-sandstone (greywacke?) are divided based on their grain size (Fig. 16c-f). Meta-siltstone is composed of quartz, calcite, graphite, hematite? and pyrite (Fig. 16d). Meta-sandstone is composed of mainly quartz along with plagioclase, calcite, chlorite, illite or muscovite, lithic fragment and pyrite (Fig. 16f). It often shows anastomosing cleavage indicating underwent metamorphism. Some observations show locally carbonate minerals are abundant. Gold mineralization is hosted by in meta-sandstone with wider alteration halo along the mineralizing veins.

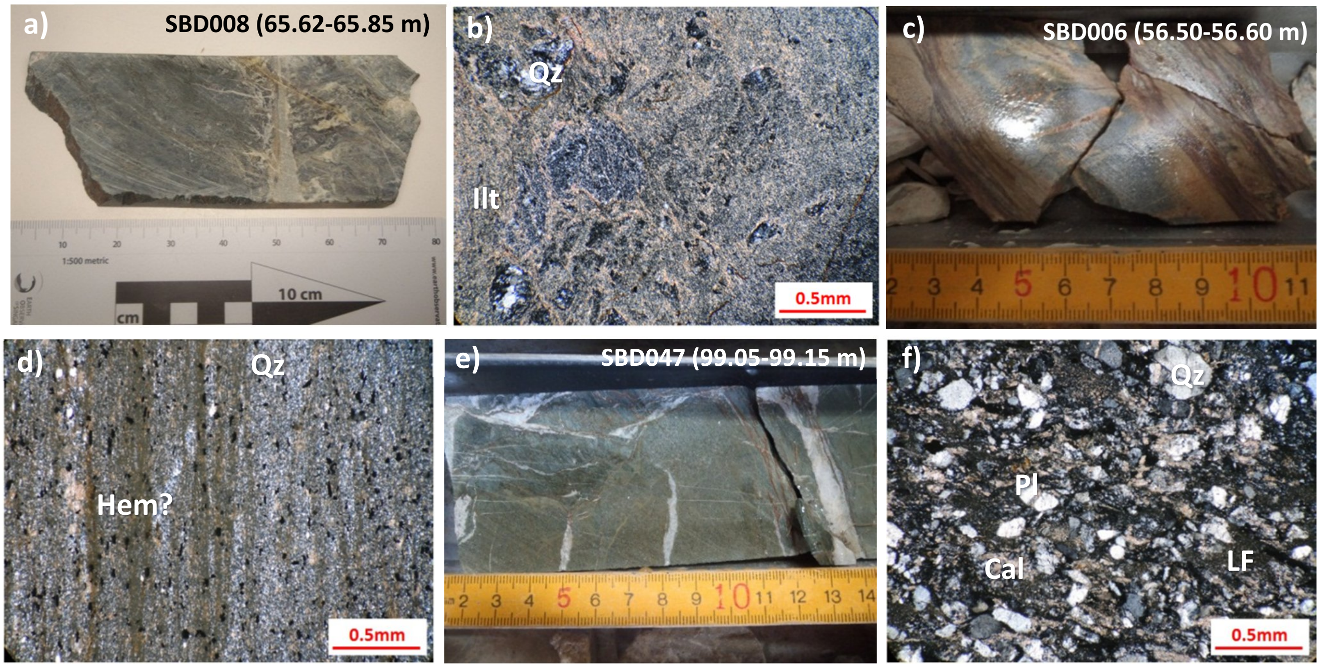

Figure 16. a) Photograph of meta-(chloritic) mudstone of drill core at SBD008; b) photomicrograph of meta-(chloritic) mudstone that consists of quartz, illite and chlorite; c) photograph of meta-siltstone of drill core at SBD006; d) photomicrograph of meta-siltstone that consists of mainly quartz, hematite? along with pyrite; e) photograph of meta-sandstone of drill core at SBD047; and f) photomicrograph of meta-sandstone that consist of quartz, plagioclase, calcite and lithic fragment. Abbreviation: Qz (quartz); Cb (carbonate mineral); Ilt (illite); Hem (hematite); Chl (chlorite); LF (lithic fragment).

4.1.2 Phyllite

A higher metamorphic grade of meta-sedimentary rock in the Salu Bulo prospect is phyllite. It shows silky lustered, is highly foliated and folded occurs as minor host rocks in the Salu Bulo prospect (Figs. 17a, b). Quartz is relatively coarser than in the meta-mudstone. Graphite and hematite are aligned commonly parallel to the foliation. It more contains illite or muscovite reflecting higher metamorphic grade compared to other meta-sedimentary rocks. The early quartz-carbonate vein is parallel to foliation and boudined. Quartz-ankerite±albite and ankerite-quartz±albite veins are occasionally observed parallel to the foliation and folded that formed after formation of framboidal pyrite showing pressure shadow or quartz fringe. Phyllites mainly consist of quartz with augen texture, illite or muscovite, calcite, ankerite, plagioclase, graphite, lesser hematite and pyrite (Figs. 17c, d). Pyrite occurred probably as a product of diagenesis or metamorphism as it was aligned parallel to the foliation and it is fine-grained, aggregated and boudined.

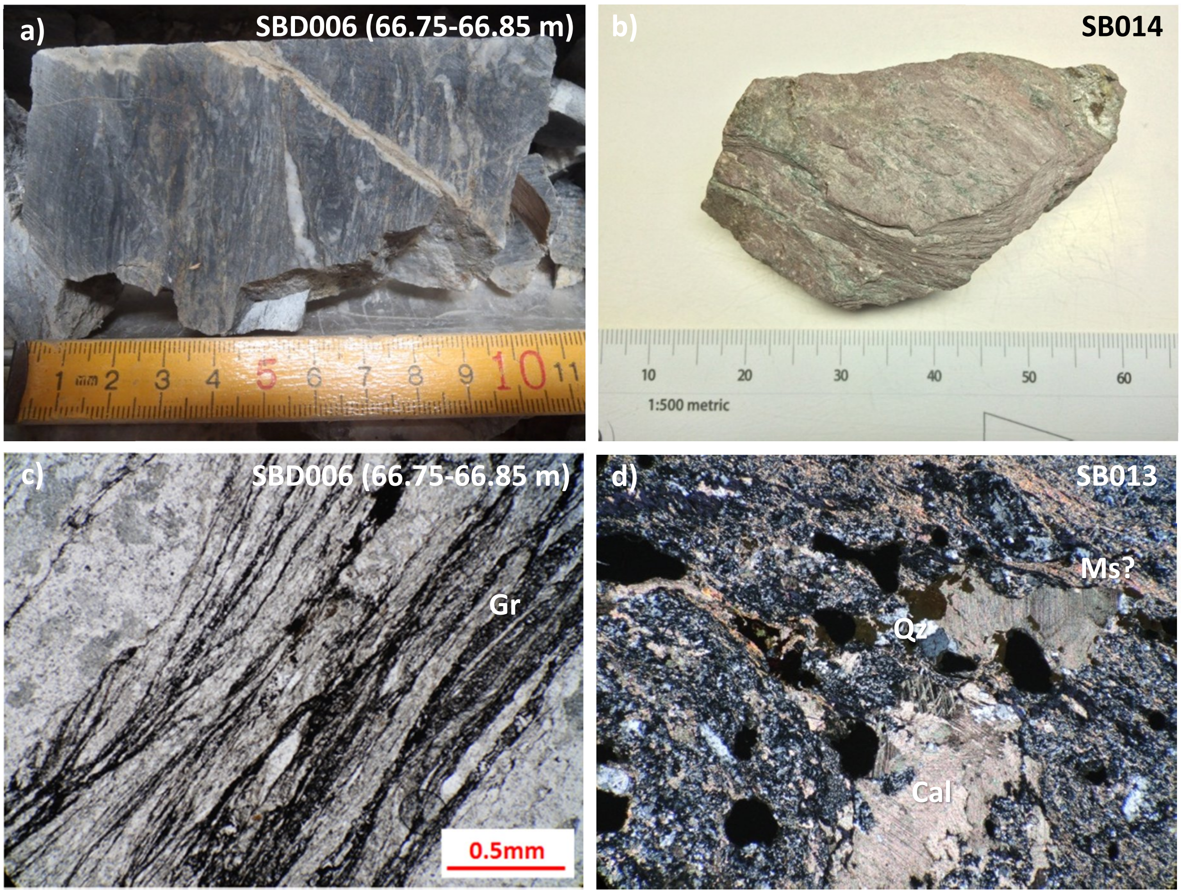

Figure 17. a) Photograph of phyllite of drill core at SBD006; b) photograph of phyllite (meta-hematitic mudstone) at SB014; c) photomicrograph of highly foliated phyllite reflecting by more graphite in the foliation plane; and d) photomicrograph of phyllite at SB013 that consist of mainly quartz, carbonate mineral and sericite. Abbreviation: Qz (quartz); Cal (calcite); Ms (muscovite); Gr (graphite).

4.1.3 Meta-volcanic and meta–volcaniclastic rocks

Meta-volcanic and meta-volcaniclastic rocks are intercalated with meta-sedimentary rocks observed in the outcrop and drill cores (Figs. 14a, 18b). Meta-volcanic rocks consist of plagioclase, pyroxene altered to chlorite, calcite, muscovite, prehnite or pumpellyite?, epidote, hematite and pyrite (Fig. 18a). It's original rock is classified as basalt based on its mineral compositions. Calcite and chlorite are metamorphic mineral assemblages that converted from plagioclase and originally mafic minerals. Meta-volcaniclastic rocks are composed of fine ash, illite or muscovite, chlorite, pyroxene, calcite, quartz, plagioclase, lithic fragment, prehnite or pumpellyite, epidote? and pyrite (Fig. 19c). Chlorite, illite or muscovite and carbonate minerals are the main metamorphic mineral assemblages in this rock. It is classified as lithic tuff (?) based on its mineral composition and texture. These rocks host carbonate-quartz-albite veins and show same alteration mineral assemblages in the alteration halo.

Figure 18. a) Photomicrograph of meta-volcanic rock that consists of plagioclase and carbonate mineral of drill core at SBD086; b) photograph of meta-volcaniclastic rock at SB014; and c) photomicrograph of meta-volcaniclastic rock that consists of lithic fragment and carbonate mineral. Abbreviation: Pl (plagioclase); Cal (calcite); Ank (ankerite); LF (lithic fragment).

4.2 Metamorphic grade

Under the microscope analysis, metamorphic mineral assemblages can be recognized namely illite or muscovite parallel to the foliation, calcite and ankerite which replaced original plagioclase in meta-volcanic rocks and meta-volcaniclastic rocks. Graphite that occurred parallel to the foliation in highly foliated rocks (e.g. phyllite) was formed during metamorphism. Chlorite replaced original mafic minerals such as pyroxene in meta-volcanic rocks and meta-volcaniclastic rocks, meta-sandstone and meta-mudstone. Quartz was formed during metamorphism. Along those minerals, prehnite or pummpellyite were also observed rarely in the meta-(chloritic) mudstone, meta-volcanic rocks and meta-volcaniclastic rocks. Albite is present in the meta-sandstone, meta-(graphitic) mudstone and phyllite. Epidote is present in meta-volcanic rock, meta-volcaniclastic rocks and meta-(chloritic) mudstone.

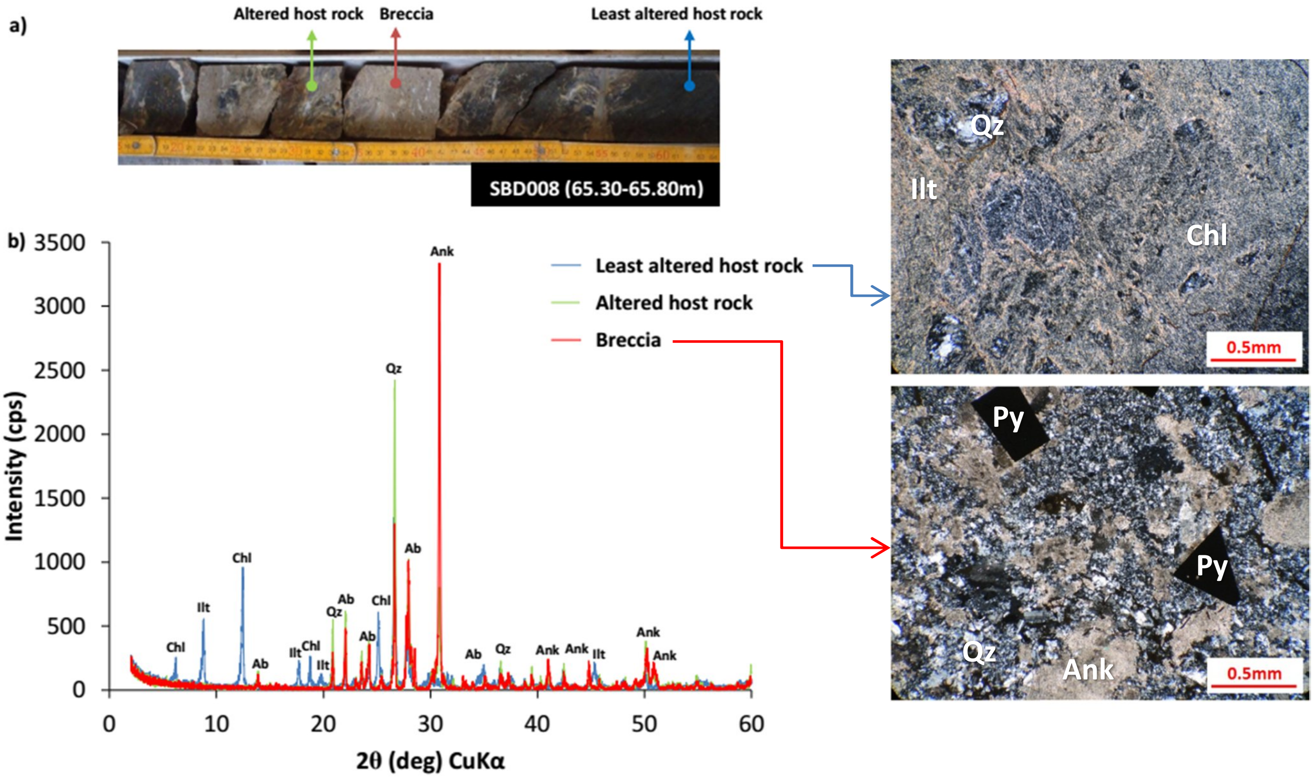

Abbreviations: Ab = albite; Ank = ankerite; Chl = chlorite; Ilt = illite; Qz = quartz

Figure 19. a) Photograph of mineralized part of meta-(chloritic) mudstone intersected by a drill core of SBD008 at 65.30-65.80 m depth; and b) X-ray diffraction peaks of least altered and altered host rock and breccia of Figure 19a. Abbreviation: Qz (quartz); Ilt (illite); Py (pyrite); Ank (ankerite); Chl (chlorite).

Veins formed during metamorphism were quartz-calcite and rarely quartz-ankerite±albite veins that are parallel to the foliation. Quartz shows undulose extinction indicating recrystallization process while calcite shows twinning. Quartz-ankerite±albite veins are particularly hosted in the highly foliated host rocks (i.e phyllite). XRD analyses of several samples of unaltered host rocks show illite and chlorite peaks and absent in ores indicating those were formed during metamorphism (Fig. 19, Appendix 4).

Based on those mineral assemblages in the metamorphic host rocks and veins, the protoliths of the host rocks in the Salu Bulo prospect have been low-grade prehnite-pumpellyite facies metamorphism with temperature and pressure ranging from 150 to 250 °C and 2 to 6 kbar, respectively (Fig. 20). Illite peaks from XRD analysis were also used to know the temperature formation of those minerals. Using Kubler Index method, illite crystallinity values from illite peaks in ethylene-glycol treatment were obtained. These values were used to calculate temperature formation using formula from Hara and Kurihara (2010). The temperature formation of illite was 150 to 250 °C that fits in the low-grade prehnite-pumpellyite facies.

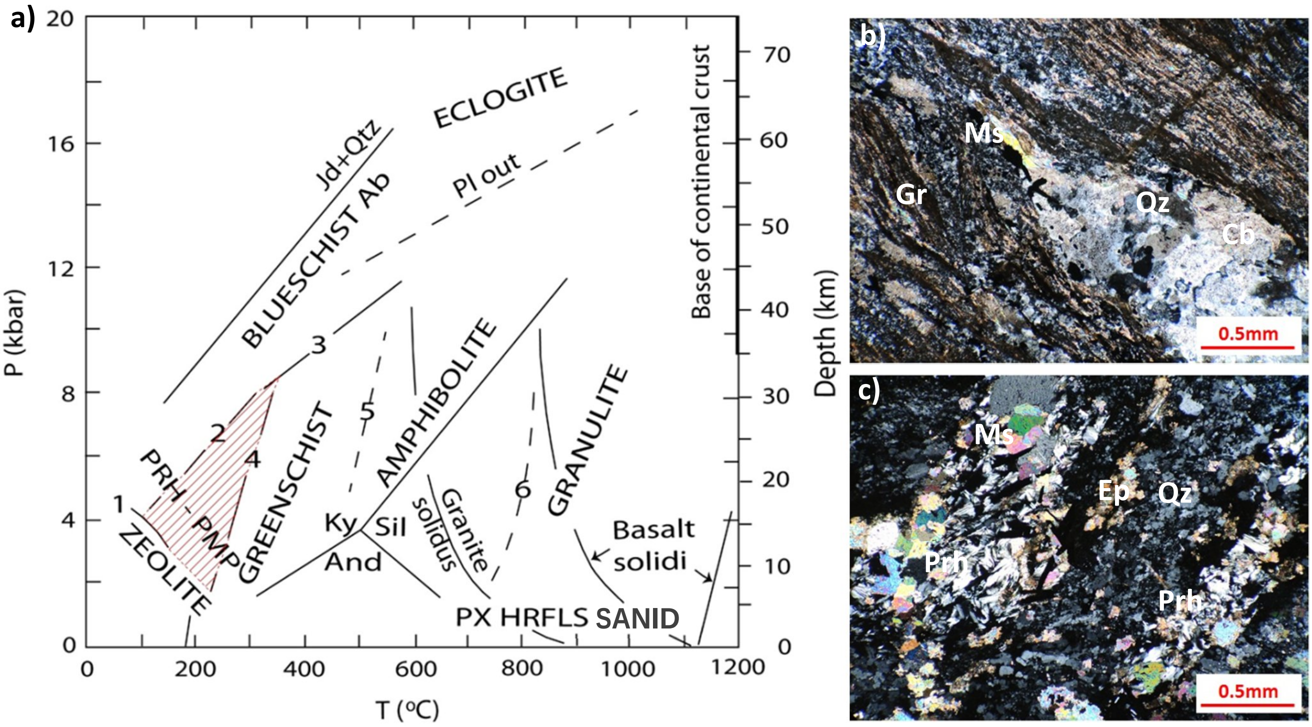

Figure 20. a) Metamorphic facies condition of host rocks in the Salu Bulo prospect (Modified from Best, 2003); photomicrograph of phyllite (b) and meta-(chloritic) mudstone (c) showing representative metamorphic mineral assemblages. Abbreviation: Qz (quartz); Ilt (illite); Cb (carbonate mineral); Prh (prehnite); Ms (muscovite); Ep (epidote); Gr (graphite); Jd (jadeite); Ky (kyanite); Sil (sillimanite); Ab (albite); Px (pyroxene); Hrfls (hornfels); And (andalusite); Pl (plagioclase); Prh-Pmp (prehnite-pumpelliyite).

4.3 Structural geology

The Salu Bulo prospect is located nearest the Kandeapi Suture which is the boundary between the Latimojong Metamorphic Complex and the adjacent Lamasi Complex, 1.8 km to the southeast of Awak Mas prospect (Figs. 9, 13, 21a). Structural control of gold mineralization in the Salu Bulo prospect remains unclear. Preliminary structural mapping has been done by the company (Querubin, 2011 unpublished report). The parallel to sub-parallel northeast-southwest and northwest-southeast trending faults show that they were not related to gold mineralization which displaced the ore bodies (Fig. 13).

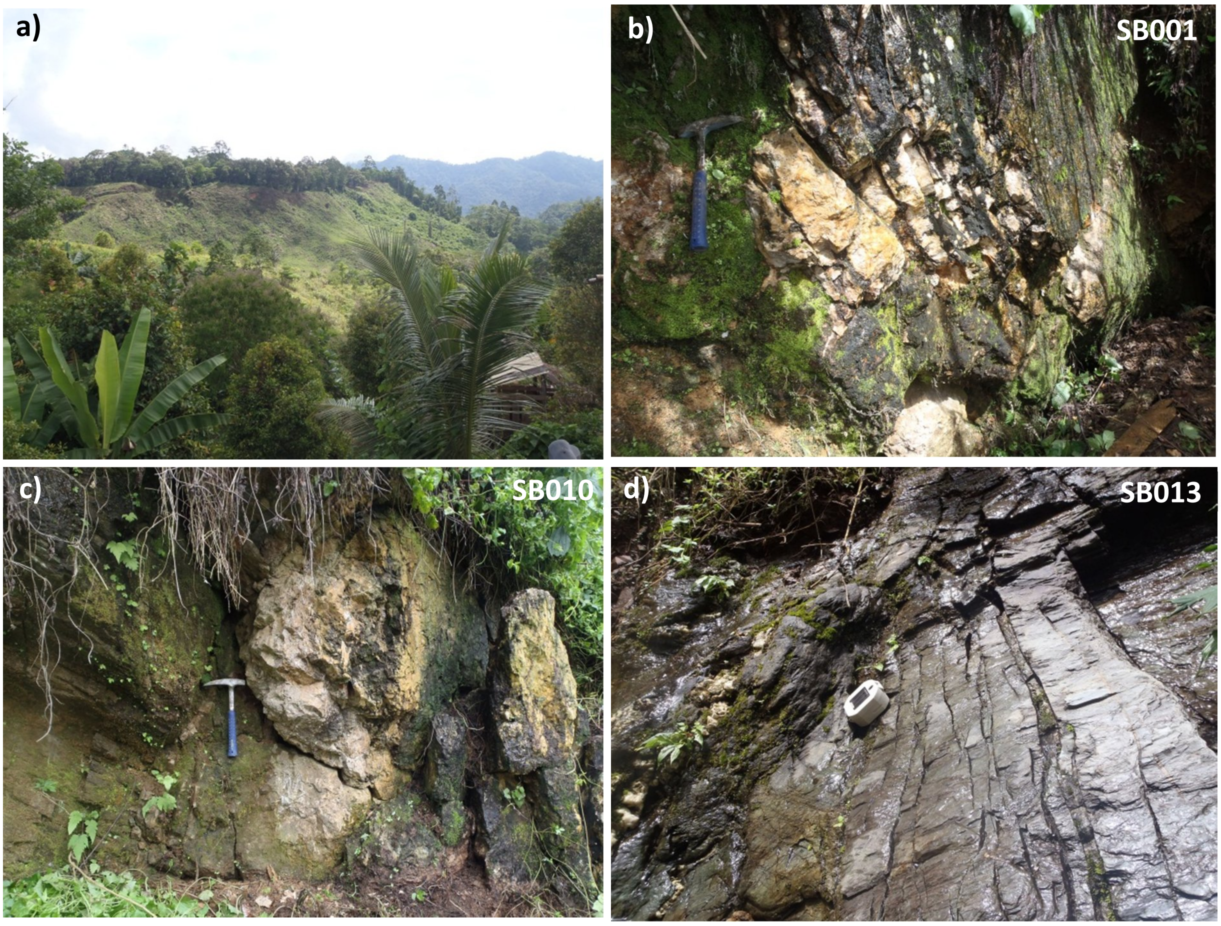

Figure 21. a) Photograph of the morphology of Kandeapi Suture which is the boundary between Latimojong Metamorphic Complex and Lamasi Complex; b) fault plane (N/74E) at SB001; c) contact plane (S/55W) between massive quartz vein and host rocks at SB010; and d) open fractures (S40W/53NE) at SB013.

The north-south trending, steeply dipping eastward ore bodies which are accompanied with brecciation and veining indicate brittle deformation took place and accompanied with gold mineralization in the Salu Bulo prospect. Contact or fault planes between ore bodies and the host rocks were observed in the field showing N/74E and S/55W at SB001 and SB010, respectively, whereas an open fracture at SB013 showing S40W/53NE (Figs. 21b-d).

An episode of late extension of brittle deformation (D3) which formed normal faulting and brecciation was reported to control gold mineralization in the Awak Mas prospect (Smillie, 1996; Archibal et. al., 1996). Simultaneously, this episode might have also controlled gold mineralization in the Salu Bulo prospect resulting the north-south trending ore bodies which formed after metamorphism of the host rocks.

CHAPTER V: ORE CHARACTERISTICS

5.1 Deposit orientation and styles

The ore bodies in the Salu Bulo prospect are north-south trending and dipping steeply eastward (Figs. 13, 22a). They are approximately three meters thick which are associated with veins, stockwork and breccias with orientations sub-parallel and discordant to the foliation of the host rocks (Figs. 22b, 23a, b).

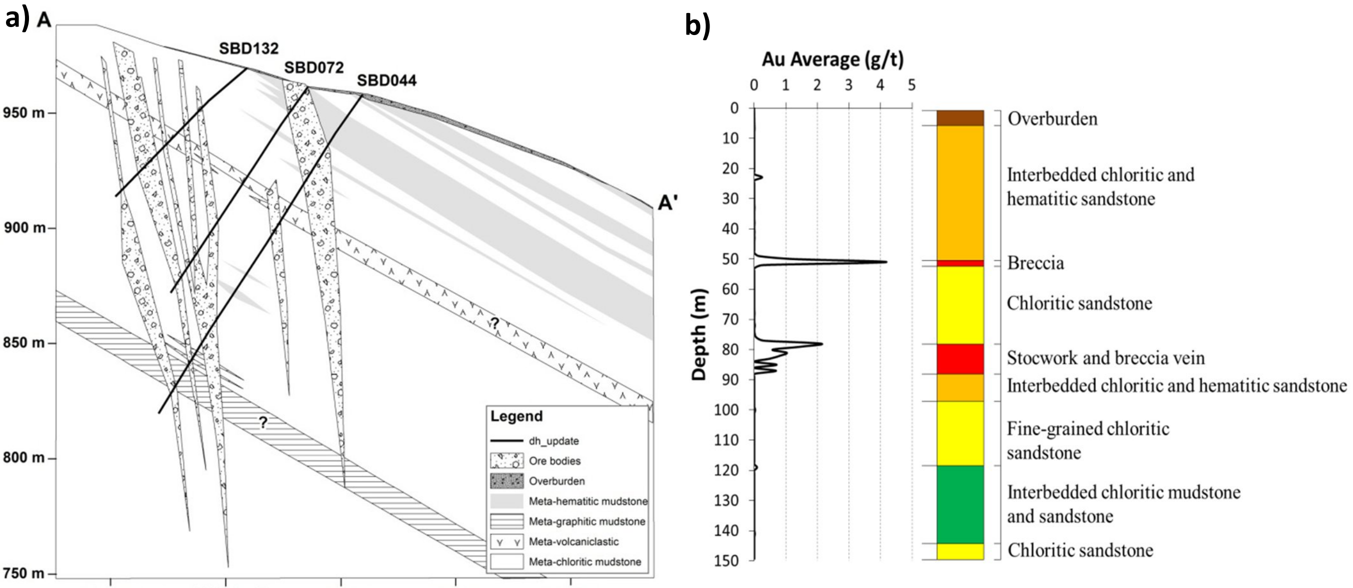

Data source: PT Masmindo Dwi Area

Figure 22. a) Section of the drill holes in the Salu Bulo prospect that show steep east-dipping mineralized zones (ore bodies) (modified from PT Masmindo Dwi Area). Location of the section line A-A' is indicated in Figure 13; and b) drill hole profile of SBD102 that intersects high gold grade related to stockwork and breccia (Data source: PT Masmindo Dwi Area).

5.2 Veins

The veins in the Salu Bulo prospect were formed by multiple events. Based on cross-cutting relationships observed megascopically and microscopically, the veins can be classified into three stages: early, main and late stages. The gold mineralization is mainly related to the main stage veins.

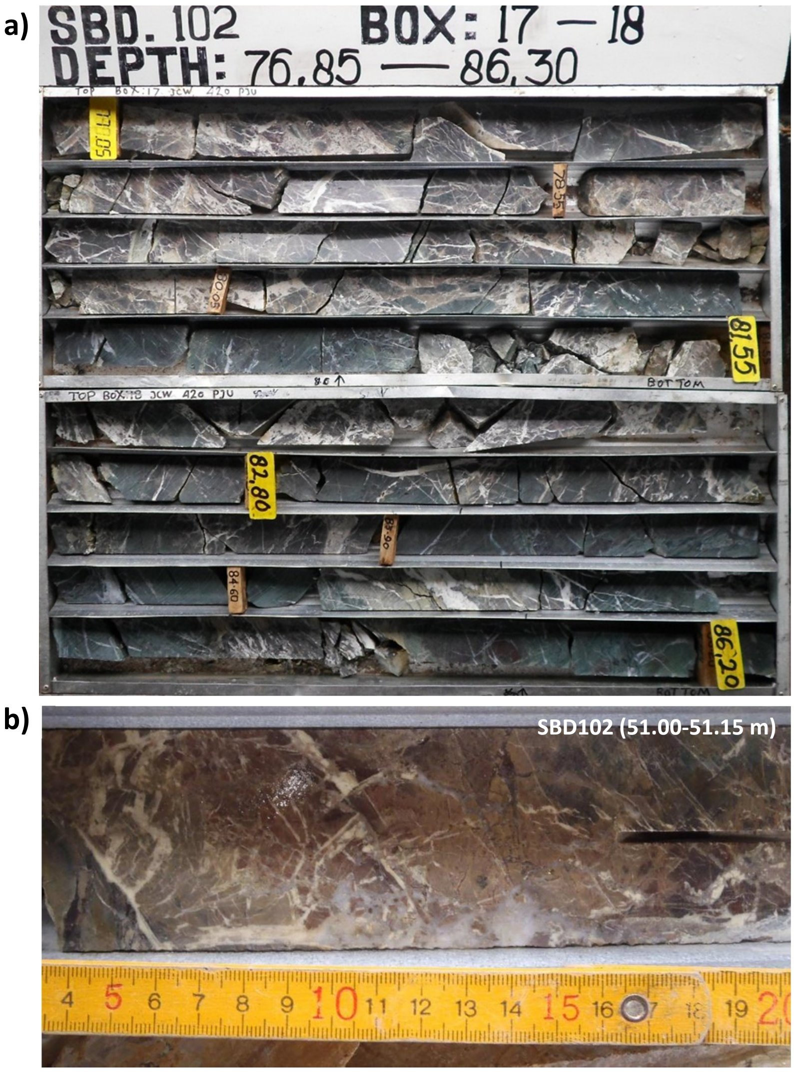

Figure 23. a-b) Photograph of drill core of SBD102 showing veins, stockwork and breccia which are related to gold mineralization in the Salu Bulo prospect (Courtesy of PT Masmindo Dwi Area).

5.2.1 Early stage veins

The early stage veins formed during metamorphism of host rocks. These veins consist of quartz and calcite that are parallel and sub-parallel to the foliation of the host rocks and that were often boudined (Figs. 24a, b). Early veins exhibit recrystallization of quartz grain such as undulose extinction, suture migration and calcite twinning. These veins are hosted in the meta-sedimentary rocks, meta-volcanic rocks and meta-volcaniclastic rocks. In the highly foliated metamorphic rock such as phyllite, quartz-ankerite±albite veins are parallel to the foliation, boudined and rarely folded and often cut by quartz-albite vein or veinlets (Fig. 24c).

Fine-grained framboidal pyrite was observed showing pressure shadow or quartz fringe.

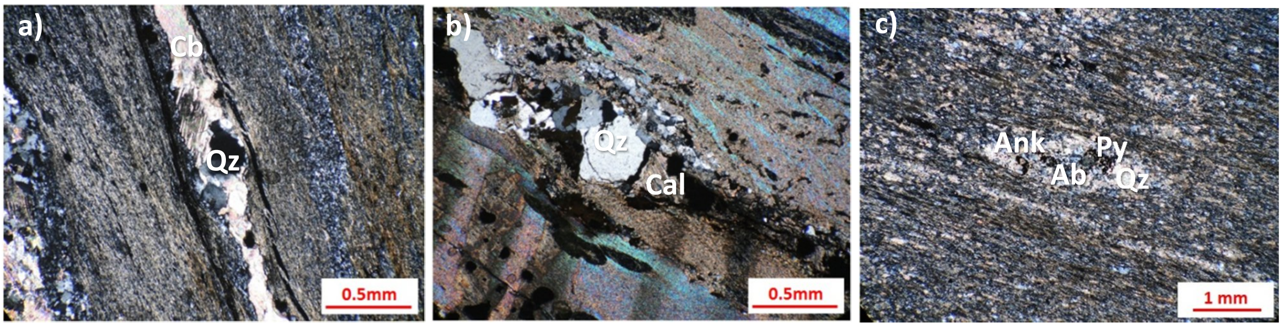

Figure 24. a) Early quartz-calcite veins parallel to the foliation hosted in meta-(graphitic) mudstone at SBD006 and b) in phyllite at SB013; and c) early quartz-ankerite-albite vein hosted in phyllite at SBD009 which is boudined and formed after fine-grained framboidal pyrite. Abbreviation: Qz (quartz); Cal (calcite); Ank (ankerite); Ab (albite); Py (pyrite).

5.2.2 Main stage veins

The veins formed within the main stage are composed of quartz, ankerite, calcite and albite (Fig. 25). Most of the main stage veins are massive in texture except for thin quartz±calcite-albite veins that exhibit comb texture in some observation. The thickness of veins ranges approximately from 0.1 cm to 2 meters. The quartz-calcite-albite crystals are prismatic with sharp straight edges. Quartz often shows undulose extinction. Few pyrite stringers related to the main stage exist in the host rocks and ores.

Based on cross-cutting relationship and vein composition, the main stage veins can be classified into five veins namely (i) quartz-ankerite±albite vein; (ii) ankerite±quartz±albite vein; (iii) quartz±calcite-albite vein; (iv) quartz-calcite(±ankerite)-albite vein; and microcrystalline quartz-calcite vein (Fig. 25). Alteration mineral assemblage in the alteration halo is identical to the vein composition.

Veins (i) are mainly composed of quartz and ankerite minerals which is likely in the edge of vein and rarely albite (Figs 25a-c). They are hosted in meta-sedimentary rocks and meta-volcanic rocks, veins are discordant to the foliation. The veins accompany lesser alteration halo. Ore minerals are mainly pyrite with lesser chalcopyrite. They are megascopically massive in texture and microscopically mosaic in texture. The veins contain rutile.

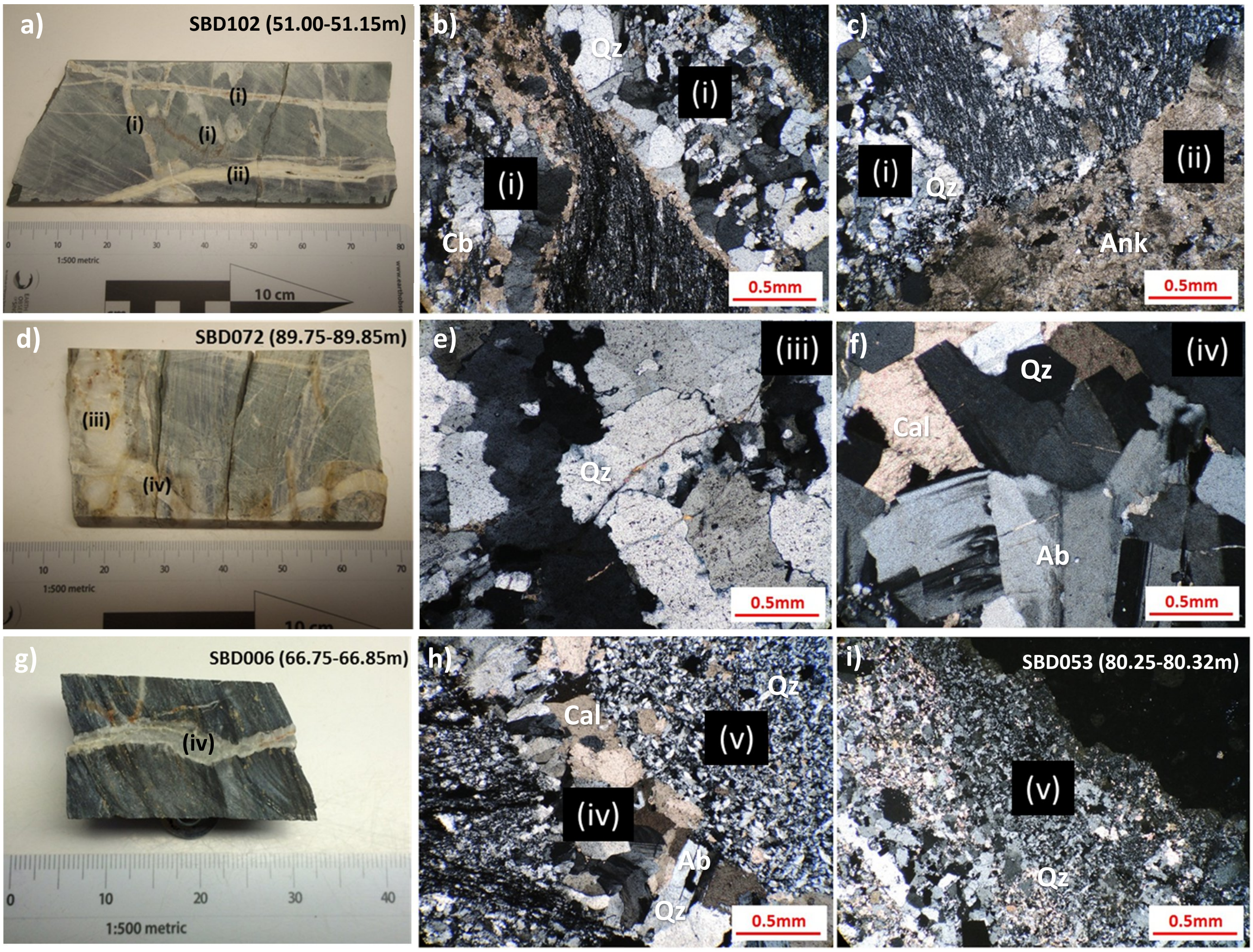

Figure 25. Photographs and photomicrographs of the main stage veins showing multiple veins events a-c) quartz-ankerite ± albite vein (i) cut by ankerite ± quartz ± albite vein (ii) hosted in meta-chloritic mudstone; d-f) quartz ± calcite-albite vein (iii) cut by quartz-calcite-albite vein (iv) hosted in meta-(chloritic) mudstone; g-i) quartz-calcite-albite vein (iv) and microcrystalline quartz-calcite vein (v) hosted in phyllite. Abbreviation: Qz (quartz); Cal (calcite); Ab (albite); Ank (ankerite).

Veins (ii) are mainly composed of ankerite with quartz and albite minerals (Fig. 26c). They cut veins (i) and cut by veins (iii), (iv) and (v) in meta-volcanic rock. They are hosted mainly in meta-volcanic rocks and meta-(chloritic) mudstone. In the alteration halo, carbonatization is major along with quartz and albite. Veins (ii) are massive in texture with lesser crustiform texture and are present as clast in the breccia. The veins contain rutile.

Veins (iii) are mainly composed of quartz along with calcite and albite in the thinner veins. They exhibit massive texture (Figs. 25d, e). The thickness of veins (iii) is up to 2 m in the outcrop SB001 and SB010 (Figs. 21b, c). Veins are thicker if more abundant quartz with silicified alteration halo with lesser albite. In thinner veins, albite and calcite are often occurred along with quartz. The quartz crystals are euhedral to anhedral in shape, showing undulose extinction and lesser recrystallized. They cut veins (ii) and cut by veins (iv). The veins (iii) occur as clasts in breccia and veins (v). They are hosted in all type of host rocks with mainly silicified alteration halo.

Veins (iv) are mainly composed of quartz, calcite and/or ankerite and albite showing euhedral to anhedral in shape (Figs. 25d, f-h). They are massive to comb in textures with calcite and albite growth at the edge of vein. They cut veins (ii) and (iii) in meta-sedimentary rocks, meta-volcanic rocks and meta-volcaniclastic rocks. They are discordant to the foliation. The veins (iv) are associated with reopening of fracture filling (Figs. 25g, h).

Veins (v) are composed of microcrystalline quartz-calcite showing grey color megascopically (Figs. 25g-i). The breccia contains clast of early veins (ii), (iii) and the vein (v) were formed after veins (iv) in open seal fracture. They are associated with silicification of host rocks along with the veins (iii).

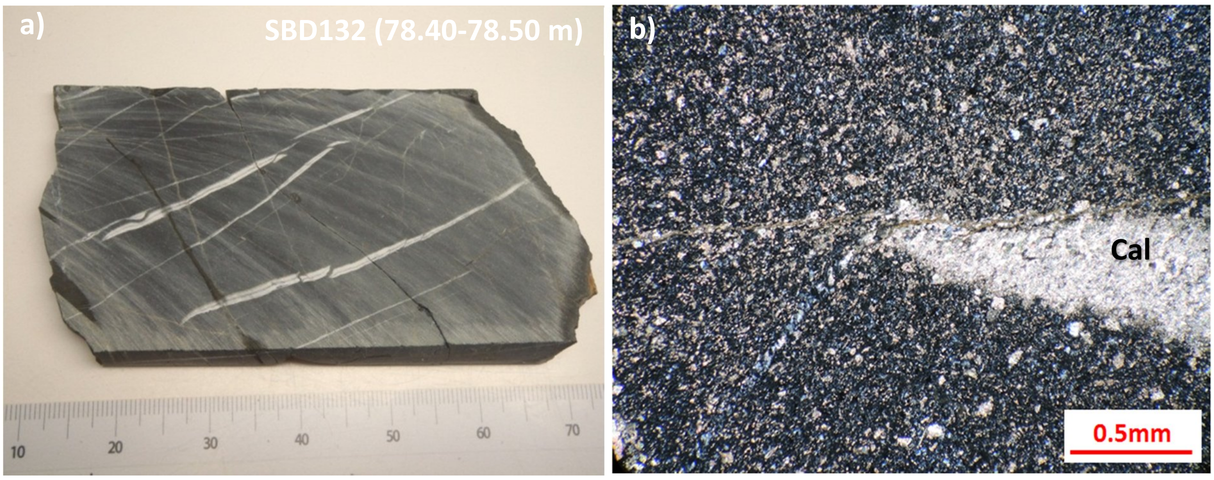

Figure 26. Calcite vein of late stage hosted in unaltered (carbonaceous) siltstone. Abbreviation: Cal (calcite).

5.2.3 Late stage veins

The veins formed during the late stage are calcite veins that are not related to gold mineralization (Fig. 26). They exist in the unaltered host rocks.

5.3 Breccia

The breccias were formed mainly during the main stage veining of gold mineralization in the Salu Bulo prospect (Fig. 27). They contain clasts of various altered host rocks and the early veins with angular to sub-rounded shape of various sizes (ca. 0.05 – 4.7 cm) (Fig. 27a). The clasts are mainly autochthonous and/or allocthonous and sometimes oriented. The breccias are associated with quartz, ankerite, calcite and albite. Matrix are principally composed of quartz, ankerite (and lesser calcite) and albite (Fig. 27). The mineral assemblage is an alteration product of clasts and matrix of breccia and is similar to the alteration mineral assemblage observed in the alteration halo of the main stage veins. Based on those mineral assemblages, general characteristics and relationship with the vein composition, the breccias are divided into milled and crackle breccias.

5.3.1 Milled breccia

Milled breccia is easily recognized by bleached color in outcrop and drill cores that composed of matrix quartz-ankerite-albite and pyrite (Figs. 27a-c). It consists of various altered host rocks and early vein (ii and iii). In some observations, the matrix of breccia is composed of fine-grained altered host rock, different from crackle breccia. Pyrite was formed mainly in the altered host rocks clast.

5.3.2 Crackle breccia

The matrix of crackle breccia is white in color that contains larger crystal grain than in the milled breccia (Fig. 27f). Interstices between the breccia clasts were cemented by a mixture of quartz, calcite, ankerite and albite crystals, which is the same mineral assemblage in the main stage veins (iv). Quartz and albite crystals grew from the edge of breccia clasts and exhibit euhedral-subhedral shape indicating that they were crystallized from solution (Fig. 27f). On the other hand, the main stage veins (v) are also accompanied with breccia that consists of microcrystalline quartz-calcite matrix and clast of the main stage veins (ii, iii) (Figs. 27h, i). This breccia is rarely observed.

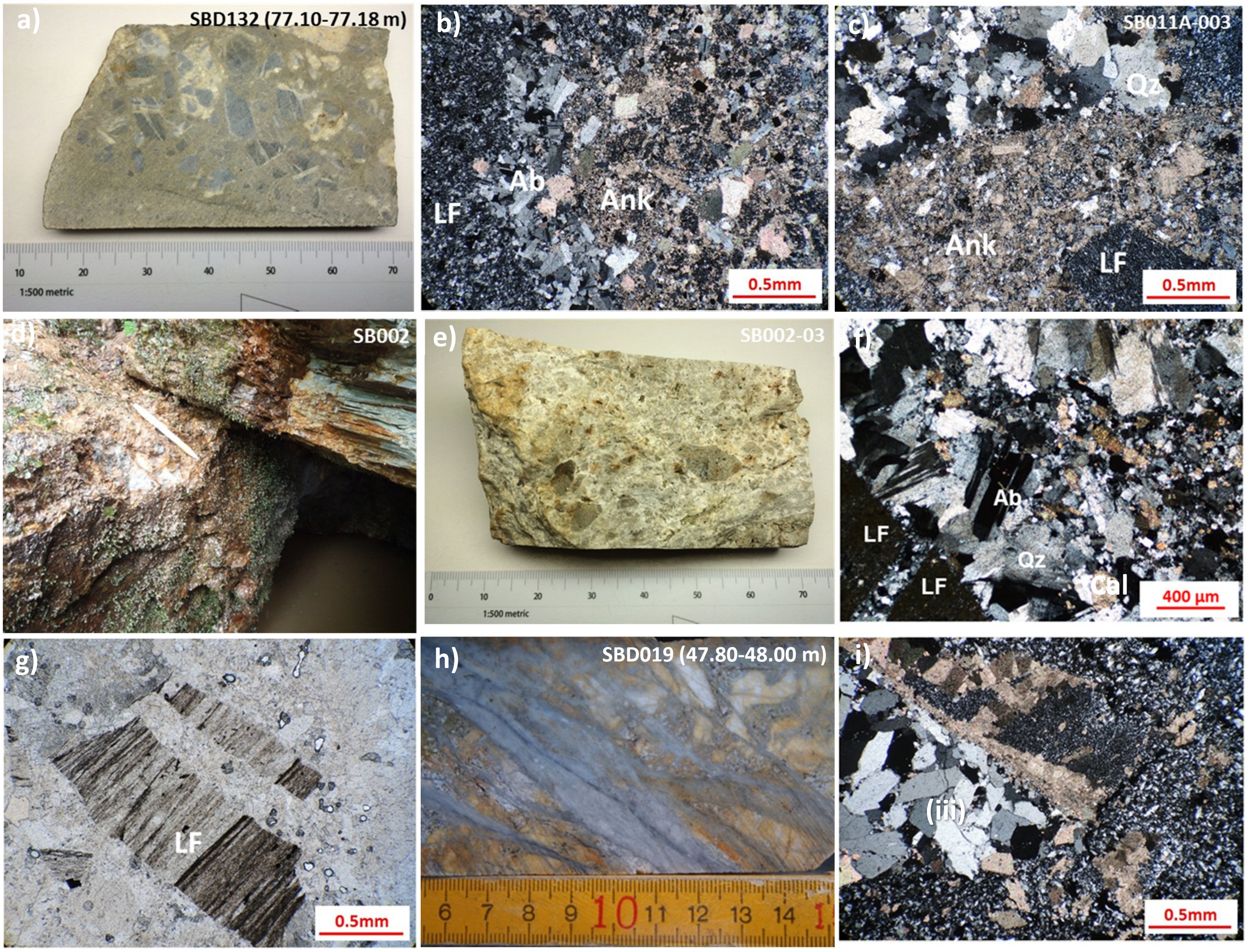

Figure 27. Photographs and photomicrographs of breccia in the Salu Bulo prospect showing identical mineral compositions to main stage veins. a-c) milled breccia that was cemented by ankerite±quartz±albite related to vein (ii), with variously altered clast of breccia and clasts of an early veins (i); d-g) crackle breccia that was cemented by quartz-calcite-albite that related to vein (iv); and h-i) breccia that was cemented by microcrystalline quartz-calcite vein (v). Abbreviation: Qz (quartz); Ab (albite); Ank (ankerite); Cal (calcite); LF (lithic fragment).

5.4 Structural analysis of the ores

Multi-phase veining stages and breccia formations in the Salu Bulo prospect indicates that re-activation occurred in the same fluid pathway to form gold mineralization in the Salu Bulo prospect (Figs. 25, 27). Preserved foliation in clast of breccia indicates that it was formed after ductile deformation (D2) (Fig. 27g). Hydrothermal fluid likely filled the foliation as to form sub-parallel and parallel of the foliation of main stage veins during brittle deformation (D3). It often connects to main stage veins that cut foliation (Fig. 28).

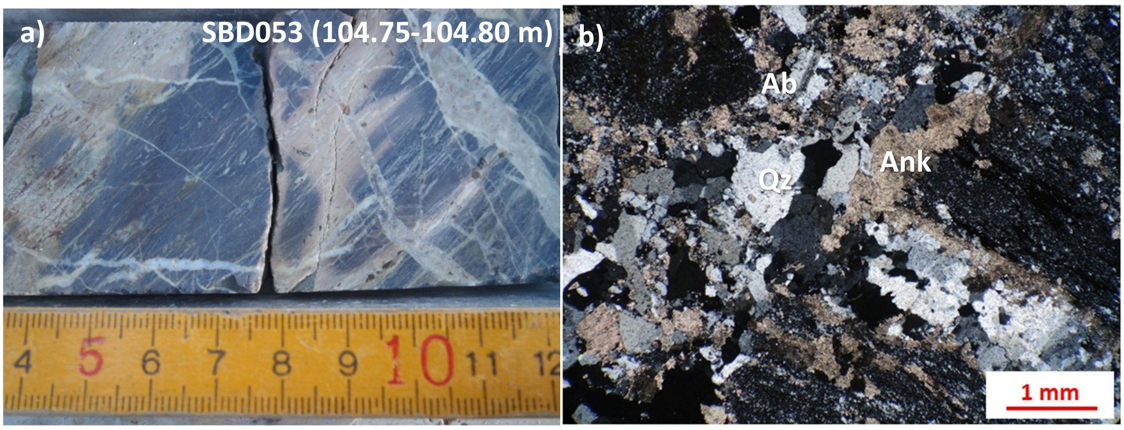

Figure 28. a) Photographs of meta-(graphitic) mudstone (phyllite) showing the main stage veins are parallel and cross cut the foliation at SBD053; b) and photomicrographs quartz-ankerite±albite vein which is parallel and cross cut the foliation. Abbreviation: Qz (quartz); Ank (ankerite); Ab (albite).

CHAPTER VI: ALTERATION, MINERALIZATION AND PARAGENESIS

6.1 Hydrothermal alteration

In the drill cores and outcrops, alteration is recognized as bleaching of host rocks (Fig. 29). Alteration halo occurred in millimeter to centimeter scale along the veins, and it is thicker in more permeable host rocks such as meta-sandstone. Porosity and/or permeability of the host rocks are one of the parameters for the hydrothermal fluid to penetrate to create the alteration along with fracturing during veining and breccia formations. Whereas, an absence of alteration halo along the main stage veins was often observed.

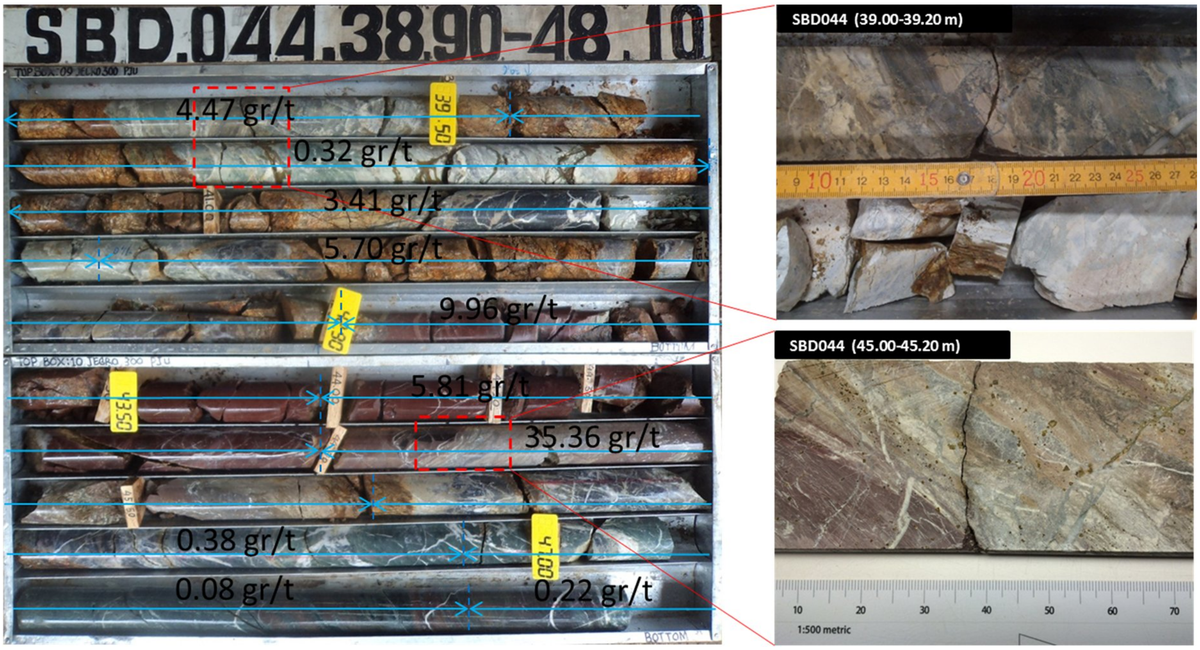

Figure 29. Photograph of drill core of SBD044 showing signature of hydrothermal alteration (Courtesy of PT Masmindo Dwi Area).

Gold mineralization in the Salu Bulo prospect mainly occurred in the alteration halo along the main stage veins and stockwork and breccia. High gold grade mineralization in the Salu Bulo prospect is associated with intense alteration such as carbonatization, albitization, silicification and sulfidation along the main stage veins and stockwork and breccia (Fig. 29). Alteration mineral assemblages in the alteration halo and breccia are identical to the mineral assemblage of veins of the main stage, namely ankerite (±calcite), quartz, albite and pyrite along with minor sericite (Figs. 25, 27, 28). Clasts in the breccia were also hydrothermally altered variously (Figs. 27a, e). In some observations, alteration mineral assemblages are superimposed on the metamorphic mineral assemblage.

6.1.1 Carbonatization

Ankerite is the most prominent carbonate mineral in this alteration part. It is observed along with lesser calcite. Carbonatization dominantly occurred along main stage vein (ii) that mainly consists of ankerite (Fig. 30). Albite and quartz accompanied carbonatization in all host rocks.

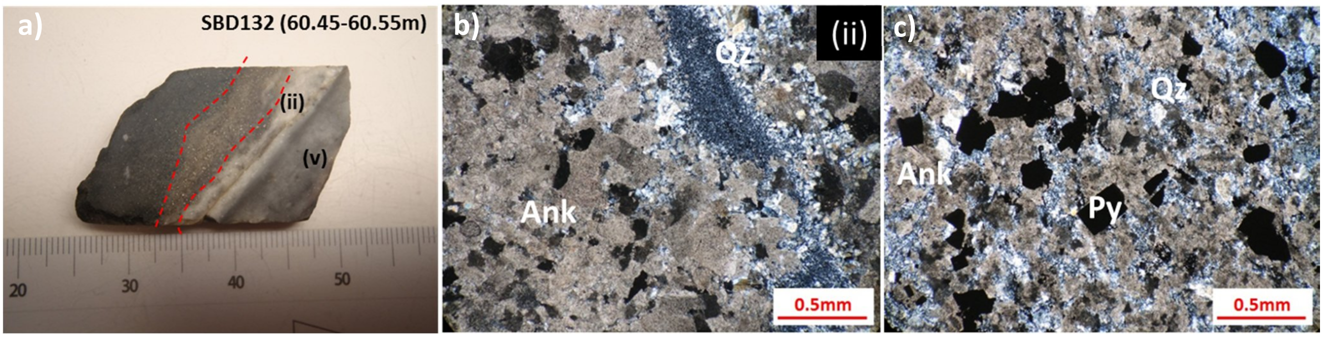

Figure 30 a-c) Intense of carbonate alteration along main stage vein (ii) consisting of mainly ankerite along with quartz and pyrite. Abbreviation: Qz (quartz); Ank (ankerite); Py (pyrite).

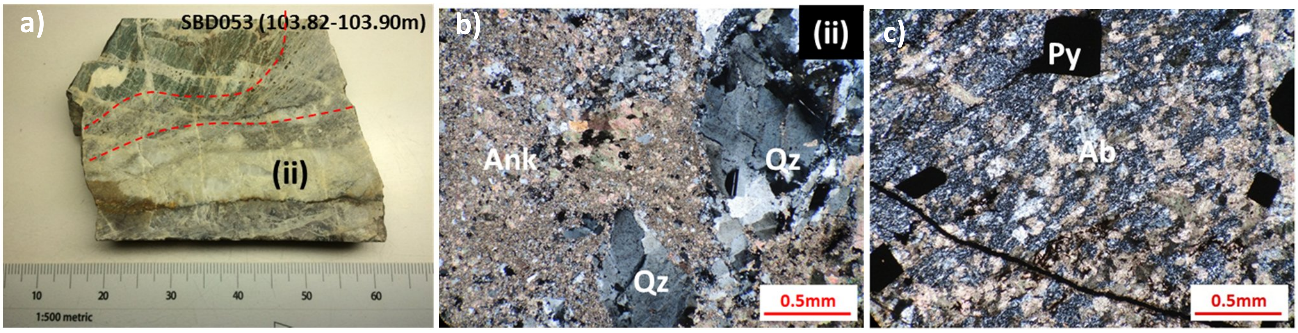

Figure 31. a-c) Albite alteration along main stage vein (ii) consisting of albite, ankerite, quartz and pyrite. Abbreviation: Qz (quartz); Ank (ankerite); Py (pyrite).

6.1.2 Albitization

Albite alteration occurred together with quartz and ankerite (Fig. 31). It is mainly in the alteration halo of the vein that is composed of albite such as the main stage veins ii and iv (Figs. 31a, c) The crystal shape is subhedral-anhedral and often occurred with ankerite. Albite alteration is observed in all type of host rocks.

6.1.3 Silicification

Silicification was observed along the main stage veins iii and v. It is composed mainly of quartz along with albite and calcite. In one of the old artisanal gold mines that were operated by the local community surrounding the mine area, a massive quartz vein (iii) around two meters thick is enveloped by an alteration halo consisting of quartz and lesser albite along with pyrite, galena, chalcopyrite and tennantite (Fig. 32). They occur along with native gold and electrum filling fractures and pores in pyrite crystals. Silicification is observed mainly in the clast of breccias.

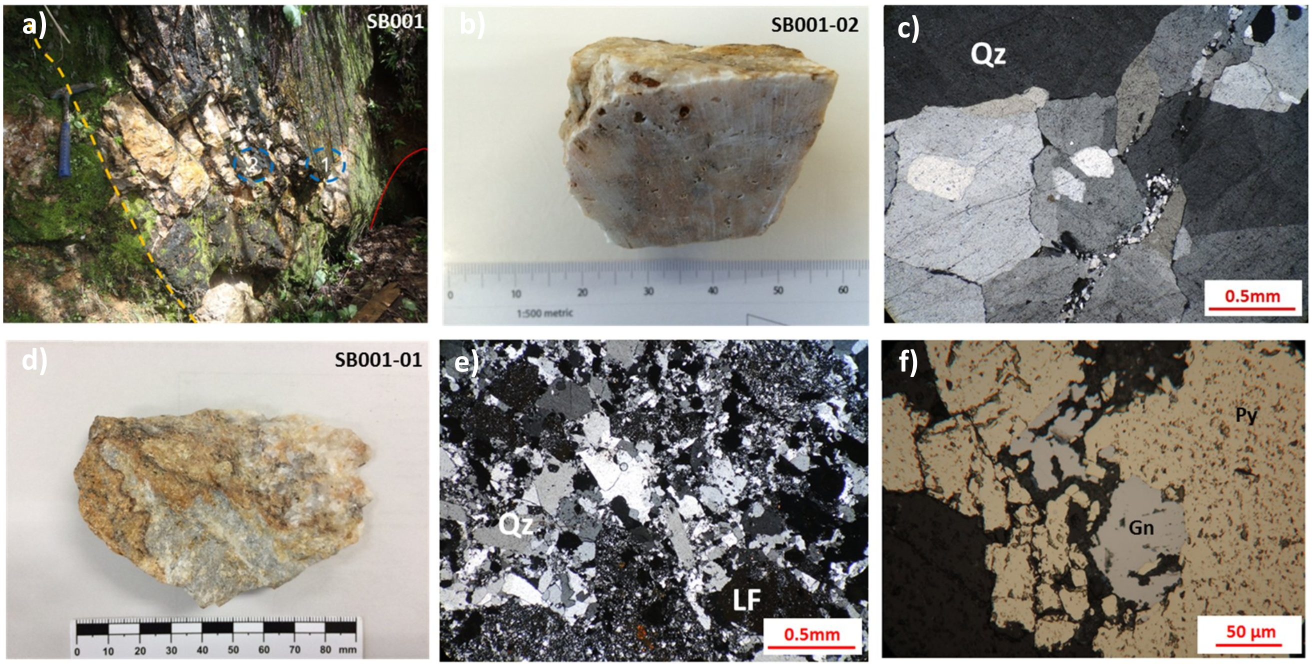

Figure 32. a) Photograph of an outcrop of massive quartz vein (iii) in one of old artisanal mine (red line), showing location samples for oxygen isotope and fluid inclusion analyses which are shown in Figure 32b and d; b) rock slab of massive vein (iii) in point 2 in Figure 33a; c) photomicrograph of sample in Figure 32b that consists of mainly quartz; d) rock slab of alteration halo along massive quartz vein in point 1 in Figure 32a; e) photomicrograph of sample in Figure 32d which mainly consists of quartz, lithic fragment; and f) photomicrograph sample in Figure 32d showing pyrite and galena. Abbreviation: Qz (quartz); Py (pyrite); Gn (galena); LF (lithic fragment).

6.1.4 Sulfidation

Pyrite was mainly formed in the alteration halo and clast and matrix of breccias (Fig.

33). It is absent or minor in the veins. Pyrite is more abundant in the mafic host rocks that are rich in iron content such as meta-(hematitic) mudstone, meta-(chloritic) mudstone, meta-volcanic rocks and meta-volcaniclastic rocks. It is associated with ankerite in the alteration halo along the veins. On the other hand, pyrite was also formed during formation of the host rocks such as fine- and medium-grained pyrite that exhibits framboidal texture. Pyrite that was formed during hydrothermal activity has euhedral shape, is less porous and is mainly in the alteration halo and ores (Fig. 33).

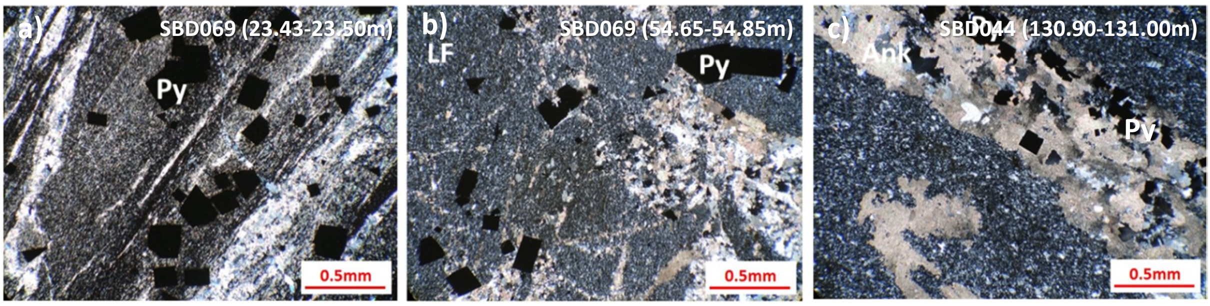

Figure 33. Photomicrograph of pyrite that occurred mainly in the alteration halo of ankerite±quartz±albite vein (ii) in meta-(hematitic) mudstone (a), clast of breccia that consists of quartz-ankerite±albite matrix (b); and contact between host rock and ankerite±quartz±albite vein (ii). Abbreviation: Ank (ankerite); Py (pyrite); LF (lithic fragment).

6.2 Ore mineralogy

Pyrite is the most abundant sulfide occurring in the altered host rocks and ores (Fig. 34). It commonly occurs as euhedral cubic to anhedral crystals and is also aggregated. Disseminated pyrite is more abundant in altered host rocks than in the veins (Fig. 34). The size of pyrite ranges from ca. 1 µm to 4 mm (Fig. 34d). Pyrite shows various morphologies and textures such as porous, deformed and massive aggregates (see next chapter). The aggregated fine-grained pyrite in host rocks exhibits layering and framboidal textures. Porous pyrite occurs in the host rocks and ores. Deformed pyrite caused by rotation, fracturing or brecciation often occurs in the ores. On the other hand, in intensely foliated meta-(graphitic) mudstone (phyllite), pyrite exhibits boudinage aggregate texture.

Gold (<2-42 µm in size) mainly fills fractures and pores in the deformed and porous pyrite, respectively, and the gap between pyrite grains which is mainly hosted in the alteration halo of the main vein and stockwork and breccia than in veins (Fig. 35). Lesser amounts of tennantite-tetrahedrite, chalcopyrite, bornite, galena, hematite and rutile are also present as inclusions in pyrites, and as discrete disseminated minerals in altered host rocks, veinlets and matrix of breccia (Fig. 36).

Figure 34. a-d) Pyrite as the most sulfide mineral in the Salu Bulo prospect that occurred mainly in altered host rocks.

Chalcopyrite is a common sulfide mineral after pyrite occurred as inclusion in pyrite and a discrete mineral in the altered part of host rocks and veinlet. It was formed along with bornite and other copper-bearing minerals. Tennantite-tetrahedrite is associated with chalcopyrite which was formed relatively late. It is also common as a discrete mineral that was formed relatively late in the hydrothermal activity and associated with carbonate mineral and hematitic rocks. Coarser grain galena was formed after pyrite in the silicification accompanied by veins (iii) and common as inclusion in pyrite in all altered part. In the supergene process, covellite and chalcocite were formed on the rim and replacement minerals in the chalcopyrite. Hematite occurred as an oxidation product that probably replaced pyrite.

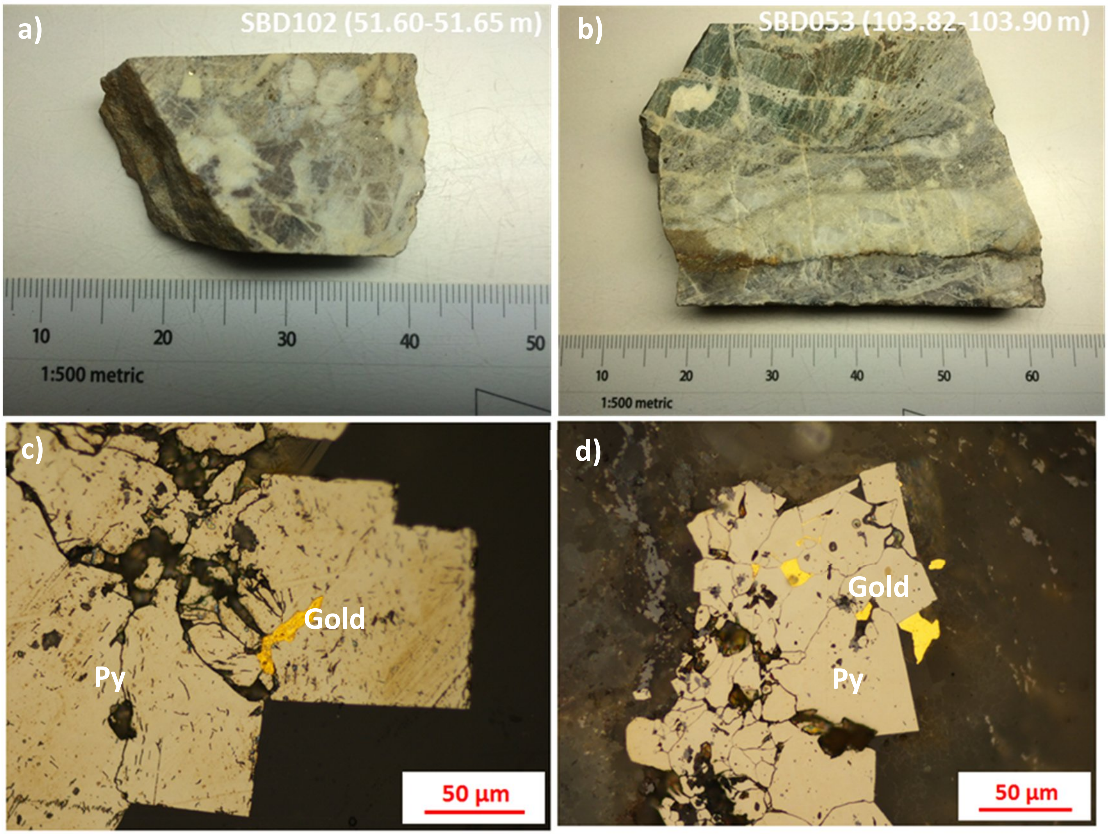

Figure 35. Photograph of breccia (a) and main stage vein (ii) (b) which host pyrite in Figure 35c and d, respectively. Photomicrographs of gold as filling pore and fracture of pyrites in breccia in Figure 35a (c) and alteration halo of ankerite±quartz±albite vein (ii) in Figure 35b (d). Abbreviation: Py (pyrite).

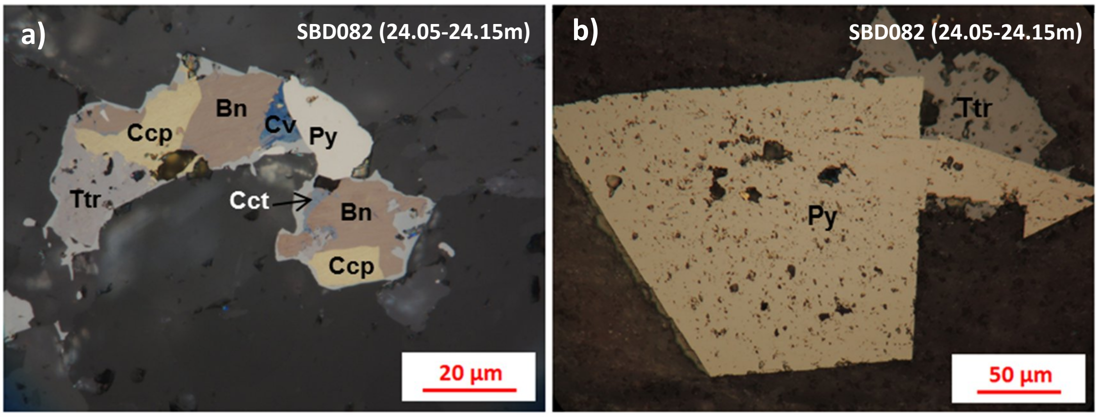

Figure 36. a-b) Photomicrograph of tetrahedrite, chalcopyrite, bornite, covellite and chalcocite of carbonate vein (ii) in meta-(hematitic mudstone). Abbreviation: Py (pyrite); Ttr (tetrahedrite); Ccp (chalcopyrite); Bn (bornite); Cv (covellite); Cct (chalcocite); and Gn (galena).

6.3 Paragenetic sequence

Minerals of host rocks and minerals formed during hydrothermal activity in the Salu Bulo prospect are summarized in Figure 37. Meta-sedimentary rocks consist of graphite, hematite, quartz, calcite, chlorite, prehnite or pumpellyite, illite or muscovite and lesser plagioclase along with pyrite. Phyllite occurred as increasing metamorphic grade of meta-(graphitic) and -(hematitic) mudstone. It mainly consists of segregation of quartz, graphite and/or hematite, containing more illite or muscovite, ankerite±calcite and albite. Meta-volcanic rocks and meta-volcaniclastic rocks were intercalated to meta-sedimentary rocks during metamorphism of the cover sequence of Latimojong Metamorphic Complex. The meta-volcanic rock consists of plagioclase, altered pyroxene to chlorite, calcite, sericite, prehnite or pumpellyite?, epidote, hematite and pyrite, whereas meta-volcaniclastic rock consists of fine ash material, illite, chlorite, augite, calcite, quartz, plagioclase, lithic fragment, prehnite or pumpellyite, epidote and pyrite.

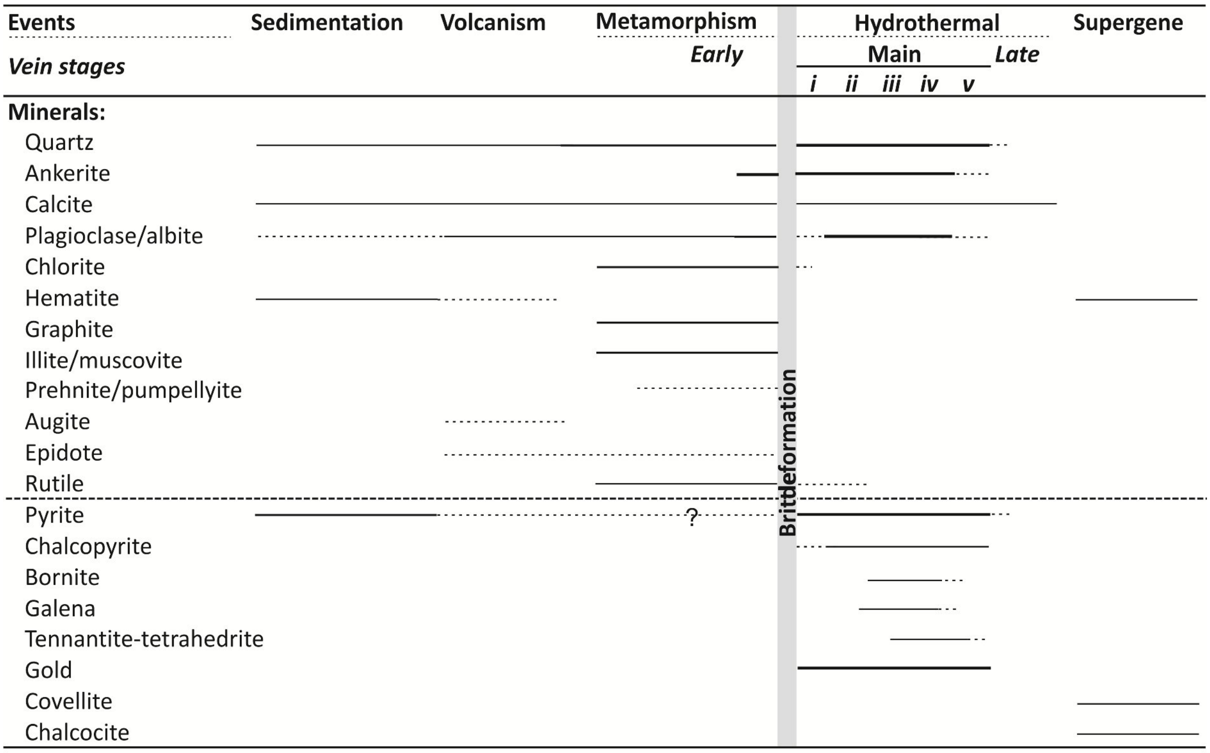

Figure 37. Paragenetic sequence of the Salu Bulo prospect.

The vein mineralogy is mainly composed of quartz, ankerite, calcite and albite. These minerals were formed during early to late stage of veining. Most sulfide minerals occurred during the hydrothermal process that was related to main stage veins. On the other hand, pyrite was formed in wide range of formation process. It formed during sedimentary and diagenetic process to form fine-grained (framboidal) and medium-grained pyrites and probably during metamorphism which shows boudined, pressure shadow or quartz fringe that was related to early quartz-ankerite±albite veins and orientation of core of porous pyrite which is parallel to the foliation.

Mineral assemblages of hydrothermal alteration are identical to the mineral composition of the main stage veins, namely quartz, ankerite (±calcite), albite and pyrite along with minor sericite. These minerals formed proportionally in the alteration halo of the main stage vein depend on the vein composition namely i.e. carbonatization, silicification, albitization and sulfidation. Gold was introduced mainly in hydrothermal phase having a spatial relationship with pyrite as fracture and pore filling in deformed and porous pyrite, respectively, and inclusions.

CHAPTER VII: WHOLE-ROCK GEOCHEMISTRY AND MINERAL CHEMISTRY

7.1 Major and trace elements

Major, trace and rare earth elements composition of host rocks, hydrothermally altered host rocks and ores in the Salu Bulo prospect are summarized in Table 4.

7.1.1 Unaltered host rocks

The SiO_2 content of the unaltered host rocks ranges from 41.0 to 56.5 wt%, the Al_2O_3 content ranges from 11.4 to 18.5 wt%, the Fe_2O_3 content ranges from 5.7 to 10.2 wt%, the MgO content ranges from 1.9 to 6.8 wt%, the CaO content ranges from 2.2 to 17.5 wt%, the Na_2O content ranges from 1.6 to 6.8 wt%, the K_2O content ranges from 0.03 to 3.8 wt%, the LOI content ranges from 4.1 to 16.1 wt% and the Fe/(Fe+Mg) molar ratio ranges from 0.6 to 0.8 (Table 4). The Ni content of unaltered host rocks ranges from 43.4 to 162.1 ppm, the As content ranges from 3.7 to 196.4 ppm, the Sb content ranges from 0.6 to 1.3 ppm, the Ba content ranges from 53 to 552 ppm, the Mo content ranges from 0.6 to 14.4 ppm, the W content ranges from 0.8 to 7.2 ppm, the Co content ranges from 8.1 to 33.4 ppm and the Hg content ranges from <0.01 to 0.02 ppm (Table 4).

7.1.2 Altered host rocks and ores

The SiO_2 content of the least and intensely altered host rocks and ores ranges from 53.2 to 58.3 wt%, 44.1 to 61.1 wt% and 43.8 to 77.4 wt%, respectively, the Al_2O_3 content ranges from 15.8 to 20.9 wt%, 9.9 to 17.5 wt%, 6.7 to 15.4 wt%, the Fe_2O_3 content ranges from 7.1 to 10.0 wt%, 4.0 to 6.1 wt%, 1.9 to 8.4 wt%, respectively, the MgO content ranges from 1.1 to 2.9 wt%, 0.6 to 4.5 wt%, 0.7 to 5.0 wt%, respectively, the CaO content ranges from 0.8 to 2.7 wt%, 1.2 to 9.6 wt%, 1.7 to 11.4 wt%, respectively, the Na_2O content ranges from 3.2 to 9.2 wt%, 5.7 to 10.2 wt%, 0.1 to 8.2 wt%, respectively, the K_2O content is ranges from 0.1 to 3.8 wt%, 0.1 wt%, 0.02 to 1.24 wt%, respectively, the LOI content ranges from 3.4 to 6.34 wt%, 4.1 to 14.4 wt%, 3.2 to 16.5 wt% and the Fe/(Fe+Mg) molar ratio ranges from 0.8 to 0.9, 0.6 to 0.9 and 0.5 to 0.8, respectively (Table 4).

The Ni content of the least and intensely altered host rocks and ores ranges from 117.1 to 149.8 ppm, 65.4 to 223.1 and 54.3 to 332.9 ppm, respectively, the As content ranges from 2.9 to 6.0 ppm, 4.0 to 36.4 ppm and 4.5 to 97.1 ppm, respectively, the Sb content ranges from 0.9 to 2.5 ppm, 2.9 to 18.8 ppm and 0.6 to 9.0 ppm, respectively, the Ba content ranges from 24 to 550 ppm, 14.0 and 8.0 to 143.0 ppm, respectively, the Mo content ranges from 1.7 to 5.7 ppm, 3.2 to 8.5 and 1.2 to 8.6 ppm, respectively, the W content ranges from 4.3 to 23.3 ppm, 8.2 to 49.2 ppm and 4.2 to 89.7 ppm, respectively, the Co content ranges from 12.5 to 24.4 ppm, 6.3 to 26.2 ppm and 6.6 to 29.7, respectively and the Hg content ranges from 0.02 to 0.06 ppm, 0.02 to 0.17 ppm and <0.01 to 0.19 respectively (Table 4).

7.2 Rare earth elements (REE)

The rare earth element (REE) content of host rocks, hydrothermally altered host rocks and ores are summarized in Table 4. Post-Archaean average Australian sedimentary rock (PAAS) (McLennan, 1989) was used to normalize REE concentration of unaltered and altered host rocks and ores.

7.2.1 Unaltered host rocks

The total rare earth element (ΣREE) contents of meta-mudstone, meta-sandstone and meta-volcanic rock and meta-volcaniclastic rock range from 61.3 to 104.5 ppm, 53.2 to 81.3 ppm and 46 to 59.9 ppm, respectively (Table 4). PAAS normalized REE plots of host rocks show depleted light rare earth element (LREE) and sub-horizontal high rare earth element (HREE) patterns, a part of sample SB021 (Figs. 38a-c). Europium (Eu) positive anomalies are only shown by meta-sandstone and sample number SB003, with Eu/Eu* varying from 0.1 to 0.2, normalized lanthanum over ytterbium (La/Yb)N ratios between 0.1 and 0.4 and normalized lanthanum over lutetium (La/Lu)N ratios between 0.1 and 0.3 (Table 4, Figs. 38a-c).

7.2.2 Altered host rocks and ores

The ΣREE values of least altered host rocks range from 88.3 to 131.8 ppm (Table 4). PAAS normalized REE plots of least altered host rocks show depleted LREE and sub-horizontal HREE patterns (Fig. 38d). There are no characteristics including the Eu positive anomaly, with Eu/Eu* varying from 0.07 to 0.09, (La/Yb)N ratios between 0.2 and 0.6 and (La/Lu)N ratios between 0.2 and 0.6 (Table 4, Fig. 38d).

The ΣREE values of intensely altered host rocks range from 20.1 to 112.1 ppm (Table 4). PAAS normalized REE plots of host rocks show slightly to strongly depleted LREE and sub-horizontal HREE patterns (Fig. 38e). There are no characteristics including the Eu positive anomaly, with Eu/Eu* varying from 0.07 to 0.09, (La/Yb)N ratios between 0.2 and 0.6 and (La/Lu)N ratios between 0.2 and 0.6 (Table 4, Fig. 38e).

The ΣREE values of ores range from ppm and 14.7 to 164.9 ppm (Table 4). PAAS normalized REE plots of intensely altered host rocks and ores show depleted LREE and sub-horizontal HREE patterns (Fig. 38f). The most important characteristics including the Eu positive anomaly, with Eu/Eu* varying from 0.08 to 0.6, (La/Yb)N ratios between 0.08 and 0.9 and (La/Lu)N ratios between 0.07 and 0.7 (Table 4, Fig. 38f).

Table 4. Major, trace and rare earth elements composition of host rocks, hydrothermally altered host rocks and ores in the Salu Bulo prospect.

Lithology	**Meta-mudstone**			**Meta-sandstone**		**Meta-volcanic rock & meta-volcaniclastic rocks**		**Least altered host rocks**			**Intensely altered host rocks**			**Ores**									
Sample No.	SB 002	SB 021	SB 023	SB 015	SB 022	SB 003	SB 006	SB 001	SB 004	SB 005	SB 007	SB 008	SB 014	SB 009	SB 010	SB 011	SB 012	SB 013	SB 016	SB 017	SB 018	SB 019	SB 020
wt%																							
SiO_2	47.3	41.0	56.5	55.1	50.9	44.8	50.3	58.3	53.2	55.2	61.1	61.1	44.1	43.8	55.5	54.6	62.2	50.7	77.4	57.3	59.0	46.3	47.7
Al_2O_3	16.1	11.4	18.5	14.9	16.4	17.2	15.7	17.7	15.8	20.9	17.5	9.9	13.2	8.9	10.0	10.1	6.7	15.4	9.4	8.7	13.8	13.0	11.3
Fe_2O_3	9.6	5.7	7.1	8.4	9.4	8.5	10.2	7.1	10.0	7.3	4.0	6.1	5.7	7.2	4.8	5.1	3.6	4.6	1.9	6.7	5.9	8.4	5.8
MgO	3.9	1.9	3.0	4.9	4.8	6.8	5.4	1.1	2.1	2.9	0.6	2.3	4.5	5.0	3.6	3.8	4.0	3.3	0.7	3.6	1.4	3.1	4.4
CaO	6.7	17.5	2.2	4.2	5.8	6.3	8.7	1.5	2.7	0.8	1.2	5.5	9.6	11.4	7.8	8.1	7.8	6.7	1.7	7.3	3.7	7.8	9.1
Na_2O	6.8	1.6	1.9	2.2	4.1	5.0	4.1	9.2	8.6	3.2	10.2	5.7	7.3	5.1	5.5	5.6	0.1	5.4	5.3	5.1	8.2	7.6	6.3
K_2O	0.3	2.6	3.8	2.0	0.8	0.5	0.03	0.3	0.1	3.8	0.1	0.1	0.1	0.03	0.1	0.1	0.2	1.4	0.03	0.02	0.04	0.04	0.1
TiO_2	1.0	0.4	0.9	0.8	0.9	1.7	0.8	1.0	0.8	0.8	0.9	0.6	0.6	0.9	0.5	0.3	0.1	0.8	0.1	0.4	0.6	1.0	0.5
P_2O_5	0.2	0.2	0.2	0.1	0.2	0.4	0.2	0.2	<0.01	0.1	0.1	0.1	0.02	0.3	0.02	0.1	0.2	0.2	0.03	0.04	0.2	0.3	0.01
MnO	0.2	1.5	0.1	0.2	0.2	0.9	0.2	0.1	0.04	0.2	0.02	0.4	0.3	0.5	0.2	0.2	0.2	0.1	0.1	0.2	0.1	0.7	0.2
Cr_2O_3	0.02	0.01	0.02	0.02	0.01	0.05	0.03	0.03	0.06	0.03	0.06	0.08	0.04	0.03	0.04	0.05	0.01	0.02	0.05	0.05	0.05	0.02	0.04
LOI	7.9	16.1	5.6	7.0	6.2	7.4	4.1	3.4	6.4	4.5	4.1	7.9	14.4	16.5	11.9	11.8	14.7	11.3	3.2	10.6	6.8	11.6	14.4
Total	99.8	99.9	99.8	99.8	99.8	99.7	99.8	99.9	99.8	99.8	99.9	99.8	99.8	99.7	99.9	99.9	99.7	99.8	100.0	99.8	99.9	99.8	99.8
TOT/C	1.8	4.0	0.7	1.1	0.7	1.0	0.3	0.7	1.8	0.3	0.7	2.4	4.1	4.7	3.3	3.4	3.5	2.8	0.8	3.1	1.4	3.1	4.1
TOT/S	0.6	<0.02	0.4	0.6	<0.02	0.0	0.3	0.3	0.1	0.1	1.3	1.9	0.3	1.7	1.1	1.2	0.0	1.2	0.7	2.8	3.4	4.05	0.5
ppm																							
Mo	2.3	0.6	14.4	1.3	1.0	1.1	2.9	5.7	5.6	1.7	8.5	6.9	3.2	2.5	2.5	4.8	1.2	1.2	8.6	8.5	7.8	2.0	3.5
Cu	135.4	5.8	29.4	88.1	90.2	859.4	144.4	19.9	44.1	150.8	28.9	258.4	112.9	59.8	32.3	33.5	3.5	49.0	9.6	11.8	312.7	61.2	75.5
Pb	4.4	10.5	33.7	10.4	4.6	3.9	8.7	4.1	3.3	4.4	5.6	5.7	3.7	7.4	6.1	11.8	13.4	6.3	2.1	7.4	40.4	11.2	3.4
Zn	70	52	95	95	82	82	76	78	179	117	32	48	46	74	32	63	66	44	17	46	23	53	43
Ni	59.1	162.1	59.2	79.5	43.4	121.1	79.8	117.1	149.8	141.0	212.3	223.1	65.4	121.6	85.0	139.0	71.4	54.3	179.0	332.9	267.0	113.8	102.7
As	20.2	5.3	196.4	15.2	8.4	3.7	14.9	6.0	3.4	2.9	4.0	36.4	7.2	10.0	9.6	21.6	4.5	22.7	9.2	6.7	97.1	35.0	16.1
Sb	0.9	1.1	0.9	0.7	0.6	1.3	1.1	1.7	2.5	0.9	2.9	18.8	5.0	9.0	7.6	5.8	1.3	9.0	0.6	1.7	4.1	2.6	3.4
Bi	0.1	<0.1	0.6	0.3	<0.1	<0.1	<0.1	0.2	<0.1	0.2	<0.1	0.2	<0.1	0.1	0.1	<0.1	<0.1	0.2	<0.1	0.2	0.2	<0.1	<0.1
Au	0.02	0.0005	<0.0005	0.004	<0.0005	<0.0005	0.005	0.05	0.2	0.006	20.1	2.9	1.3	5.7	0.9	5.6	0.2	2.0	1.7	14.2	13.0	4.6	0.4
Ag	0.1	<0.1	<0.1	<0.1	<0.1	<0.1	<0.1	0.2	<0.1	0.2	2.8	0.7	0.6	1.2	0.3	0.9	<0.1	0.4	0.3	2.2	2.7	1.2	0.2
Hg	0.02	0.01	0.02	0.01	<0.01	0.02	0.02	0.03	0.06	0.02	0.04	0.17	0.02	0.11	0.19	0.03	0.02	0.13	<0.01	0.01	0.01	0.03	0.04
Tl	<0.1	<0.1	<0.1	<0.1	<0.1	<0.1	<0.1	<0.1	<0.1	<0.1	<0.1	<0.1	<0.1	<0.1	<0.1	<0.1	<0.1	<0.1	<0.1	<0.1	<0.1	<0.1	<0.1
Se	1.0	<0.5	<0.5	<0.5	<0.5	<0.5	<0.5	<0.5	<0.5	<0.5	0.6	1.1	<0.5	<0.5	<0.5	0.9	<0.5	<0.5	<0.5	1.0	1.7	1.8	<0.5
Ba	53	342	552	214	123	69	74	33	24	550	14	14	14	12	8	8	30	143	18	9	12	8	14
Co	30.3	12.5	8.4	27.8	22.9	31.0	33.4	12.5	18.5	24.4	6.3	26.2	17.7	22.5	16.3	19.1	15.0	16.2	6.6	29.7	24.2	13.6	17.8
Cs	2.3	8.1	8.5	13.8	5.1	4.1	2.1	2.3	1.2	12.7	0.2	0.5	0.7	2.1	0.7	0.7	12.2	4.8	<0.1	0.2	0.3	0.3	0.6
Rb	10.9	92.8	104.6	60.0	23.8	20.7	0.6	11.1	1.2	124.0	1.5	1.7	2.7	0.2	1.1	1.0	6.0	47.7	<0.1	0.1	0.4	<0.1	2.2
Sr	238.5	150.1	74.8	64.3	527.8	168.4	156.5	243.1	363.5	98.8	262.8	573.6	510.4	1518.3	509.7	456.5	1192.9	355.9	150.3	630.2	387.0	684.7	425.6
V	301	104	164	190	266	214	312	223	373	198	138	108	156	63	72	47	110	163	26	48	75	113	148
W	7.2	1.8	1.0	0.8	1.2	2.3	1.5	15.2	23.3	4.3	49.2	14.5	8.2	57.5	56.5	9.8	5.3	19.2	4.2	34.8	21.2	89.7	23.5
La	9.1	22.9	14.1	13.4	7.9	5.3	6.7	10.8	19.6	25.9	17.1	22.1	2.2	30.4	1.2	2.2	4.3	26.9	3.6	5.1	15.5	8.4	1.5
Ce	19.4	41.1	34.7	27	16.5	15.6	14.5	27.3	43.3	51.6	37.3	43.8	5.1	65	2.9	4.3	7.4	57.7	7.7	9.8	24.6	16.9	3
Pr	2.6	4.72	3.72	3.42	2.25	2.59	1.93	3.56	5.18	6.03	4.32	5.21	0.63	7.6	0.48	0.66	0.86	6.67	0.88	1.16	2.97	2.5	0.45
Nd	12	18.9	14.5	15.8	10.3	12.7	8.3	17.4	20.6	24	17.6	20.9	3.5	31.9	2.5	3.2	4	27.6	3.4	5.2	12.7	11.6	2.6

Sm	3.03	3.5	3.4	3.8	2.6	4.0	2.2	4.7	4.1	4.8	3.9	4.2	1.1	6.9	0.9	1.1	0.9	5.6	0.6	1.5	3.4	3.2	1.0
Eu	1.0	0.7	0.7	1.3	0.9	1.3	0.7	0.9	0.8	1.0	0.7	1.1	0.4	1.9	0.4	0.4	0.3	1.5	0.2	0.5	1.0	0.9	0.4
Gd	3.7	3.4	3.2	4.3	3.3	4.5	2.9	5.6	4.3	4.8	3.5	4.1	1.6	6.5	1.4	1.5	1.3	5.1	0.7	2.0	3.9	3.7	1.5
Tb	0.6	0.5	0.5	0.7	0.6	0.8	0.5	1.0	0.8	0.8	0.5	0.6	0.3	0.9	0.3	0.3	0.2	0.7	0.1	0.4	0.7	0.7	0.3
Dy	3.8	3.2	3.1	4.4	3.4	5.3	3.3	6.3	5.1	4.9	3.4	3.7	1.9	5.3	1.7	1.8	1.4	3.7	0.7	2.9	4.8	4.3	2.3
Ho	0.8	0.7	0.6	0.9	0.7	1.0	0.6	1.4	1.2	1.0	0.8	0.8	0.4	1.0	0.4	0.4	0.3	0.7	0.1	0.6	1.0	0.9	0.5
Er	2.3	2.2	2.0	2.7	2.1	3.1	2.0	4.3	3.4	3.1	2.5	2.4	1.3	3.1	1.2	1.2	0.7	2.3	0.4	1.9	2.9	3.0	1.4
Tm	0.4	0.3	0.3	0.4	0.3	0.5	0.3	0.6	0.5	0.4	0.4	0.4	0.2	0.5	0.2	0.2	0.1	0.3	0.1	0.3	0.5	0.5	0.2
Yb	2.4	2.0	2.2	2.8	2.1	3.0	1.8	3.8	3.6	3.0	2.8	2.5	1.3	3.4	1.1	1.1	0.7	2.3	0.5	2.0	3.0	3.4	1.4
Lu	0.3	0.3	0.3	0.5	0.3	0.5	0.3	0.6	0.6	0.5	0.5	0.4	0.2	0.5	0.2	0.2	0.1	0.4	0.06	0.3	0.4	0.5	0.2
ΣREE	61.3	104.5	83.5	81.3	53.2	59.9	46.0	88.3	113.0	131.8	95.4	112.1	20.1	164.9	14.7	18.7	22.5	141.4	19.1	33.7	77.4	60.5	16.9
ΣLREE	46.1	91.1	70.4	63.4	39.6	40.1	33.6	63.8	92.8	112.4	80.2	96.2	12.5	141.8	8.0	11.5	17.5	124.5	16.2	22.7	59.2	42.6	8.6
ΣHREE	15.1	13.4	13.0	17.8	13.7	19.8	12.4	24.5	20.2	19.4	15.1	15.9	7.6	23.1	6.7	7.2	5.0	17.0	2.9	11.0	18.2	18.0	8.3
$(La/Yb)_N$	0.3	0.8	0.5	0.4	0.3	0.1	0.3	0.2	0.4	0.6	0.5	0.7	0.1	0.7	0.08	0.1	0.5	0.9	0.5	0.2	0.4	0.2	0.08
$(La/Lu)_N$	0.3	0.8	0.5	0.3	0.3	0.1	0.3	0.2	0.4	0.6	0.4	0.7	0.1	0.7	0.1	0.1	0.5	0.8	0.7	0.2	0.5	0.2	0.07
Eu/Eu*	0.2	0.1	0.1	0.2	0.2	0.1	0.2	0.07	0.09	0.09	0.1	0.1	0.5	0.08	0.6	0.5	0.5	0.1	0.9	0.3	0.2	0.2	0.5
Sr/Ba	4.5	0.4	0.1	0.3	4.3	2.4	2.1	7.4	15.1	0.2	18.8	41.0	36.5	126.5	63.7	57.1	39.8	2.5	8.4	70.0	32.3	85.6	30.4
Fe/(Fe+Mg)*	0.8	0.8	0.8	0.7	0.7	0.6	0.7	0.9	0.9	0.8	0.9	0.8	0.6	0.7	0.6	0.6	0.5	0.6	0.8	0.7	0.8	0.8	0.6
Au/Ag ratio	0.2	nd	nd	nd	nd	nd	nd	0.2	nd	0.0	7.2	4.1	2.2	4.7	2.9	6.2	nd	4.9	5.6	6.4	4.8	3.8	2.1

* = molar ratio; nd = not determined

Table 5. Correlation coefficients of Au and selected elements in intensely altered host rocks and ores.

	Au	*Si*	*Al*	*Fe*	*Mg*	*Ca*	*Na*	*K*	*Ti*	*Mn*	*Cr*	*Ba*	*Co*	*V*	*W*	*Mo*	*Cu*	*Pb*	*Zn*	*Ni*	*As*	*Sb*	*Ag*	*Hg*
Au	1																							
Si	0.141889	1																						
Al	0.451883	-0.20051	1																					
Fe	0.11597	-0.75512	0.039978	1																				
Mg	-0.50259	-0.74306	-0.43443	0.45562	1																			
Ca	-0.48894	-0.79883	-0.40739	**0.575516**	**0.982549**	1																		
Na	**0.579277**	-0.16864	**0.815556**	0.244208	-0.46634	-0.38564	1																	
K	-0.19931	-0.15693	0.396936	-0.16425	0.051064	0.003035	-0.10683	1																
Ti	0.384016	-0.55989	**0.68346**	**0.60039**	-0.06191	0.046202	**0.645409**	0.239724	1															
Mn	-0.25071	-0.56784	-0.23188	**0.776426**	0.453901	**0.589311**	-0.04778	-0.24547	0.440823	1														
Cr	0.388679	0.370807	0.109964	-0.02531	-0.50102	-0.47152	0.460115	-0.39471	-0.0022	-0.20424	1													
Ba	-0.21624	-0.08465	0.341122	-0.22363	0.023307	-0.02938	-0.17413	**0.993674**	0.181149	-0.26504	-0.41467	1												
Co	0.072684	-0.32168	-0.35686	**0.596346**	0.42079	0.451628	-0.18038	-0.09608	-0.00262	0.255663	0.262907	-0.11656	1											
V	-0.13773	-0.47715	**0.58383**	0.113867	0.169417	0.134243	0.21551	0.494054	0.456107	-0.00476	-0.22937	0.457129	-0.18946	1										
W	0.26353	-0.4276	0.219316	0.610179	0.065139	0.173461	0.37351	-0.16568	0.703304	**0.59226**	-0.19568	-0.21057	-0.07507	0.008576	1									
Mo	**0.663058**	**0.630362**	0.126474	-0.23643	-0.72507	-0.72401	0.431656	-0.39364	-0.13552	-0.43769	**0.785225**	-0.37746	0.066689	-0.43335	-0.20587	1								
Cu	0.116369	-0.03502	0.213113	0.308747	-0.24726	-0.15857	0.327551	-0.10565	0.222984	0.098742	**0.543446**	-0.11873	0.480261	0.107552	-0.1595	0.268923	1							
Pb	0.343784	0.055644	0.12419	0.182271	-0.24523	-0.18743	0.123648	-0.11208	0.047232	-0.0623	0.052795	-0.10227	0.313798	-0.18565	-0.03131	0.164263	**0.621881**	1						
Zn	-0.23217	-0.5542	-0.41594	0.448474	**0.74977**	**0.758448**	-0.48232	0.00121	0.094501	**0.611279**	-0.39868	-0.00287	0.328339	0.072181	0.13103	-0.5828	-0.23536	-0.1562	1					
Ni	**0.735597**	0.424457	-0.01347	0.115899	-0.51434	-0.49127	0.298894	-0.38606	-0.01226	-0.20182	**0.673082**	-0.37522	0.422008	-0.47833	-0.0059	**0.879967**	0.341108	0.341848	-0.34049	1				
As	0.214616	0.018302	0.264453	0.296282	-0.34187	-0.24295	0.319076	-0.0136	0.212238	0.052458	0.281718	-0.02151	0.350636	-0.07131	-0.00767	0.219385	**0.838505**	**0.875589**	-0.29845	0.350358	1			
Sb	-0.22175	-0.17611	-0.01457	0.250136	0.114219	0.167212	0.004505	0.20742	0.28754	0.280748	0.439021	0.178699	0.435608	0.154851	-0.04794	-0.10057	**0.508762**	-0.12187	0.21341	-0.03764	0.166254	1		
Ag	**0.965562**	0.041278	0.463885	0.272981	-0.46822	-0.41889	**0.628541**	-0.23655	0.455582	-0.11859	0.382151	-0.25793	0.185501	-0.14242	0.314837	**0.622712**	0.300595	**0.506894**	-0.236	**0.743146**	0.411098	-0.17733	1	
Hg	-0.31136	-0.17009	-0.03294	0.103816	0.170988	0.196525	-0.08608	0.305447	0.277246	0.175474	0.134768	0.274845	0.185272	0.130883	0.21855	-0.32119	0.143011	-0.27059	0.096964	-0.26291	-0.07488	**0.80695**	-0.31636	1

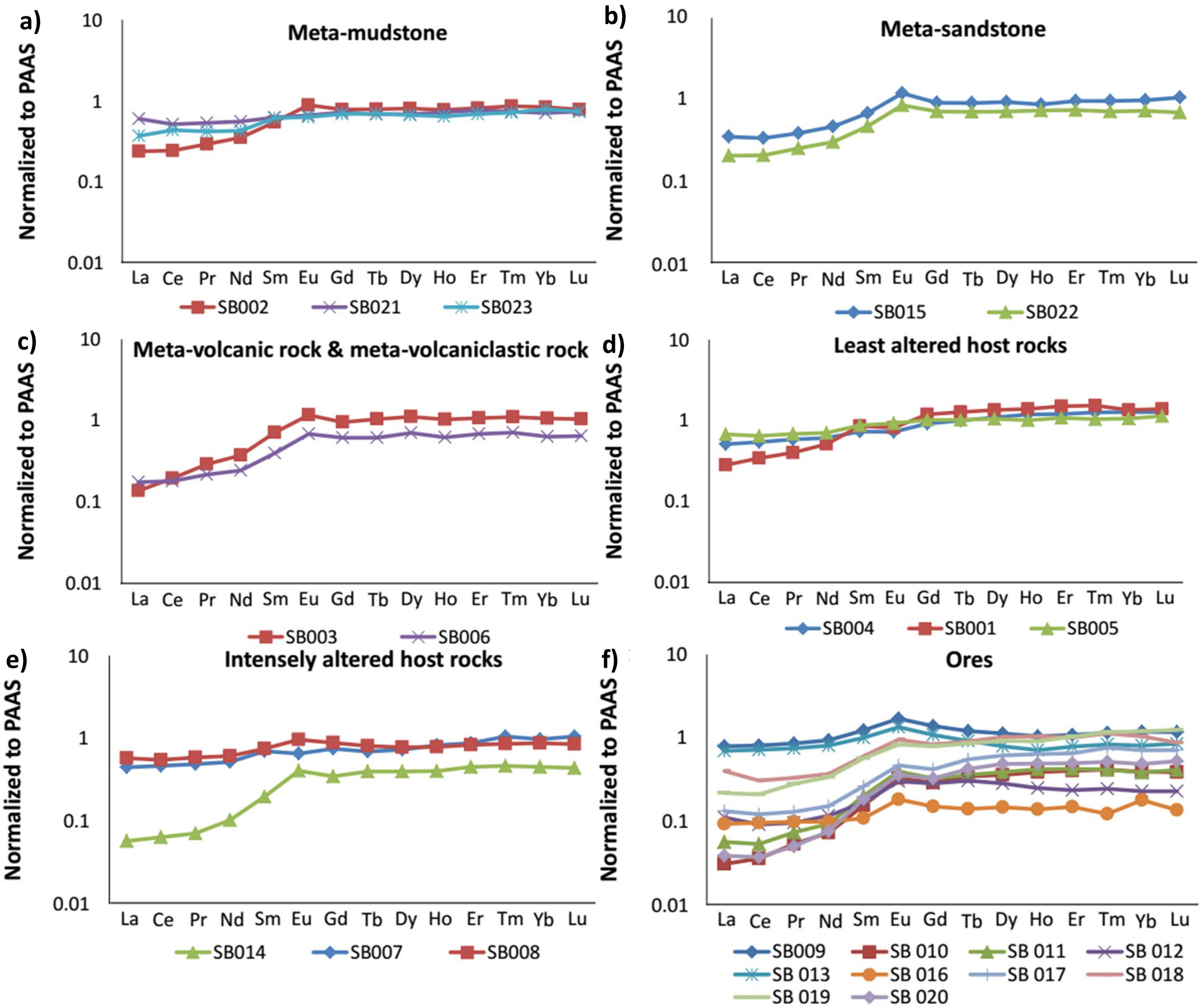

Figure 38. a-f) PAAS normalized REE plots of unaltered altered host rocks and ores in the Salu Bulo prospect.

7.3 Correlation coefficients (R)

Correlation coefficients (r) for selected elements were calculated and summarized in Table 5. Correlation coefficients (r) of whole-rock Ag, Ni, Mo and Na contents to whole-rock Au content are above 0.5 (Fig. 39) indicating that those are strongly correlated to whole-rock Au content. Correlation coefficients (r) of Al, Ti, Cr, Pb and W contents to whole-rock Au content are between 0.5 and 0.25 indicating that those are weakly correlated to whole-rock Au content (Fig. 39). On the other hand, correlation coefficient (r) of whole-rock Mg, Ca, K, Mn, Ba, V, Zn, Sb and Hg to whole-rock Au are negative (Fig. 39).

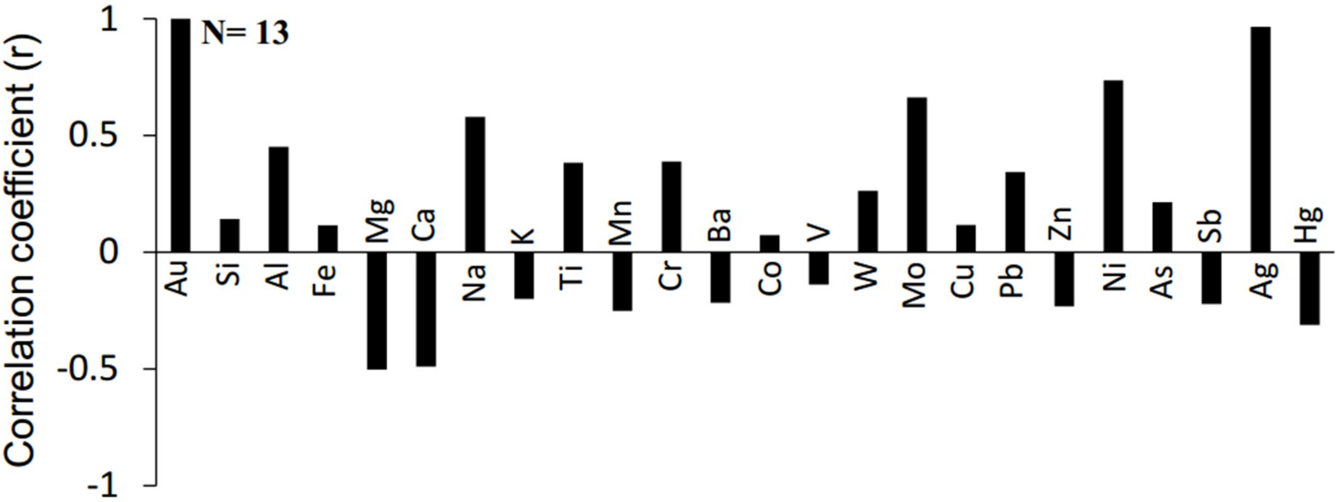

Figure 39. The correlation coefficient (r) between Au and selected elements in intensely altered host rocks and ores.

Correlation between Au and Na indicates albitization is a good indicator of gold mineralization in the Salu Bulo prospect. Similarly, Ni and Mo also can indicate the source of fluid to form gold mineralization in the Salu Bulo prospect which show strongly correlated to Au. K is not correlated to Na in the intensely altered host rocks and ores (Fig. 39). In addition, bivariate diagrams between Au and other elements of whole-rock composition of intensely altered host rocks and ores show Au is not correlated with Zn, Sb, Cu, As, W and Pb and only positively correlated with Ni and Mo (Figs. 40a-h). Silver is strongly positively correlated to Au (Fig. 40i).

7.4 Mass balance/transfer

7.4.1 Major Elements

Major oxide elements in unaltered and altered host rocks with or without ore are shown in Figure 42. CaO content of meta-(chloritic) mudstone, MgO and MnO contents are slightly elevated in the intensely altered host rocks and ore (breccia) than in the unaltered host rock, whereas Al_2O_3 and K_2O contents are depleted (Fig. 41a). Na_2O content of meta-

(graphitic) mudstone is elevated in the intensely altered host rock and ores than in the unaltered host rocks, whereas Al_2O_3, MgO, MnO and K_2O contents are depleted (Fig. 41b). Na_2O content is elevated and MgO content is slightly elevated in the altered host rocks than on the unaltered meta-(hematitic) mudstone, whereas CaO, K_2O and MnO contents are depleted (Fig. 41c). Na_2O and Al_2O_3 contents of meta-sandstone are similar in the unaltered and altered host rocks, whereas MgO, CaO, K_2O and MnO contents are depleted in altered part (Fig. 41d).

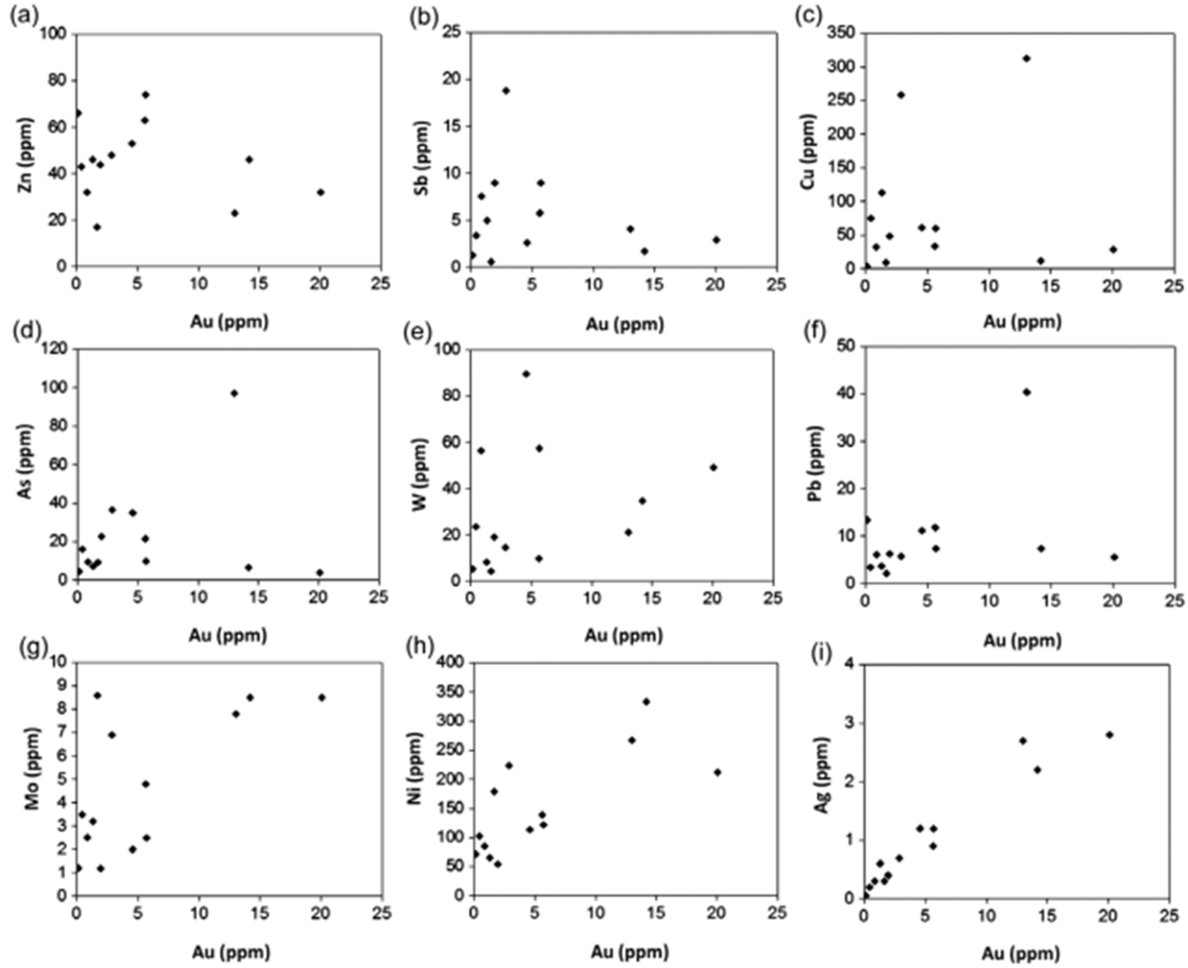

Figure 40. a-i) Correlation between Au and other elements. The samples were from intensely altered host rocks and ores.

Major oxide (i.e., CaO, MgO, Fe_2O_3, Al_2O_3 and MnO) contents in hydrothermally altered host rocks and ores depend on an inherited bulk composition of host rocks (i.e. mineral composition). The K_2O contents of unaltered and least altered host rocks are generally higher than those of intensely altered host rocks and ores indicating water-rock interaction during hydrothermal activity decomposed K-bearing minerals such as illite or muscovite in the unaltered host rocks (Fig. 41).

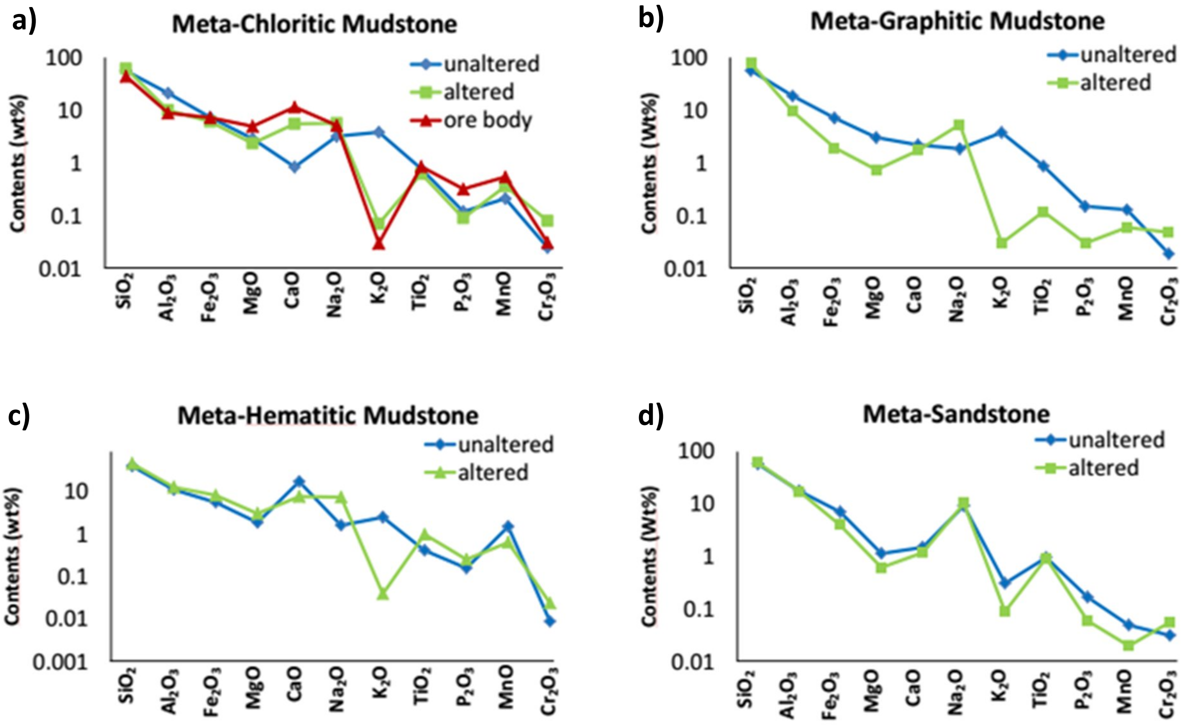

Figure 41. a-d) Whole rock major elements oxide of unaltered and altered host rocks of various meta-sedimentary rocks in the Salu Bulo prospect.

Na and K contents of unaltered host rocks and hydrothermally altered host rock and ores are inversely relationships reflecting differing proportions of albite and K-bearing minerals (e.g., illite or muscovite) (Fig. 42a). Fe/(Fe+Mg) molar ratio of hydrothermally altered host rocks and ores are not significantly enriched in unaltered host rocks while pyrite is present in the altered host rocks (Table 4, Fig. 42b). Slightly high sulfur contents of the unaltered host rocks is related to fine- and medium-grained pyrite that were formed during syn-sedimentary and diagenetic process. Figure 42c shows relatively positive correlation between MgO and LOI in intensely altered host rocks and ores than in the unaltered host rocks which indicates water-rock interaction and presence of ankerite alteration by addition of CO_2. Total volatile content (LOI) in the intensely altered host rocks and ores is elevated than in the unaltered host rocks (Table 4, Figs. 42c, d). Similarly, total C content is elevated in the intensely altered host rocks and ores, apart from a sample of meta-(graphitic) mudstone

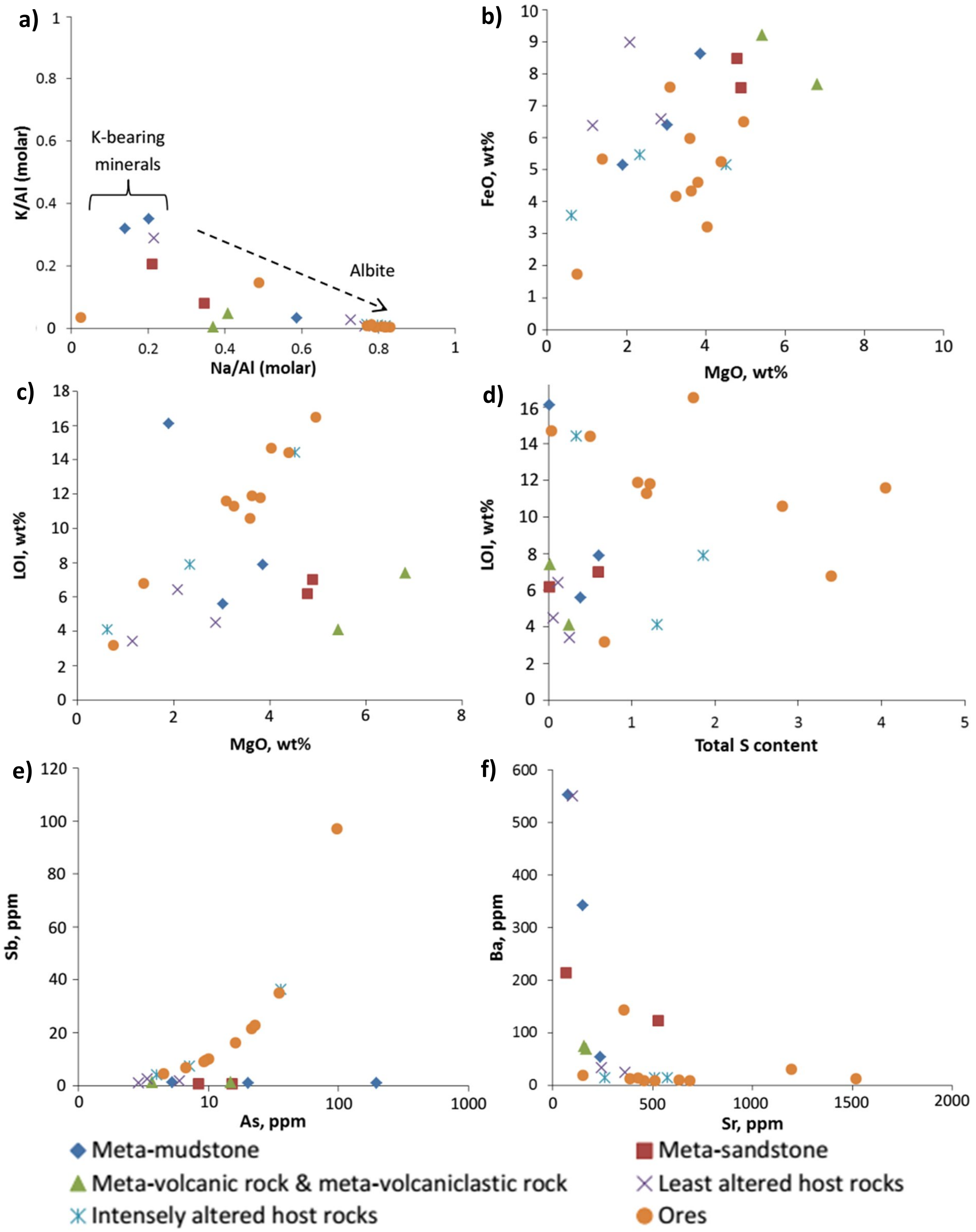

Figure 42. Plot of a) molar ratio Na/Al and K/Al; b) iron and magnesium oxide contents; c) magnesium oxide content and loss-on-ignition; d) total sulfur contents and loss-on-ignition (LOI); e) Sb and As contents; and f) Ba and Sr contents in unaltered and altered host rocks and ores in the Salu Bulo prospect.

in unaltered host rocks (Table 4). During the hydrothermal activity, the addition of CO_2 and S contributed for ankerite alteration and pyrite formation, respectively in the intensely altered host rocks and ores.

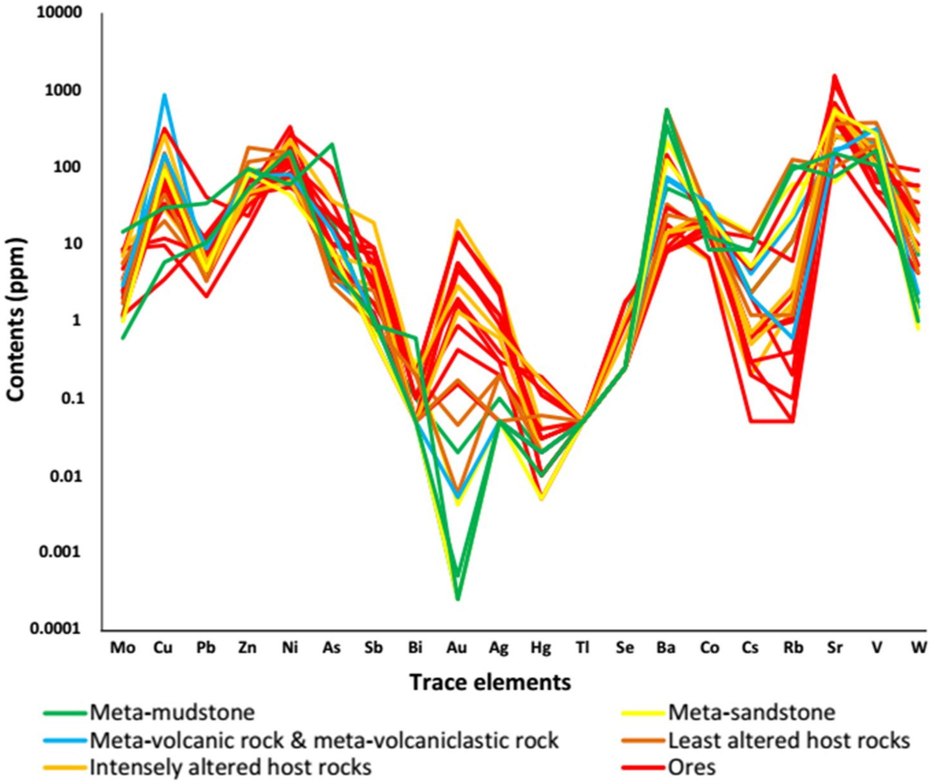

Figure 43. Diagram of trace element concentrations in unaltered and altered host rocks and ores in the Salu Bulo prospect.

7.4.2 Trace Elements

Trace element concentrations in intensely altered host rocks and ore are slightly and strongly elevated or depleted relative to unaltered host rocks during hydrothermal alteration (Table 4, Fig. 43). Mo, Ni, Sb, Hg, Se, Sr and W contents were significantly increased in altered host rocks and ores relative to unaltered host rocks, whereas Cs, Rb, Ba and V contents were decreasing (Fig. 43). Concentration of Ni is constant in unaltered host rocks, altered host rocks and ores indicating that it was locally derived from host rocks during water-rock interaction (Fig. 44). On the other hand, strongly positive correlation between Au and Ni indicate that significant amount of Ni in the ore-forming fluid was probably derived from the interaction between the hydrothermal fluid and mafic rocks prior to form gold mineralization in the Salu Bulo prospect (Fig. 39).

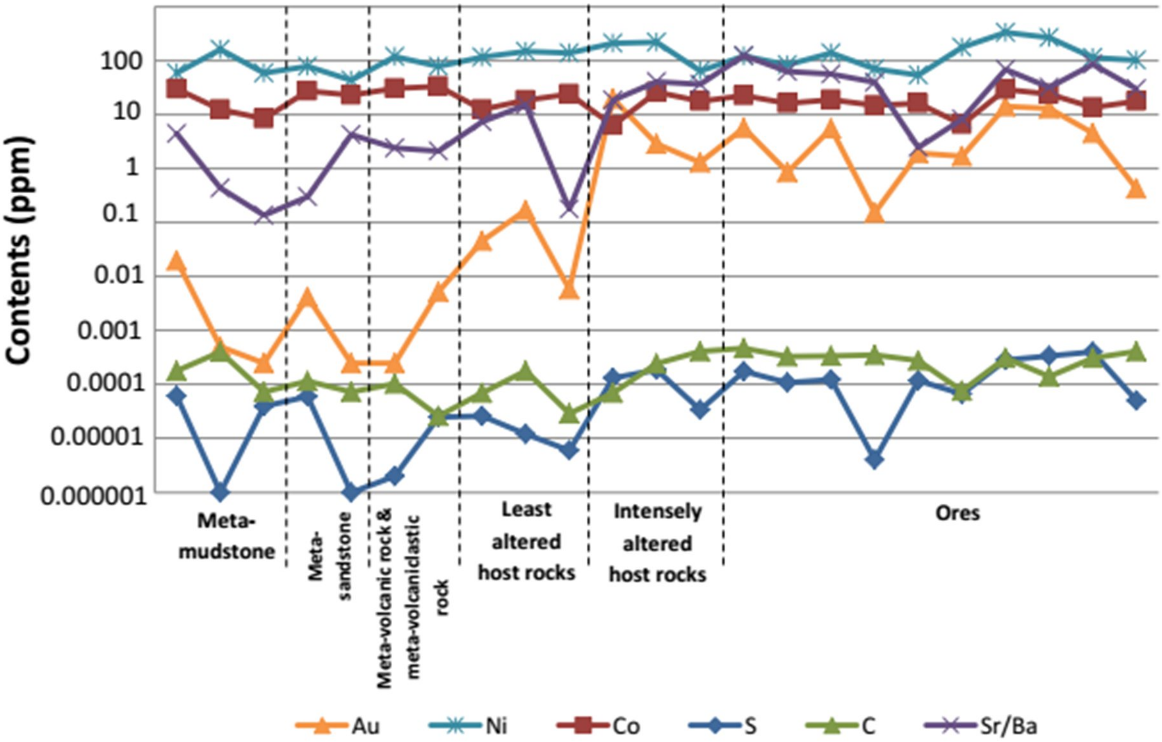

Figure 44. Diagram of Ni, Co, total sulfur and carbon, Sr/Ba ratio, and gold in unaltered and altered host rocks and ores in the Salu Bulo prospect.

Sb concentration is mainly depleted in unaltered host rocks and increased in altered host rocks and ores along with As concentration which shows linear correlation (Table 4, Figs. 42e, 43). However, As concentration in unaltered host rocks is relatively high and does not show significantly increased in altered host rocks and ores (Table 4, Figs. 42e, 43). Ba concentration in unaltered host rocks is elevated compared with that in the altered host rocks and ores (Table 4, Figs. 42f, 43). Inversely, Sr concentration is elevated in altered host rocks and ores compared to that in the unaltered host rocks (Table 4, Figs. 42f, 43). Sr/Ba ratio of altered host rocks and ores ranges from > 5 to 126.5 apart of sample numbers SB005 and SB013 compared to unaltered host rocks which are less than 5, reflecting highly elevated Sr concentration during hydrothermal activity (Table 4, Figs. 42f, 44).

7.4.3 Rare earth elements (REE)

Meta-sandstone and sample number SB003 show positive Eu anomalies reflect plagioclase content (Figs.38b, c). Similarly, intensely altered host rocks and ores show positive Eu anomalies (Figs. 38e, f, 45). REE patterns of the intensely altered host rocks and ores are relatively similar compared to unaltered host rocks (Figs. 38, 45). However, total REE are depleted in intensely altered host rocks and ores which are evidence for mobility and fractionation of REE during hydrothermal alteration through water-rock interaction (Fig. 45).

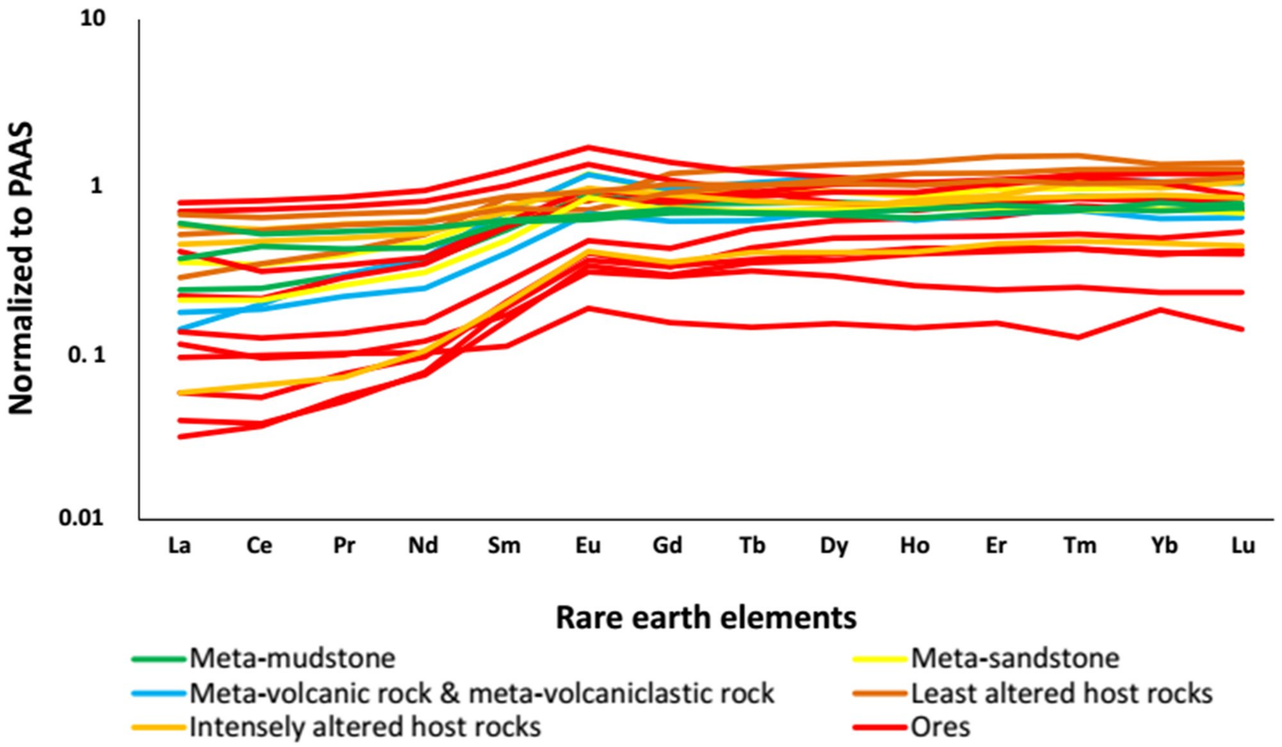

Figure 45. PAAS normalized REE plots of unaltered altered host rocks and ores in the Salu Bulo prospect showing evidence for mobility and fractionation of REE during hydrothermal activity.

7.5 Pyrite chemistry

7.5.1 Morphology and texture

Pyrite is a major sulfide mineral in the Salu Bulo prospect. As explained in the previous chapter, it shows various morphologies and textures such as porous, deformed and massive aggregates (Table 6, Figs. 46-49). On the basis of petrographic observations, pyrite is divided into five types according to morphological, characteristics and overgrowth relationship (Table 6, Figs. 46-49).

Pyrite 1: fine-grained framboidal pyrite

Pyrite 1 (py1) mainly occurs in unaltered host rocks and often aligned parallel to foliation plane. It consists of individual fine-grained (< 2 μm) to cluster framboidal (5 μm to 1 mm across) pyrite grains (Table 6, Fig. 46). Py1 grains are associated with py2 (Figs. 46c, d), py3 and py5 (Figs. 49a, b) and are considered to be the oldest pyrite type. Framboidal pyrite is generally thought to be syn-sedimentary or early diagenetic in origin (Liu et al., 2006). Py1 also occurs in altered host rocks and clast of breccia as inherited from unaltered

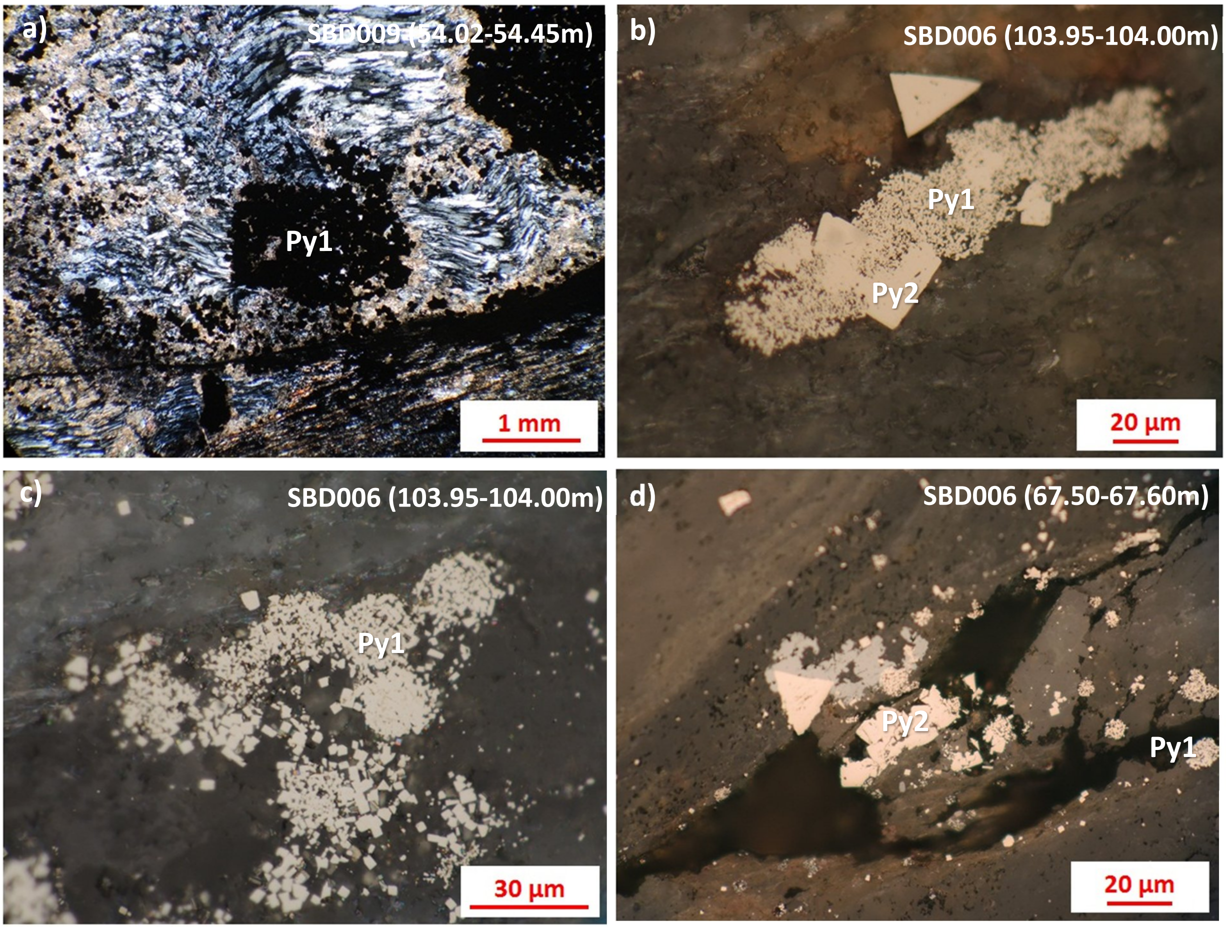

Figure 46. Photomicrograph of py1 and py2 in phyllite that related to quartz fringe of the early quartz-ankerite vein (a), unaltered meta-(chloritic) mudstone (b-c) and slightly silicified meta-(graphitic) mudstone (d).

Pyrite 2: medium-grained pyrite

Pyrite 2 (py2) occurs as clusters of relatively coarser euhedral-subhedral grains than py1 that commonly surround and overgrow py1 and as individual grain (Table 6, Figs. 46c,

Table 6. Summary of pyrite morphologies and textures and interpretation of formation process of five types of pyrite in the Salu Bulo prospect.

Classification	Fine-grained	Medium-grained	Porous	Deformed	Massive
Size	< 2 µm	5 - 30µm	0.01 – 2.3 mm	0.04 - 0.95 mm	0.01 - 2.25 mm
Shape	Euhedral-subhedral; layered; framboidal	Euhedral-subhedral;	Euhedral - subhedral; cubic (mostly);	Subhedral - anhedral	Euhedral
Internal texture and characteristics	Commonly clear, inclusion free	Commonly clear, inclusion free	Irregular dissolution core filled by silicate and carbonate minerals and sedimentary matrix; random and preferential alignment inclusion; gold and other sulfide minerals as fracture filling and inclusion, respectively	Deformation of early (porous) pyrite; gold and other sulfide minerals as fracture filling and inclusion, respectively	Less porous; visible sulfide minerals as inclusion
Hosted by	Host rocks (Intensely foliated graphitic phyllite); altered host rocks; clast of breccia	Host rocks; altered host rocks; clast of breccia	Ore bodies; altered host rock	Ore bodies; altered host rocks	Ore bodies; altered host rock; clast of breccia
Interpretation of formation process	Syn-sedimentary to syn-diagenetic	Diagenetic?	Late diagenetic to syn-metamorphism?	Syn-deformation	Late deformation to hydrothermal event
Other features	Overgrown by later pyrite; deformed; layering and framboidal; early recrystallization	Recrystallization of fine-grained pyrite; overgrew early pyrite	Recrystallization of fine-grained pyrite; preferential alignment of inclusion parallel to foliation; framboidal pyrite as core; boudinage	Brecciated; fractured; rotated	Fractured; overgrew fine-grained pyrite

d). Its size ranges from 5 to 30 µm across (Table 6). It was formed later than py1 during the diagenetic process by increasing temperature (Figs. 46b, d). Py2 is mainly present in unaltered host rocks and often in altered host rocks and ores.

Pyrite 3: porous pyrite

Pyrite 3 (py3) is coarser grained than py1 and py2. It occurs as euhedral-subhedral grains and is commonly present in host rocks and ores with grain size vary from 0.01 to 2.3 mm across (Table 6, Fig. 47). The core of py3 is often aligned or oriented parallel to foliation and commonly in the highly foliated or metamorphic host rocks. Spatially, gold occurred as a filling of porous.

Figure 47. Photomicrograph of py3 showing core (porous) and rim hosted in carbonate alteration of meta-(graphitic) mudstone (a, b) and in silicified meta-mudstone (c).

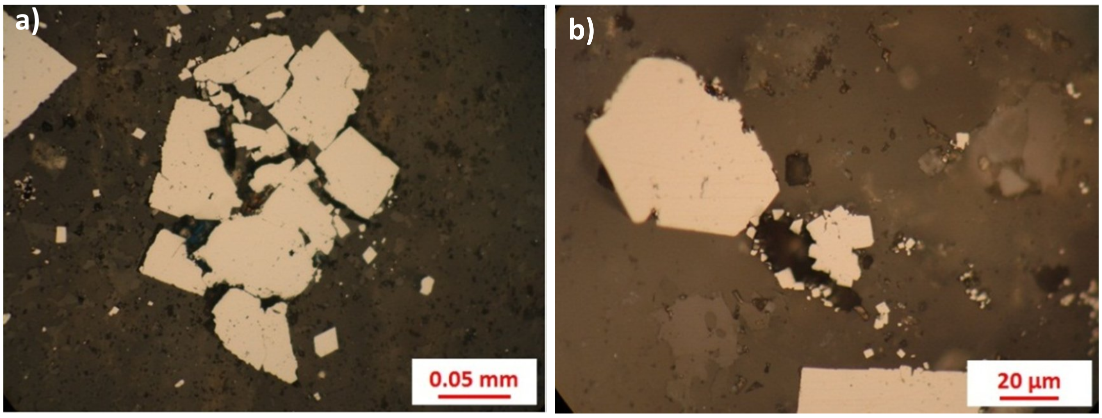

Figure 48. a-b) Photomicrograph of py4 in breccia ore of SBD069 (52.06-52.10 m).

Pyrite 4: deformed pyrite

Pyrite 4 (py4) is deformed pyrite showing brittle and ductile signatures and subhedral-anhedral shape (Table 6, Fig. 48). Its size is around 0.04 to 0.95 mm. It is common in ores. Py4 has a strongly spatial relationship with gold that occurred as filling in the fractures. Py4 locally exhibits intense fracturing and pulverizing particularly in breccia. It was probably occurred within brittle deformation that accompanied by hydrothermal activity.

Pyrite 5: less porous (massive) pyrite

Py5 is assumed latest pyrite that was formed during hydrothermal activity. It is common in altered host rocks and ores showing less porous and euhedral to subhedral shape (Table 6, Fig. 49). Its size is around 0.01 to 2.25 mm. It is occasionally overgrowing py1 (Figs. 49a, b).

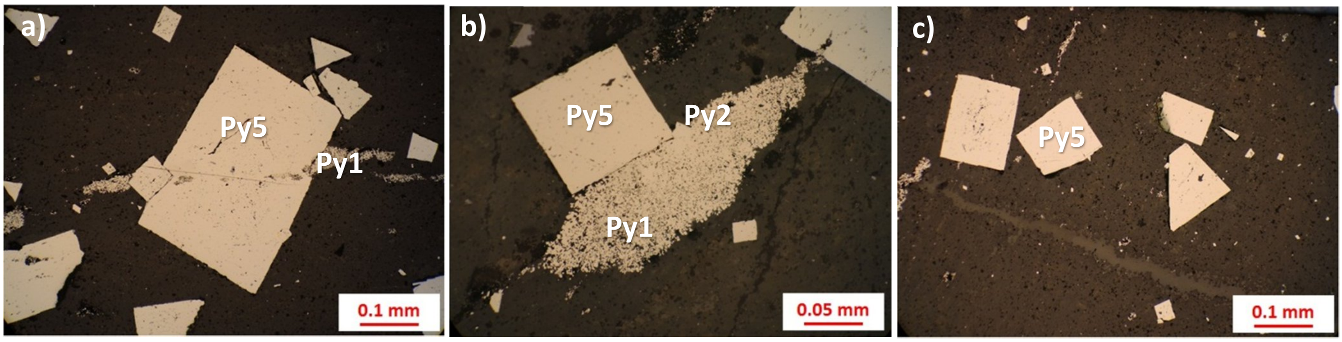

Figure 49. a-c) Photomicrograph of py1, py2 and py5 in breccia ore of SBD069 (52.06-52.10 m).

No significant elevated total sulfur in the intensely altered host rocks and ores indicates that some pyrite were formed prior the mineralization within syn-sedimentary, or syn-diagenetic process and probably syn-metamorphism period to form Py1, Py2 and Py3.

7.5.2 Trace elements

Electron probe micro analyzer (EPMA) was used to determine the concentration of trace elements (As, Co, Cu, Ni, Zn, W and Au) and to investigate chemical zoning of five types of pyrite (Appendix 4, 5). Au concentration up to 20 - 320 ppm was rarely observed. Ni and Co concentrations are high, 10 - 7780 ppm and 390 - 2710 ppm, respectively, in edges, cores and rims of py2, py3 and py5 with zoning (Figs. 50-55, Appendix 5). As concentrations are relatively low or absent in all type of pyrite confirming As-poor pyrite in the Salu Bulo prospect, similarly for Zn and W concentrations that are not significantly high (Fig. 53,

Appendix 5). Cu concentrations are highly similar to Ni and Co that range from up to 20 to 1280 ppm (Fig. 51).

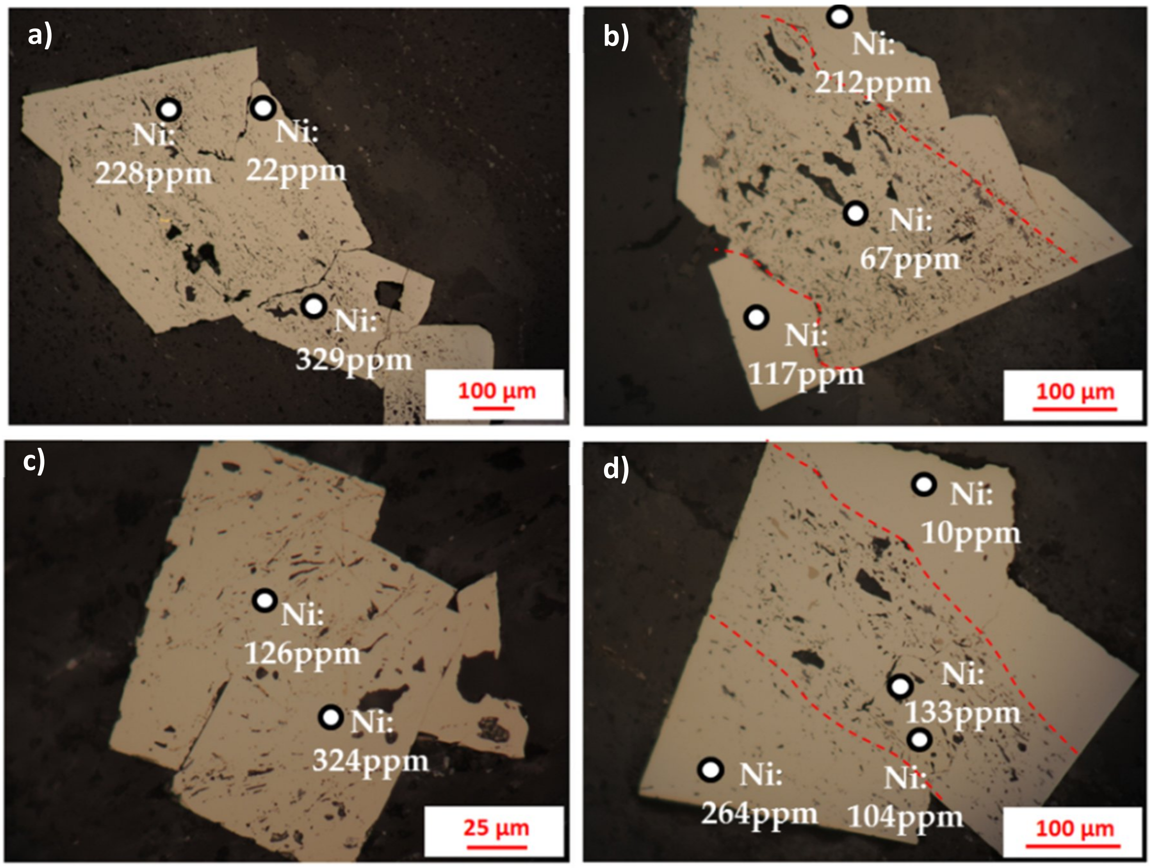

Figure 50. Point observation of Ni in different pyrites morphologies hosted in carbonate alteration of meta-(graphitic) mudstone in SBD053 (104.75-104.80 m) (a, b, d) and silicified meta-(graphitic) mudstone in SBD006 (66.75-66.85 m).

High concentrations of Ni in the pyrite are consistent with high Ni content in unaltered and altered host rocks and ores. On the other hand, Co concentration in unaltered and altered host rocks and ores are not significantly high. Co/Ni ratio of all pyrite ranges from 0.09 to 63 with wide range Ni and narrow range Co contents (Fig. 52). Zaccarini and Garuti (2008) reported that high Co/Ni ratio of pyrite in the VMS deposit of northern Apennine ophiolites, Italy in which Ni was leached from mafic host rocks due to water-rock interaction between the hydrothermal fluid and the host rocks at the site of ore deposition. Ni can substitute element in silicate lattice of chlorite along with Fe, Mg and Mn. In the Salu Bulo prospect, Chlorite was mainly occurred in unaltered host rock and absent in altered host rocks and ores (Fig. 19). This condition assumes chlorite could become the source of Ni in the ore-forming fluid that leached during water-rock interaction.

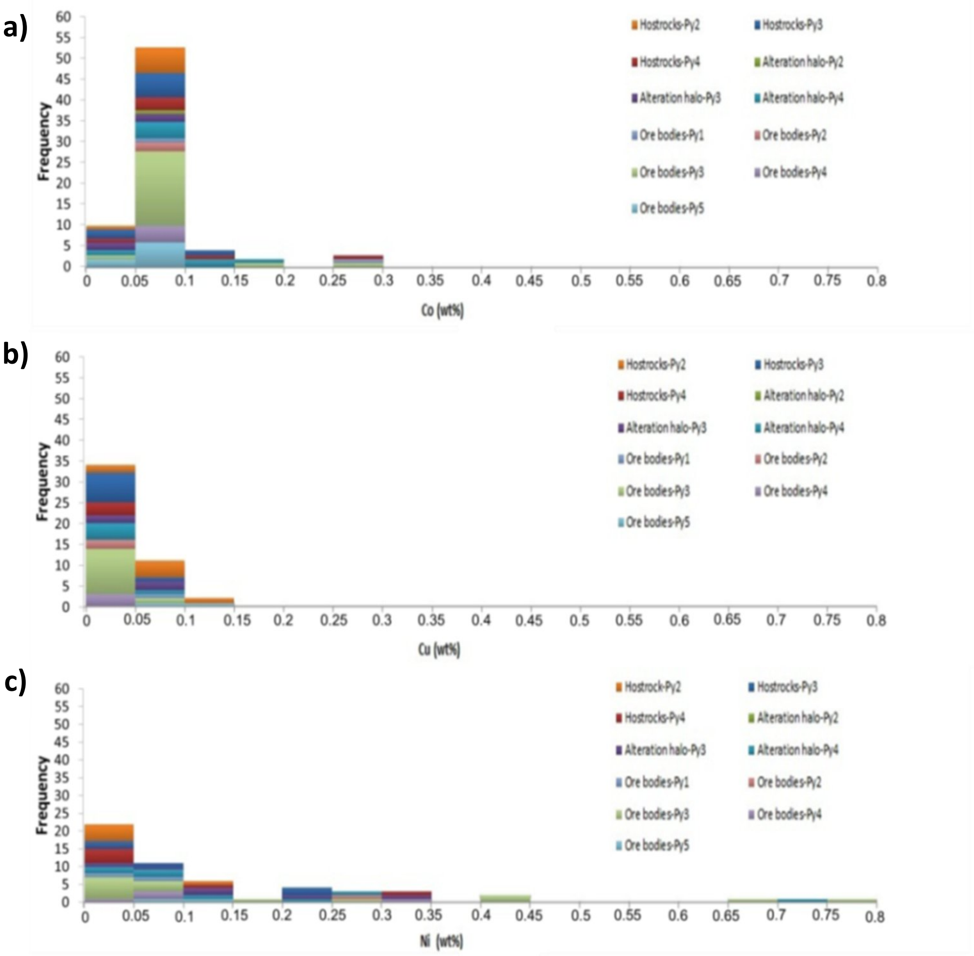

Figure 51. Composition of Co (a), Cu (b) and Ni (c) in pyrite from the Salu Bulo prospect.

7.5.3 Element mapping

Elemental mapping of five types of pyrite in the Salu Bulo prospect indicates that high concentration of Ni and Co show zoning compared to other elements (Figs. 53, 55). Py1 is low in S concentration indicating genetically formed during sedimentary and diagenetic process, while high in Co content (Figs. 53a, 55). Py2 contains high Ni concentration and moderate Co concentration (Figs. 53a, 55). Py3 is high in Ni and Co concentrations, concentrated in the core of pyrite than in the rim which they show normal zoning and was deformed in some observations probably during diagenesis or metamorphism (Figs. 53b, 54, 55). Py5 is high in Ni concentration and low in Co concentration (Figs. 53a, 53c, 55).

Evidence of overgrowth on early pyrite by later pyrite is shown in Figure 46b, d and 49a, b, py1 is overgrown by py2 and py5. However, zoning of Ni and Co reflects several periods of pyrite formation (Figs. 53, 55).

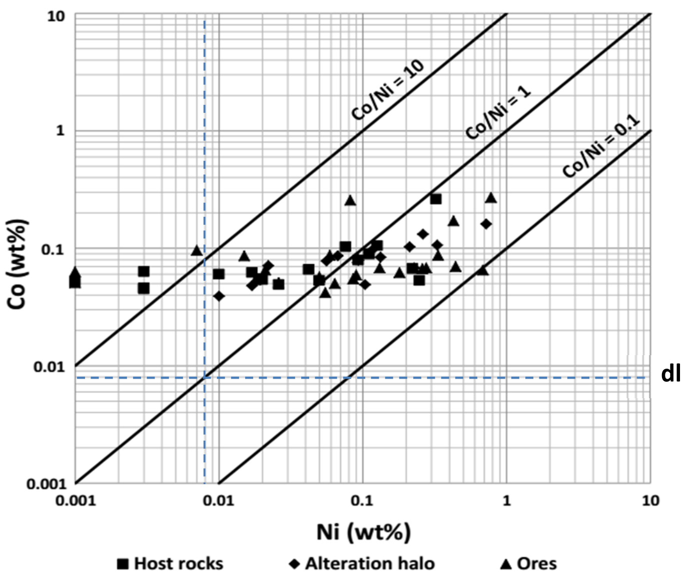

Figure 52. Plot of Co vs Ni contents (by EPMA) in pyrites from unaltered and altered host rocks and ores in the Salu Bulo prospect. (dl: detection limit).

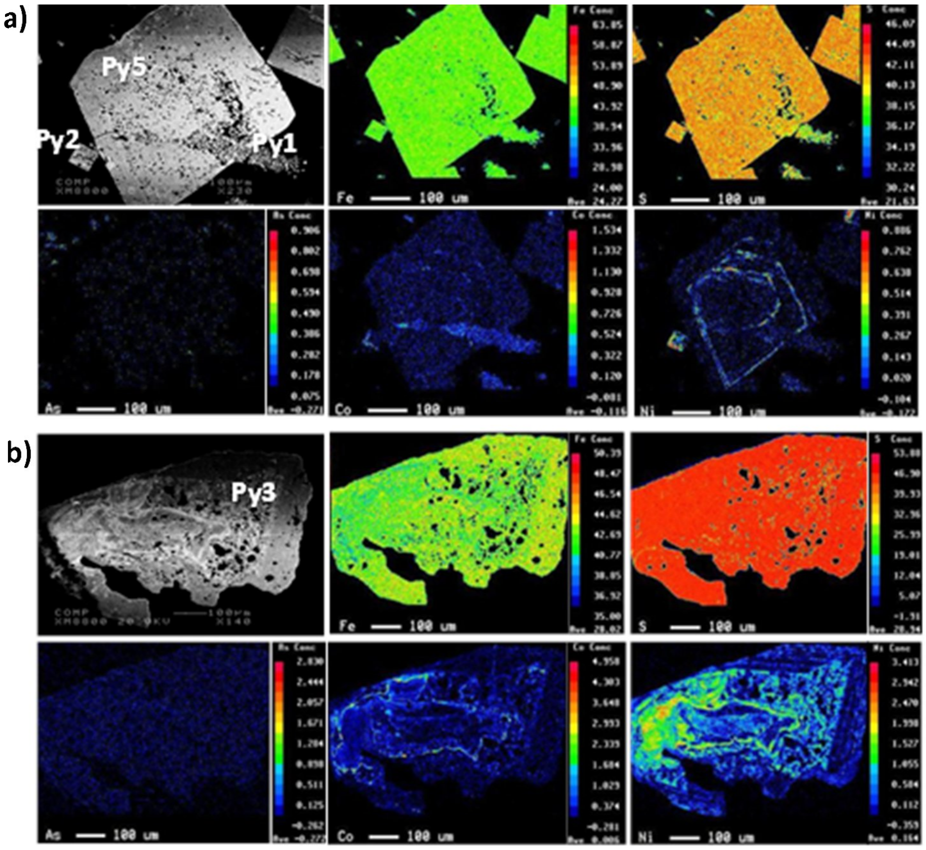

Figure 53. Element mapping (by EPMA) of pyrite in the Salu Bulo prospect. a) Py1, Py2 and Py 5 hosted in breccia ore that consists of quartz-ankerite±albite in SBD069 (54.65-54.85 m). c) Py3 hosted in silicified meta-mudstone in SBD109 (40.60-40.70 m).

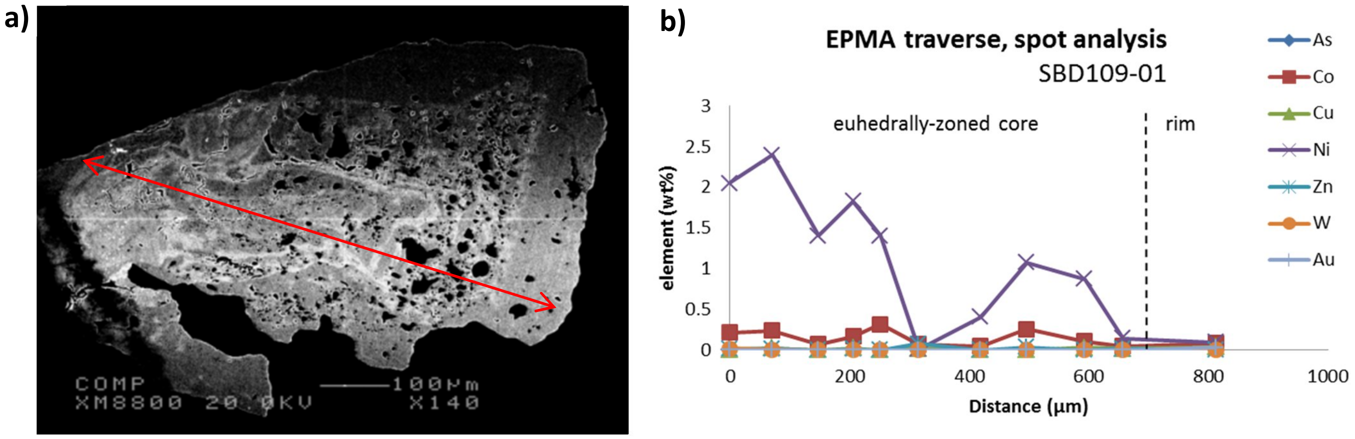

Figure 54. a) Backscatter image from electron microprobe analysis of py3 hosted in silicified meta-mudstone in SBD109 (40.60-40.70 m).; and b) trace elements distribution of pyrite along the rim to the core of py3 in Figure 54a.

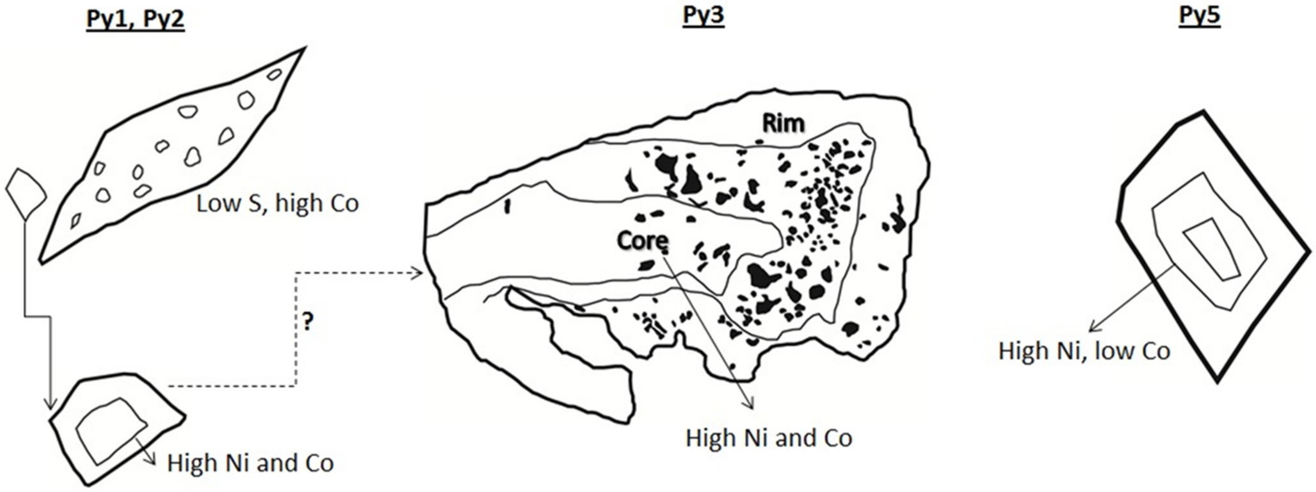

Figure 55. Schematic of morphologies and chemical composition of pyrite from Salu Bulo prospect.

7.6 Native gold and electrum chemistry

Gold is spatially related with pyrite as filling of pore and fracture or space between grains (Fig. 56). It is irregular and ellipsoid shape, size range from <2 to 42 µm. Table 7 shows atomic % Au in alteration halo and breccia that related to main stage veins (i?, ii, and iii). Gold occurs as electrum and native gold with Au/(Au+Ag) ratio ranging from 66.2 to 82.3 atomic % Au (Table 7, Fig. 57), while whole-rock Au/Ag ratio of strongly altered host rocks and ores ranges from 2.1 to 7.2 (average 4.6) (Table 4). However, the concentration of Au is not related to base metals based on assay data and electron microprobe analysis.

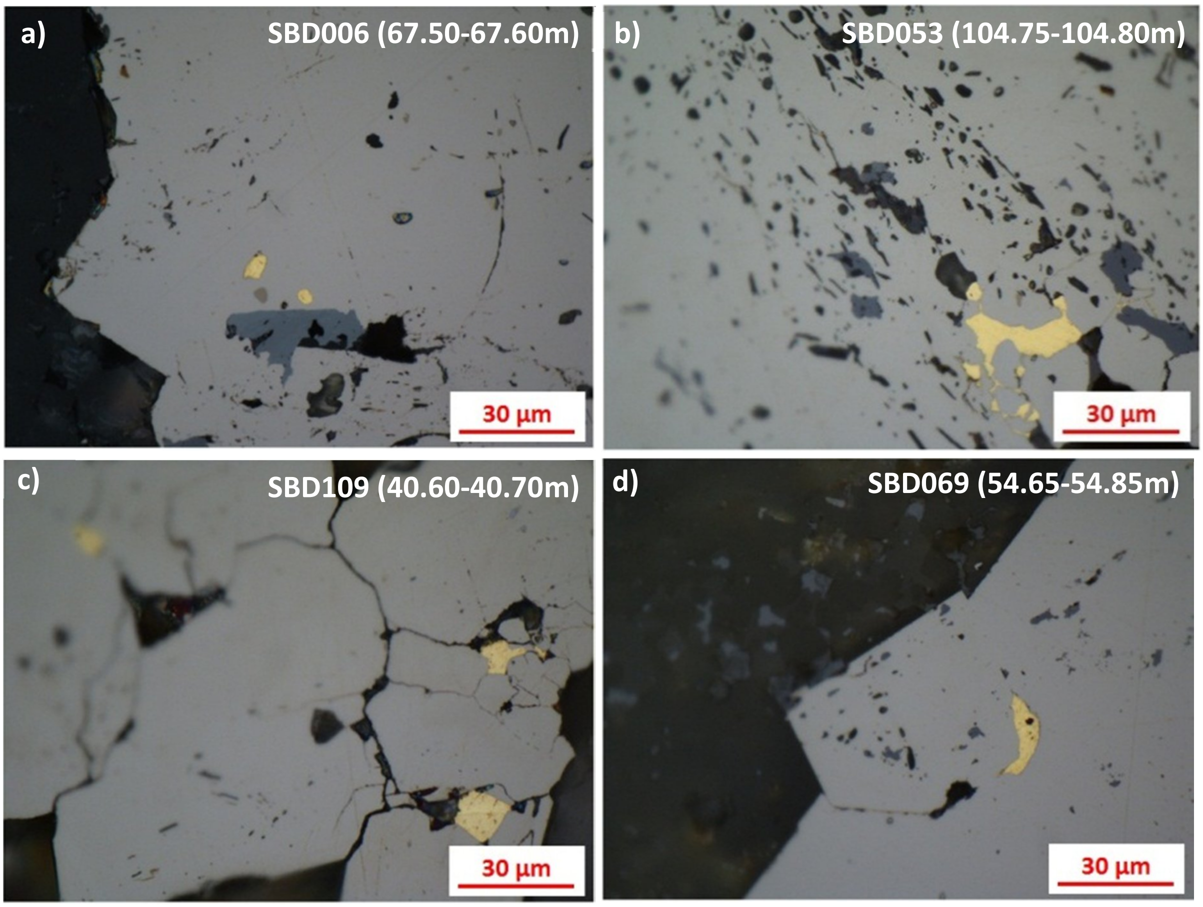

Figure 56. Photomicrographs of gold as filling porous and fracture of pyrites hosted in alteration halo of quartz±calcite-albite vein (iii) in meta-(graphitic) mudstone (a), alteration halo of ankerite±quartz±albite vein (ii) hosted in meta-(graphitic) mudstone (b), alteration halo of quartz±calcite-albite vein (iii) hosted in meta-(hematitic) mudstone (c), and breccia ore that consists of quartz-ankerite±albite.

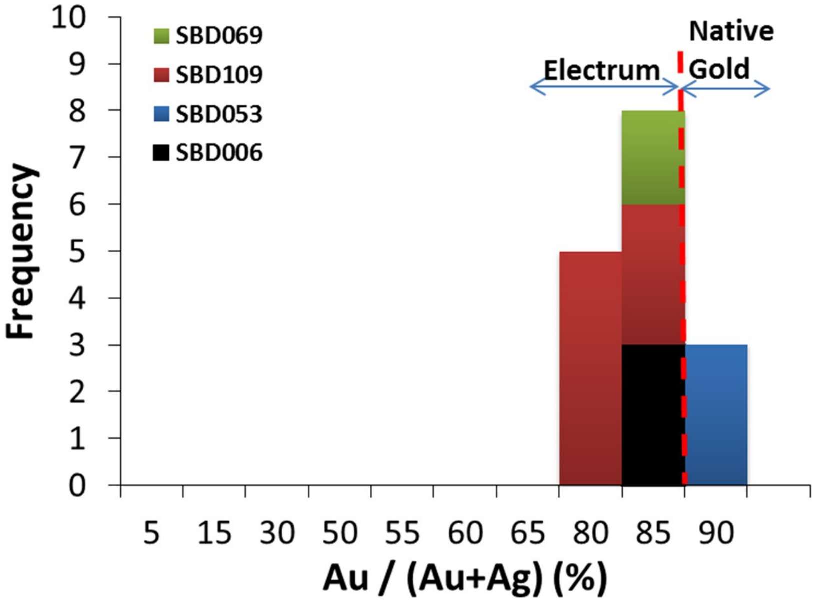

Figure 57. Au/(Au+Ag) atomic ratio of electrum and native gold in the Salu Bulo prospect.

Table 7. Atomic % of native gold and electrum from the Salu Bulo prospect, calculated by applying Bence and Albee method using K (%) of electrum microprobe data.

No.	Drill hole	Depth (m)	Host rock	Lithology	Main stage vein	Alteration mineral assemblages	Point observation	Atomic %		Total (%)
								Au	Ag	
1	SBD006	67.50-67.60	meta-graphitic mudstone (phyllite)	Alteration halo	iii	quartz±calcite-albite	1	79	22	100
							2	78	23	100
							3	77	23	100
2	SBD053	104.75-104.80	meta-graphitic mudstone (phyllite)	Alteration halo	ii	ankerite±quartz± albite	4	82	18	100
							5	81	19	100
							6	82	18	100
3	SBD109	40.60-40.70	meta-hematitic mudstone	Alteration halo	iii	quartz±calcite-albite	7	73	28	100
							8	68	33	100
							9	67	33	100
							10	70	30	100
							11	71	29	100
							12	68	32	100
							13	66	34	100
							14	69	31	100
4	SBD069	54.65-54.85	phyllite?	Breccia	i?	quartz-ankerite±albite	15	78	22	100
							16	78	22	100

CHAPTER VIII: FLUID INCLUSION AND STABLE ISOTOPE

8.1 Fluid inclusions

8.1.1 Sampling

Several samples of vein and matrix of breccia were prepared. Only five samples of the main stage veins and two samples of matrix of breccia were selected for analyses based on the occurrences of fluid inclusions, namely SB006-16, SBD072-13A and B, SB001-01 and 02, SB002-03 and SBD044-08 (Table 8, Fig. 58).

SBD006-16: The sample was taken from drill core SBD006 with depth ranges from 67.5 to 67.6 meters (Figs. 58a, b). The vein is classified as vein (iii) that was formed in the main stage during hydrothermal activity and cut by vein (iv). It consists of mainly quartz with lesser calcite and albite. The vein is sub-parallel to the foliation of host meta-(graphitic) mudstone (phyllite). Alteration halo along the vein shows intense silicification along with carbonatization. Pyrite is the main sulfide mineral that was formed in the alteration halo along with tetrahedrite. Gold was observed in the alteration halo as filling in deformed pyrite.

SBD072-13: It consists of two samples (A and B) which were taken from drill core SBD072 with depth ranges from 89.75 to 89.85 meters (Figs. 58c-e). The sample “A” is classified as vein (iii) that was cut by vein (iv) which is sample “B”. Both of the veins were formed in the main stage vein during hydrothermal activity. The sample “A” consists of mainly quartz with lesser calcite and albite whereas the sample “B” consists of quartz, ankerite and albite showing euhedral crystal that grew from the edge of vein. The vein (iii) is sub-parallel whereas vein (iv) cross cut to the foliation of host meta-(chloritic) mudstone. Alteration halo along the vein shows intense silicification along with

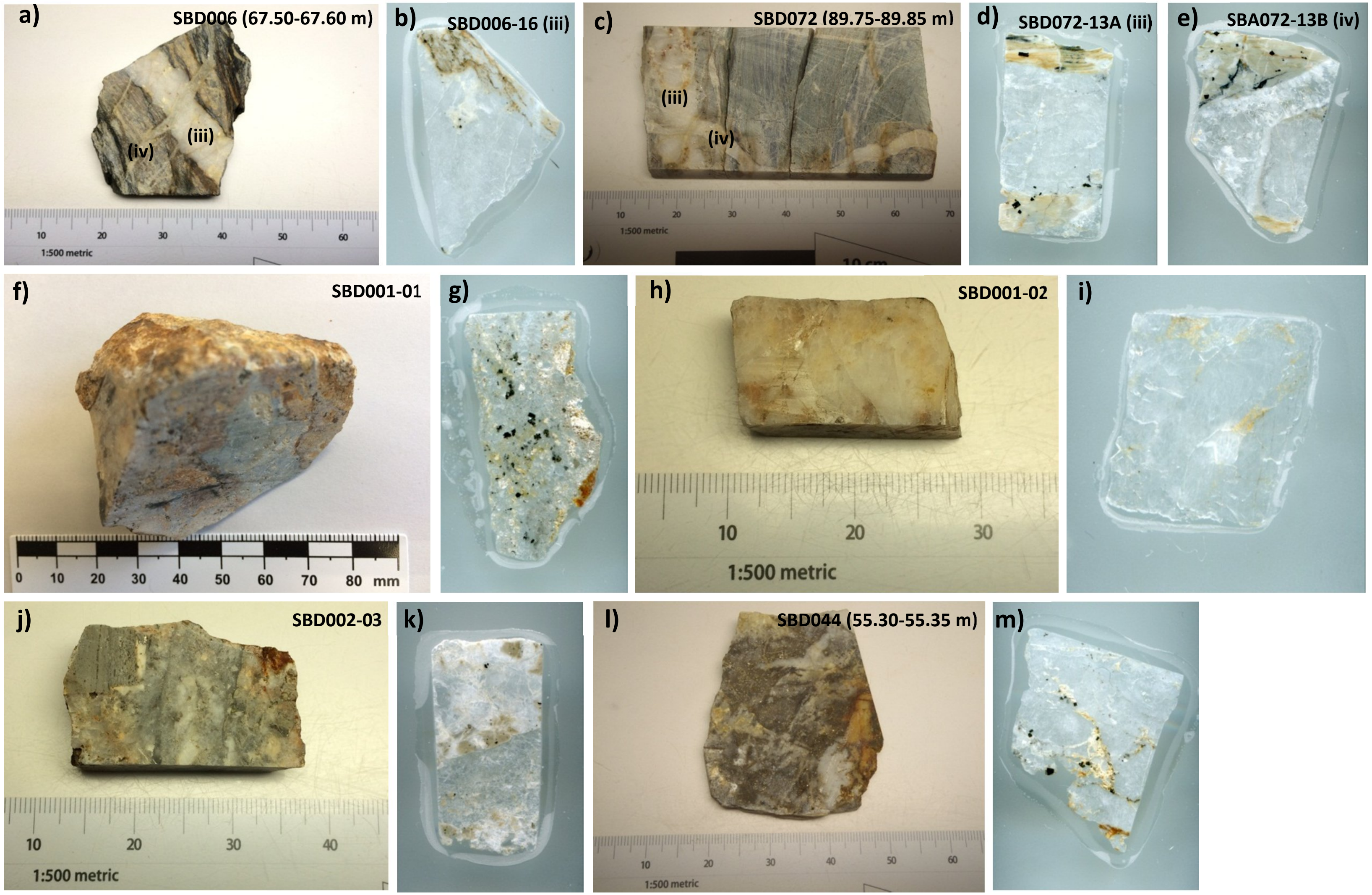

Figure 58. a-m) Representative photograph of fluid inclusion samples taken from main stage veins and breccia in the Salu Bulo prospect.

carbonatization. Pyrite is the main sulfide mineral that was formed in the alteration halo. Gold was observed along the alteration halo as filling in pyrite.

SB001: It consists of two samples (01 and 02) which were taken from the massive vein in outcrop SB001 (Figs. 33a, 58f-i). The sample A is classified as vein (iii) consisting of quartz. The sample B is classified as vein (iii) closest to the alteration halo. The vein is hosted by meta-(chloritic) mudstone. Alteration halo along the vein shows intense silicification along with albite. Pyrite is the main sulfide mineral that was formed in the alteration halo along with galena, chalcopyrite and tennantite. Gold was observed along the alteration halo as filling in deformed pyrite.

SB002-03: The sample is matrix of breccia which was taken from outcrop SB002 (Figs. 28d, 58j, k). The matrix of breccia consists of quartz, ankerite and albite showing euhedral crystal that grew from edge of breccia clast. It was formed in the main stage during hydrothermal activity and related to vein (iv). Silicification is intense in the altered clast of breccia. Pyrite is the main sulfide mineral that formed in clast and matrix of breccia.

SBD044-08: The sample is matrix of breccia which was taken from drill core of SBD044-08 with depth ranges from 89.75 to 89.85 meters (Figs. 58l, m). The matrix of breccia consists of quartz and carbonate (ankerite) that formed in the main stage during hydrothermal activity and related to vein (i). Silicified is intense in the altered clast of breccia along with carbonatization. Pyrite is the main sulfide mineral that formed in clast and matrix of breccia.

8.1.2 Petrography

Fluid inclusions of five samples of veins and two samples of matrix of breccia were observed under a Nikon polarization optical microscope. The distribution of the fluid inclusions is similar in the main stage veins and matrix of breccia. Isolated individual and clustered inclusions were considered as primary inclusions in quartz crystals. Fluid inclusions in quartz of vein and matrix of breccia are mainly two-phase liquid-rich inclusions with minor single-phase liquid and vapor inclusions and two-phase vapor-rich inclusions at room temperature (Fig. 59). The size of inclusions varies from 2 to 34 µm and shapes are negative crystal, irregular, spherical and elongated (Fig. 59).

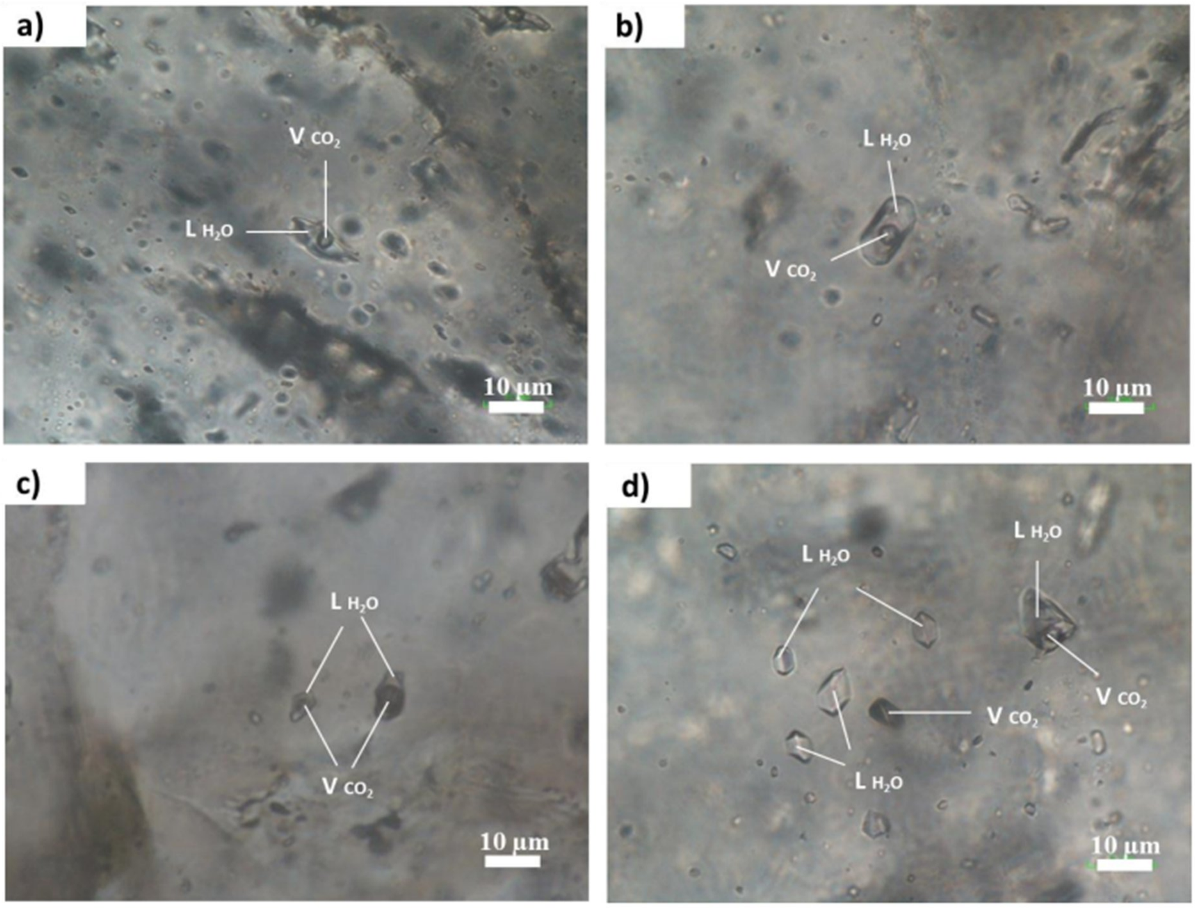

Figure 59. Photomicrographs of representative fluid inclusions in the Salu Bulo prospect. a and b) two-phase liquid-rich inclusion from ankerite±quartz±albite vein (ii) and matrix of breccia (SBD044-08), respectively ; c) the co-existence of two-phase liquid-rich and two-phase vapor-rich inclusions in matrix of breccia (SBD044-08); and d) single-phase liquid and vapor inclusions in matrix of breccia (SBD044-08).

8.1.3 Laser Raman microthermometry

Considering the size of fluid inclusions Laser Raman microthermometry was conducted only on single-phase vapor and liquid inclusions and two-phase liquid-rich inclusions in the main stage veins and matrix of breccia. It confirmed a composition of volatile CO_2 and N_2, occurring along with graphite (?) in single-phase vapor inclusion and

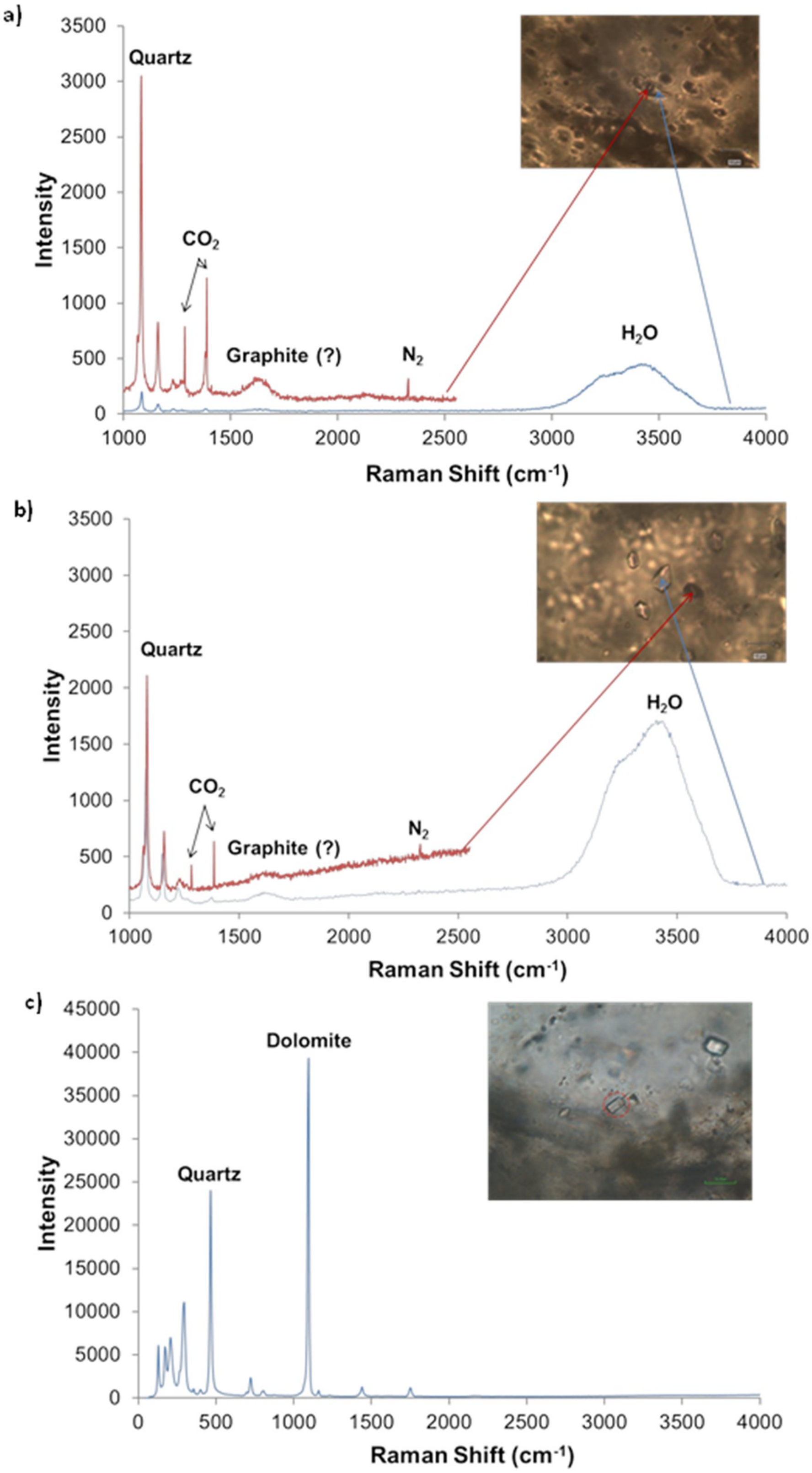

Figure 60. Laser Raman spectra of two-phase aqueous-carbonic inclusion in Figure 59a (a) and single-phase vapor inclusion and liquid inclusion in Figure 59d (b) containing CO_2 and N_2 gases and uncertain graphite in the vapor phase (red line) and H_2O liquid in the liquid phase (blue line). Dolomite as single mineral inclusion in the matrix of breccia (SB002-03) (c).

vapor phase of two-phase liquid-rich inclusions both in the veins and matrix of breccia (Figs. 60a, b). Raman spectrum of CO_2 clearly shows strong bands at ~ 1285 cm^{-1} (v_1) cm^{-1} and ~ 1388 cm^{-1} ($2v_2$) in the main stage vein and at ~ 1285 cm-1 (v1) cm−1 and ~ 1388 cm−1 (2v2) in the main stage veins (ii, iii, iv) and at ~ 1282 cm^{-1} (v_1) cm^{-1} and ~ 1385 cm^{-1} ($2v_2$) in the matrix of breccia, N_2 and graphite at ~ 2328 cm^{-1} and ~ 1617 cm^{-1} respectively in the main stage veins and at ~ 2327 cm^{-1} and ~ 1606 cm^{-1} respectively in matrix of breccia. Wide Raman spectrum of graphite indicates disordered mineral structure (Figs. 60a, b). Single mineral inclusion was also observed with a Raman shift at ~ 1096 cm^{-1} and it is identified as dolomite (Fig. 60c).

Using delta value of Fermi doublet of CO_2 which ranges from 102.77 to 102.84 cm^{-1}, CO_2 density was calculated using an equation from Yamamoto and Kagi (2006), ranging from 0.1 to 0.14 g/cm^3 thus low density CO_2 vapor (Fig. 61). Mole fraction of CO_2 and N_2 are determined from Raman spectra according to Burke (2001) with concentration of CO_2 ranging from 50 – 93.6 mol % and N_2 range from 6.4 – 50 mol %.

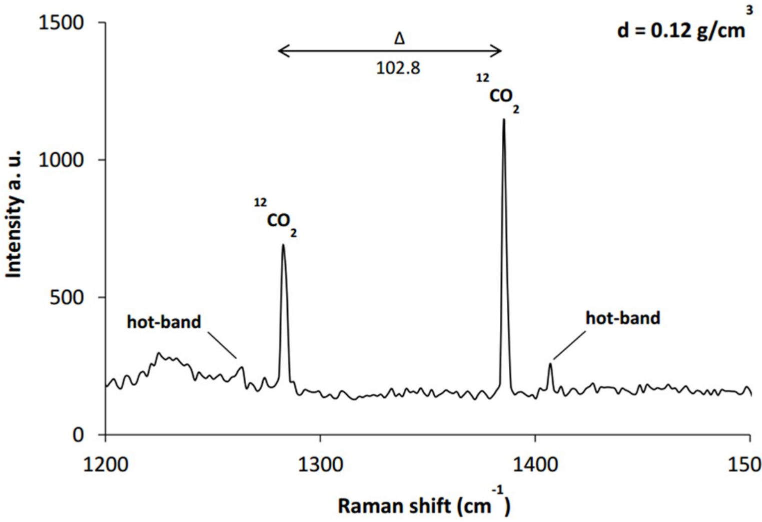

Figure 61. Laser Raman spectra used to estimate density of CO_2 for single-phase vapor inclusion in matrix of breccia (SBD088-08) using equation from Yamamoto and Kagi (2006).

8.1.4 Microthermometry

Homogenization temperature (Th) of fluid inclusions in the main stage veins ranges from 132 to 357 °C and that in the matrix of breccia ranges from 148 to 368 °C, which homogenized into a liquid phase (Table 8, Figs. 62a-e, g, h). The temperature of final melting of ice of fluid inclusions in the main stage veins and the matrix of breccia ranges from -5.6 to -2.2 °C (average -4.3 °C) and from -6.0 to -2.5 °C (average -4.0 °C), respectively. Salinity of fluid ranges from 3.5 to 8.0 wt% (average 6.3 wt%) NaCl equivalent in the main stage veins and from 3.9 to 8.5 wt% (average 6.0 wt%) NaCl equivalent in the matrix of breccia (Table 8, Figs. 62f, i). Plotting of salinity (wt.% NaCl equiv.) versus Th shows similar trend between mineralizing veins and matrix of breccia which suggests that they were formed simultaneously from the same ore-forming fluid.

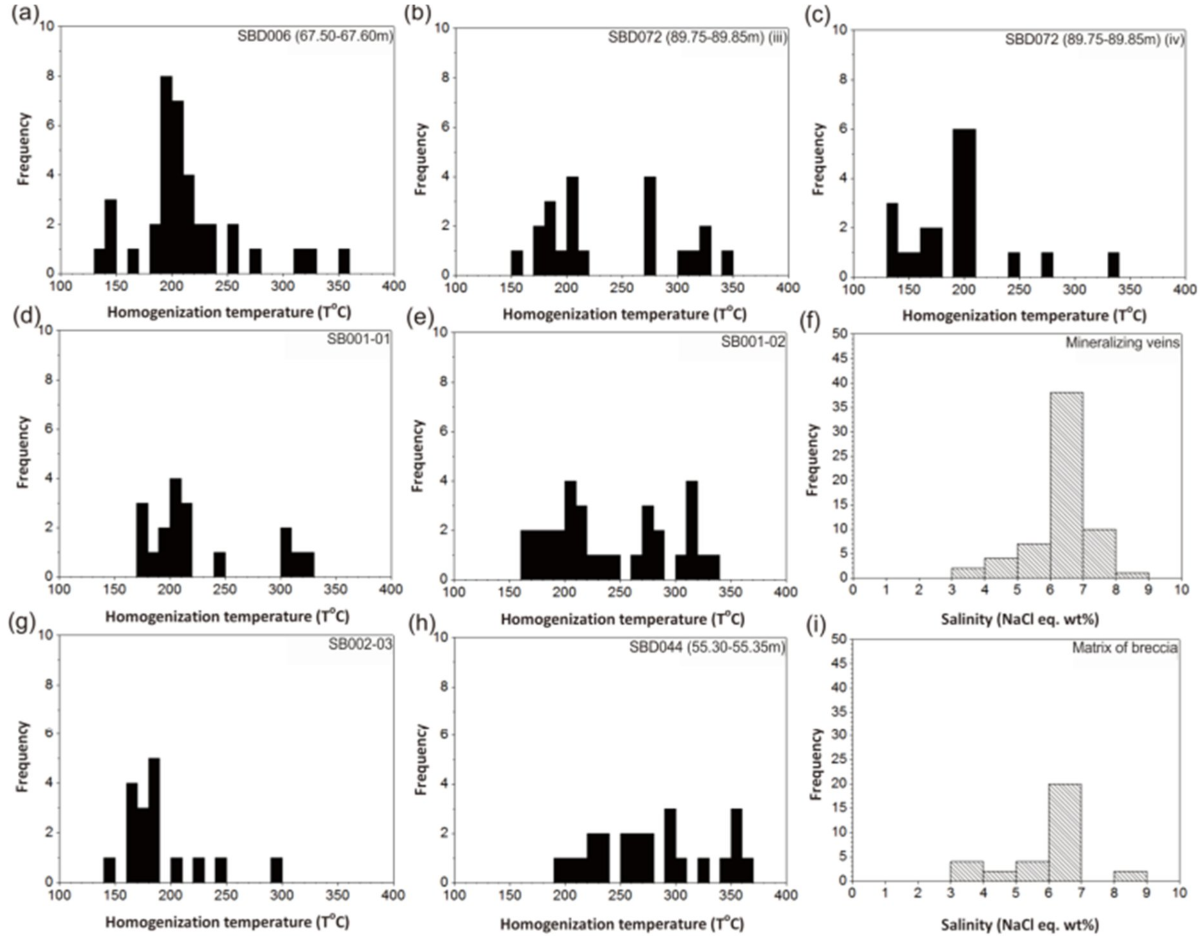

Figure 62. Histograms of homogenization temperature of fluid inclusions in the veins (a-e) and the matrix of breccia (g-h), and histograms of salinity equivalent to NaCl wt% of fluid inclusions in the veins (f) and the matrix of breccia (i) from the Salu Bulo prospect.

Figure 62 shows a wide range of homogenization temperature indicating one of the fluid boiling evidence. On the other hand, co-existence of two-phase liquid-rich and vapor-rich inclusions was observed in one of samples (Fig. 59c). The occurrences of single-phase vapor CO_2 with low density are also considered as other boiling evidence (Fig. 59d). The boiling occurred when ore-forming fluid was trapped in temperature ranges from 190^{o}C to 210^{o}C (Figs. 62a-e, g, h). During the microthermometry analysis, single-phase vapor (carbonic) and two-phase liquid-rich and vapor-rich (aqueous-carbonic) inclusions did not display any phase change diagnostic of liquid CO_2 or clathrate indicating they are categorized into low P_{CO2} (Rosso & Bodnar, 1995). In this case, only ice and vapor CO_2 were observed.

Table 8. Summary of measurement of homogenization temperature and salinity in quartz from different samples in the Salu Bulo prospect.

Bulk ID	Depth (m)	Host rock	Lithology	Vein stage	Mineral	Th (oC)		Salinity (wt% NaCl	
						Range	Mode	Range	Mode
SBD006-16	67.50-67.60	meta-graphitic mudstone (phyllite)	main stage vein	iii	quartz±calcite-albite	102-357	190-200	4.0-7.4	6.5
SBD072-13A	89.75-89.85	meta-chloritic mudstone	main stage vein	iii	quartz±calcite-albite	154-341	200-210	3.5-8.0	5.7
SBD072-13B	89.75-89.85	meta-chloritic mudstone	main stage vein	iv	quartz-calcite-albite	132-336	190-210	4.4-6.9	6.5
SB001-001	surface	meta-chloritic mudstone	main stage vein	iii	quartz	171-321	200-210	5.0-7.7	6.5
SB001-002	surface	meta-chloritic mudstone	main stage vein	iii	quartz±albite	161-332	200-210	3.5-7.3	6.3
SBD044-08	55.30-55.35	meta-chloritic mudstone	breccia	i	quartz-ankerite	197-368	290-300	3.9-8.5	5.7
SB002-003	surface	meta-chloritic mudstone	breccia	iv	quartz-calcite-albite	148-299	180-190	6.0-6.9	6.4

8.2 Stable isotopes

8.2.1 Oxygene isotope

$\delta^{18}O_{SMOW}$ of two quartz samples from massive quartz vein of the main stage yielded +17.2 ‰ and +19.0 ‰ (Table 8, Fig. 63). $\delta^{18}O_{SMOW}$ of H_2O calculated at ~ 205 ^{o}C based on homogenization temperatures of fluid inclusions and isotopic fractionation factor between quartz and water by Clayton et al. (1972) are +5.8 ‰ and +7.6 ‰ (Table 9, Fig. 63), respectively. The oxygen isotope values of water are plotted on all sources of rocks which do not provide a certain source of fluid in the Salu Bulo prospect (Fig. 64).

8.2.2 Sulfur isotope

$\delta^{34}S_{CDT}$ of pyrite with various morphology and texture from host rocks and ores are summarized in Table 10. $\delta^{34}S_{CDT}$ of pyrite narrowly ranges from -2.0 to +3.4 ‰ (Fig. 65). The sulfur isotope values of pyrite are plotted on all source of fluid which does not provide a certain source of sulfur (Fig. 66).

Table 9. $\delta^{18}O_{SMOW}$ of quartz and calculated $\delta^{18}O_{SMOW}$ of H_2O in the Salu Bulo prospect.

Sample ID	Fluid inclusion ID	Depth	Vein stage	Mineral	Temperature [°C]	$\delta^{18}O_{SMOW}$ of quartz (‰)	$\delta^{18}O_{SMOW}$ of H_2O (‰)
SB-044	SB001-001	Surface	iii	quartz	205	+17.2	+5.8
SB-045	SB001-002	Surface	iii	quartz±albite	205	+19.0	+7.6

Note: Locations of samples are indicated in Fig. 32a.

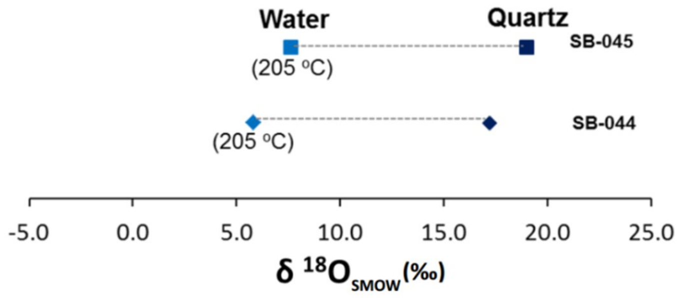

Figure 63. $\delta^{18}O_{SMOW}$ values of quartz and calculated $\delta^{18}O_{SMOW}$ of H_2O in the Salu Bulo prospect.

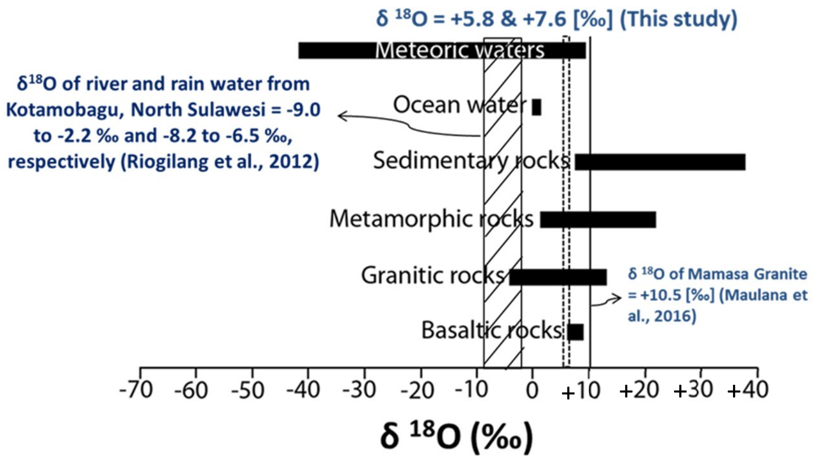

Figure 64. $\delta^{18}O_{SMOW}$ of H_2O in the Salu Bulo prospect compared to the common source of water (after Hoefs, 2015).

Table 10. $\delta^{34}S_{CDT}$ of pyrite with various morphology from host rocks and ores in the drill cores and outcrop in the Salu Bulo prospect.

No.	Drill hole / outcrop	Depth (m)	Host rock	Lithology	Vein	Alteration mineral assemblages	Total sample (n)	Morphology	$\delta^{34}S_{CDT}$ (‰)
1	SBD006	66.75-66.85	Meta-graphitic mudstone	Host rock			n=1	Porous	2.2
2		93.70-94.00	Meta-graphitic mudstone	Alteration halo	late early vein	ankerite-quartz±albite	n=1	Porous	0.2
3	SBD008	65.35-65.42	Meta-chloritic mudstone	Breccia	ii	ankerite±quartz±albite	n=1	Less porous	0.6
4	SBD044	42.90-43.03	Meta-hematitic mudstone	Host rock	pyrite stringer		n=1	Less porous	-1.8
5		45.00-45.20	Meta-hematitic mudstone	Breccia	ii	ankerite±quartz±albite	n=2	Less porous	-1.7 to -0.8
6	SBD053	102.50-102.67	Meta-chloritic mudstone?	Alteration halo			n=1	Less porous	-2
7		104.75-104.80	Meta-graphitic mudstone	Alteration halo	ii	ankerite±quartz±albite	n=3	Porous	-0.1
8	SBD069	23.43-23.50	Meta-hematitic mudstone	Alteration halo	late early vein	ankerite-quartz±albite	n=4	Porous	-0.6 to -0.3
9		54.65-54.85	Phyllite?	Breccia	i	quartz-ankerite±albite	n=1	Porous	-0.3
10	SBD072	72.80-73.05	Meta-sandstone	Altered host rock	ii,iii	ankerite±calcite-quartz±albite	n=1	Less porous	0.9
11	SBD109	59.32-59.42	Phyllite?	Altered host rock	late early vein	ankerite-quartz±albite	n=1	Porous	-1.6
12	SB002	Surface	Meta-chloritic mudstone	Breccia	iv	quartz-calcite-albite	n=2	Less porous	-0.1 to 0
							n=3	Porous	0 to 0.5
							n=1	Aggregated fine-grained	3.4

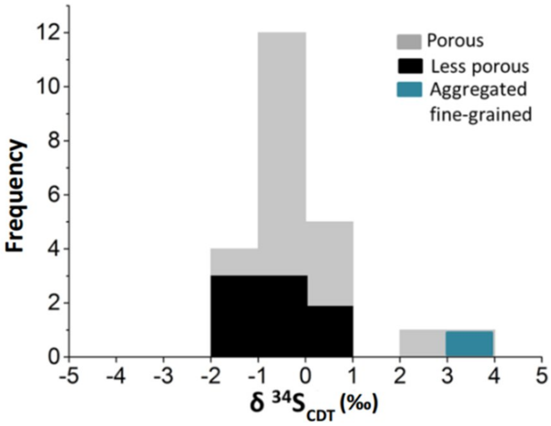

Figure 65. Histogram of $\delta^{34}S_{CDT}$ of pyrite from the Salu Bulo prospect.

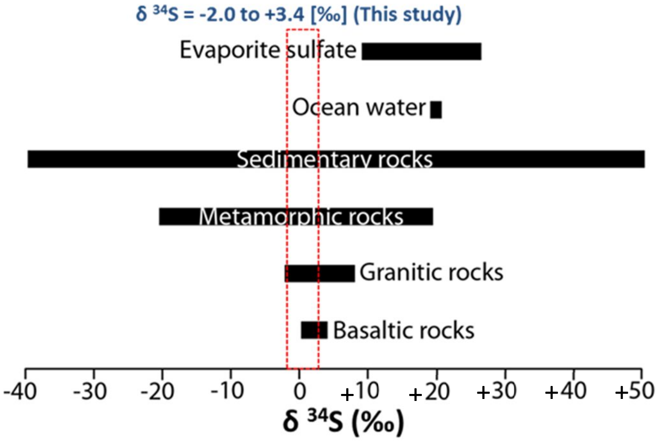

Figure 66. Plot of $\delta^{34}S_{CDT}$ of pyrite from the Salu Bulo prospect compared to the common source of sulfur (after Hoefs, 2015).

CHAPTER IX: DISCUSSION

9.1 Gold mineralization in the metamorphic terrain

Groves et al. (1998) later introduced orogenic type to define gold mineralization that occurs in the metamorphic terrain (i.e., synorogenic, turbidite-hosted, mesothermal and Achaean lode-gold) which is subdivided into epizonal (< 6 km), mesozonal (6-12 km), and hypozonal (> 12 km) based on pressure-temperature condition of ore formation (Groves et al., 1998; Goldfarb et al., 2005). The gold deposits are likely to be formed during compressional to transpressional deformation processes at convergent plate margins in accretionary and collisional orogens (Groves et al., 1998). Ores are mostly hosted in greenschist facies, but can be present in lower and higher grade metamorphic rocks (Goldfarb et al., 2005).

In the lower temperature sulfide minerals are dominantly pyrite and arsenopyrite whereas pyrrhotite is mainly in higher temperature (Goldfarb et al., 2005; Saunders et al., 2014). In the shallow depth which is brittle regimes are dominant, deposit style vary from stockworks and breccias, whereas laminated crack-seal veins and sigmoidal vein arrays are common in brittle-ductile crustal regions and replacement- and disseminated-type are found in the deeper part which ductile environment is dominant (Goldfarb et al., 2005). Orogenic gold deposit is dominated by gold with gold:silver ratios ranging from 1 to 10 and gold fineness is more than 900 (Nesbitt et al., 1986; Goldfarb et al., 2005; Saunders et al., 2014).

Alteration mineral assemblages are generally carbonates, sulfides, muscovite, chlorite, K-feldspar, biotite, tourmaline and albite in low temperature and skarn-like assemblages in high temperature (Goldfarb et. al., 2005) which are reflecting mobility of S, Si, K and CO_2 during hydrothermal activity (Saunders et al., 2014). As, Ag, Sb, B, Hg, Te, Bi, and/or W are consistently enriched in this type of gold deposit (Saunders et al., 2014).

Several origins of ore-forming fluids were proposed to form gold mineralization in orogenic gold deposit namely magmatic, metamorphic-derived and deeply circulating meteoric waters (Kerrich & Fyfe, 1981; Burrows et al., 1986; Nesbitt et al., 1986). Metamorphic fluid in origin is widely accepted as source of ore-forming fluid in this type of gold deposit which is derived from crustal devolatilization process (Kerrich & Fyfe, 1981; Goldfarb et al., 2005; Phillips & Powel, 2010; Bodnar et al., 2014). The ore-forming fluid is near-neutral pH, low to moderate salinities, slightly reduced and dominated by sulfide complexes (Phillips & Powel, 2010; Saunders et al., 2014). The fluid inclusions are generally CO_2-rich inclusions, 4–25 mol%, with little or no H_2O (Bodnar et al., 2014; Saunders et al., 2014). N_2 and CH_4 are detected by Raman spectroscopy and crush/leach analyses in addition to CO_2 indicating more reduced system (Bodnar et al., 2014; Saunders et al., 2014). Homogenization temperatures range from about 150 to 350 ^{o}C (Bodnar et al., 2014).

Oxygen isotope ($\delta^{18}O$) values measured on ore-hosted quartz range between about +10 and +17% and calculated fluids are typically +5 to +10% (Saunders et al., 2014). Large scatters are shown by oxygen and hydrogen isotopic compositions of fluids, but are broadly consistent with a metamorphic source (Bodnar et al., 2014). This is probably as a result of isotopic exchange with later fluids and/or metamorphic rock within traverse long pathways through the crust (Ridley & Diamond, 2000; Bodnar et al., 2014).

Fluid unmixing and/or desulfidation during water-rock interaction are the two most commonly ore precipitation mechanisms in orogenic gold deposit during within pressure fluctuations (Goldfarb et al., 2005; Phillips & Powel, 2010; Saunders et al., 2014). Sulfide precipitation in wall rocks destabilizes bisulfide complexes causing deposition of gold in the alteration halos (Reed, 1997; Wilkinson, 2001; Phillips & Powel, 2010; Saunders et al., 2014).

The specific model(s) for this type of gold deposit remains controversial. However, several gold deposits host in metamorphic rocks show characteristics of epithermal gold deposit (i.e., Poboya in Sulawesi, see Chapter II).

9.2 Epithermal gold

In the upper crust (surface to 2 km depth), epithermal gold deposits are formed over the temperature ranges from < 150 to 300 ^{o}C, largely in the volcano-plutonic arcs associated with calc-alkaline to alkaline magmatism in volcanic arcs at convergent plate margins, as well as in intra-arc, back-arc and post-collisional rift settings (Hedenquist et al., 1996; Simmons et al., 2005). Epithermal gold deposits are mainly hosted by volcanic rocks and contemporaneous volcanogenic sedimentary rocks and sometimes in basement units (e.g., Baguio district, Hishikari, Porgera) (Hedenquist et al., 1996).

In general, epithermal gold deposit is divided into low- and high-sulfidation which are usually structurally controlled (Hedenquist et al., 1996). Open space filling (e.g., crustiform-colloform and lattice textures and mineral druses) and multiple generations of breccia are common in low-sulfidation deposits, whereas disseminated ore with much lower in grade but greater in total tonnage is common in high-sulfidation deposits (Hedenquist et al., 1996; Simmons et al., 2005). On the other hand, leaching by acidic fluid (pH < 2) forms massive bodies of residual (vuggy) quartz which is the most characteristic feature in high-sulfidation ore deposits (Hedenquist et al., 1996). Quartz is ubiquitous in low- and high-sulfidation. Near-neutral pH is typical ore-forming fluid in low-sulfidation indicated by adularia and calcite, while in high-sulfidation in which acidic condition is dominant kaolinite and alunite are common but minor as gangue (Hedenquist et al., 1996; Simmons et al., 2005).

Low-sulfidation deposit commonly contains arsenopyrite and high-Fe sphalerite and is enriched in Ag, As, Au, Hg, Sb, Se, Te and locally Tl (Hedenquist et al., 1996; Saunders et al., 2014). High-sulfidation deposit commonly contains Cu-bearing sulfide and sulfosalts such as enargite, luzonite, covellite, tetrahedrite and tennantite, as well as sphalerite and telluride minerals (Hedenquist et al., 1996; Simmons et al., 2005). At a deeper level Cu, Pb, and Zn are locally abundant and enriched to form intermediate-sulfidation deposit (Saunders et al., 2014). In addition, low-sulfidation deposit may be enriched in Mo, Sn, V and W in their altered wall rock (Jensen & Barton, 2000; John et al., 2003; Simmons et al., 2005).

Homogenization temperatures of fluid inclusions in epithermal deposits range from < 100 to > 450°C which is the most data range between 120 and 310 °C (Bodnar et al., 2014). The salinities range from 0 to > 40 wt% NaCl which is the most data range between 0 and 17 wt% NaCl, and the majority of the salinities is < 10 wt% (Bodnar et al., 2014). The low salinities indicate Au (and Ag) in epithermal gold deposits are transported as sulfur complexes rather than chloride complexes (Bodnar et al., 2014). CO_2 was reported in epithermal deposits detected by crushing tests or by Raman or mass spectrometric analysis along with H_2S, CH_4, N_2 and SO_2 (Roedder, 1984; Bodnar et al., 1985) which are in low concentration and not present as a separate phase (Roedder, 1984). Its presence significantly affects the depth at which boiling (immiscibility) occurs (Barton & Chou, 1993; Bodnar et al., 1985; Hedenquist & Henley, 1985).

Oxygen and hydrogen isotopic compositions of fluid inclusions from epithermal deposits show trends that extend from magmatic compositions to the meteoric water line, which are closer to the magmatic end for epithermal base metal deposits and to the meteoric end for epithermal precious metal deposits (Bodnar et al., 2014). Boiling and/or cooling and/or fluid mixing are common metal precipitation mechanisms in most of epithermal ores (Saunders et al., 2014). Loss of volatiles (i.e., H_2S, H_2 and CO_2) during boiling and/or fluid mixing causes a change in redox potential and an increase in pH of the residual liquid phase, which is encountered in the upper part of geothermal or epithermal systems, removes sulfide sulfur from fluid to destabilize gold-bisulfide complex (Hedenquist et al., 1996; Seward et al., 2014). Consequence of boiling is represented by lattice-textured bladed calcite (Hedenquist et al., 1996).

9.3 Gold mineralization in the Awak Mas district

The geology and mineralization of the Awak Mas project have been firstly described during 1990's in several unpublished reports by consultants (Archibald et al., 1996; Smillie, 1996; White, 1999). Later studies in 2000's done by company, academic staffs and researchers' provided more information and discussion in alteration and mineralogy, fluid characteristics and gold precipitation mechanism in Awak Mas project (Querubin & Walters, 2011; Idrus et al., 2015; Harjanto et al., 2016; Hakim & Melcher, 2016; Harjanto 2017; Hakim et al., 2017; 2018). Within those studies, the Salu Bulo prospect was lesser studied (White, 1999; Hakim & Melcher, 2016; Hakim et al., 2018).

Recent studies by Harjanto (2017), Hakim (2017) and Hakim et al., (2018) provided detail study in Awak Mas prospect using sophisticated laboratory analyses. They concluded the Awak Mas deposit is an epigenetic, epizonal orogenic gold deposit that shows following characteristics: 1) developed at minimum temperatures between 275 and 325 °C in depth of about 4.8 km with dominance of brittle structures and open-space filling textures; 2) relatively high As-Sb concentrations; 3) gold occurs in pyrite as sub-microscopic inclusions and as fracture fillings of deformed pyrite with a gold fineness from 925 to 935 and Au:Ag ratios between 12:1 and 14:1; 4) metamorphic origin of ore-forming fluid indicated by halogen data from dewatering of organic-rich marine sedimentary rocks with negligible magmatic input, with CO_2-poor, low to moderate salinity of fluid inclusions; and 5) The $\delta^{34}S$ values of pyrite between +0.6 and +12.9 ‰ emphasizing the metamorphic character of the ore-forming fluid.

One Asia (in an unpublished report) was newly proposed a new geological model for Awak Mas deposit. The gold mineralization was related to late stage intrusive or magmatic event that occurred in the late Miocene or Pliocene age (younger than about 8 million years) which became source for ore-forming fluid. The magmatic event induced regional doming and fault networking facilitating upward migration of fluid to concentrate along a suite of north to northeast striking faults as well as along earlier more horizontal foliations or imbricate thrust and/or extensional faults. Shallowly dipping (foliation parallel) mineralization is dominant while steeply dipping crosscutting mineralization is locally hosting higher grade ores. The mineralization appears to occur within a variety of different host rocks (i.e., meta-sedimentary sequences and basement gneisses and intrusives).

As analogous of the Awak Mas prospect, the Salu Bulo prospect was also concluded as typical epizonal orogenic gold deposit, discriminated based on 1) veins are hosted by fine-grained meta-sedimentary and -volcanic rocks; 2) high intensity of carbonatization (siderite+ankerite), chloritization and albitization; 3) mineralization formed through compressional deformation and fault reactivation; 4) high Au:Ag ratio (8.5:1 to 9:1); 5) formation at moderate temperature (i.e., 175 to 350 °C) (Hakim & Melcher, 2016).

Despite more and detail information have been provided some questions are still considerable uncertainty particularly in origin of fluid and how the fluid migrates from depth level to form gold mineralization in the Awak Mas project.

9.4 Characteristics of gold Mineralization in the Salu Bulo prospect

The Salu Bulo prospect is located 1.8 km toward southeast from the Awak Mas prospect (Fig. 8). It is the nearest gold prospect in the Awak Mas project located to Kandeapi Suture, a boundary between Latimojong Metamorphic Complex and Lamasi Complex (Figs. 8, 9, 13). It is considered to be analogous to the Awak Mas prospect with steeply dipping gold mineralization.

9.4.1 P-T condition

The depth of formation has been estimated using the phase equilibrium properties (boiling point with depth curve) for the appropriate fluid composition (6 wt% NaCl equiv.) (Haas, 1971) (Fig. 67). Evidence of fluid boiling in the Salu Bulo prospect shown by wide range of homogenization temperature of fluid inclusions in the main stage veins and matrix of breccia and co-existence of two-phase liquid-rich and two-phase vapor-rich inclusions, in addition to single phase vapor CO_2 and liquid H_2O inclusions. Based on mode of homogenization temperature of fluid inclusions in the main stage veins and matrix of breccia, the trapping temperature is assumed to range from 190 to 210 °C in which the fluid inclusions were homogenized to liquid (Figs. 62a-e, g, h).

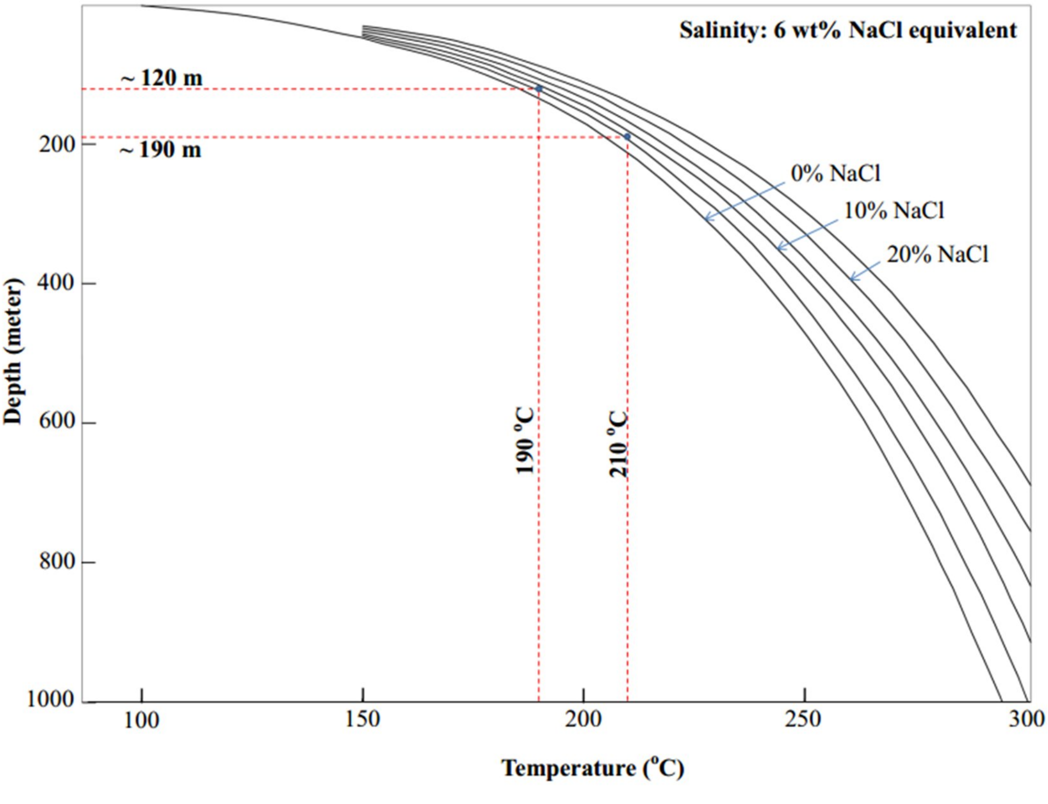

Figure 67. Plot of homogenization temperatures of two-phase liquid-rich inclusion for 6 wt% NaCl equiv. on the boiling point curves from Haas (1971) showing formation depth of gold mineralization in the Salu Bulo prospect.

Assuming boiling under hydrostatic conditions, the fluid boiling occurred at approximately 120-190 m below the paleo-water table and the calculated pressure was 1.2-

1.9 MPa (Fig. 67). The relatively low pressure is consistent with the occurrences of CO_2 vapor in fluid inclusions with low density ranging from 0.1 to 0.14 g/cm^3 that was released during boiling of ore-forming fluid triggered by pressure drop during formation of veins and breccia.

9.4.2 Origin of mineralizing fluid

Carbonate and albite alteration in the Salu Bulo prospect was probably formed by CO_2-bearing sodic mineralizing fluid. This is supported by the presence of CO_2 in low to moderate salinity (3.5 to 8.5 wt% NaCl equiv.) of fluid inclusions, and albite alteration along the main stage veins and in the breccia. Carbonate alteration was formed by the reaction between CO_2-bearing fluids and host rocks. CaO and Na_2O were added by the hydrothermal activity and resulted in the carbonatization and albitization, respectively, in altered host rock and ores, while potassic alteration is absent (Fig. 41).

Riogilang et al. (2012) reported oxygen isotope of river and rain water from Kotamobagu, Northern Sulawesi ranging from -9.0 to -2.2 ‰ and -8.2 to -6.5 ‰, respectively (Figs. 64, 68). Kusnadi and Setiawan (2009) reported oxygen and hydrogen isotopes of hot and cool waters from Bittuang geothermal system, Toraja, South Sulawesi ranging from -10.08 to -1.42 ‰ and -67.1 to -42.9 ‰ (Fig. 68). Two of hot water samples from Balla area namely Balla-1 and Balla-2 indicate oxygen isotope enrichment during its circulation prior to form hot springs. The calculated $\delta^{18}O_{SMOW}$ of water of hydrothermal fluid in the Salu Bulo prospect is +5.8 ‰ and +7.6 ‰. The value gives no signature for certain origin of fluid (Figs. 64, 68). No relationship with the volcanic and magmatic activity was recognized so far in the Salu Bulo prospect. Veins, stockwork and breccia ores in the Salu Bulo prospect reflecting those formed in relatively shallow depth in which this condition is dominantly meteoric water in origin. However, the calculated $\delta^{18}O_{SMOW}$ of water of hydrothermal fluid in the Salu Bulo prospect is distinctly higher and not consistent with general meteoric water. Those conditions suggest the ore-forming fluid in the Salu Bulo prospect has probably undergone oxygen isotopic exchange with the wall rocks during its circulation at deeper portion prior to the gold mineralization at shallow depth (Fig. 68).

Elevated Ni content of intensely altered host rocks, ores and pyrite, and the positive correlation between Au and Ni was probably caused by deep circulation of meteoric water. Susilo (1998) reported Ni contents in the Latimojong Metamorphic Complex range from 243 to 274 ppm. Mo content is not significantly enriched in the intensely altered host rocks and ores but it is positively correlated with gold indicating the presence in the ore-forming fluid. The deeply circulated meteoric water might have been enriched with Na to form albite alteration.

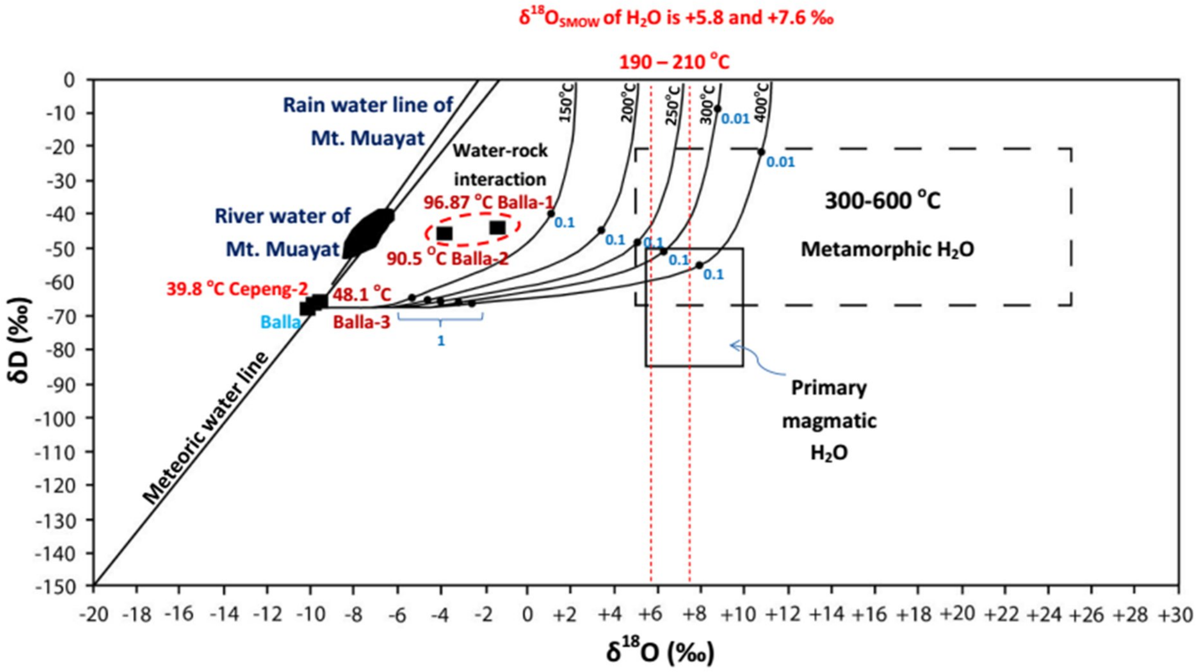

Data source: Kusnadi and Setiawan (2009); Riogilang et al. (2012)

Figure 68. Plot of $\delta^{18}O_{SMOW}$ values of water in the Salu Bulo prospect showing oxygen shift during deep circulation of meteoric water (Modified from Taylor, 1974).

Considering the larger volume of fluid is required to form a gold deposit. Deep-circulated meteoric water suggested as ore-forming fluid in the Salu Bulo prospect becomes questionable along with lack of hydrogen isotope data. Assuming the initial oxygen and hydrogen isotopes of ore-forming fluid in the Salu Bulo prospect was similar to cool water in

Balla area namely -10.08 ‰ and -67.1 ‰, respectively (Fig. 68), water rock-interaction between wall rocks and hydrothermal fluid during deep-circulated meteoric water to form ore-forming fluid of the Salu Bulo prospect could be calculated. Figure 68 shows the calculated $\delta^{18}O_{SMOW}$ of water of hydrothermal fluid in the Salu Bulo prospect that is +5.8 ‰ and +7.6 ‰ suitable in equal or less than 0.001 of water-rock ratio in temperature ranging from 200 to 250°C or 0.1 to 0.001 of water-rock ratio in temperature ranging from 250 to 300°C or more than 0.1 of water-rock ratio in temperature ranging from 300 to 400°C indicating rock-dominant oxygen isotopic composition of ore-forming fluid in the Salu Bulo prospect. These conditions are depending on initial isotopic compositions of wall rock and weight percent of oxygen and hydrogen in water to that rock which are assumed to be 12.5 ‰ $\delta^{18}O$ and -32 ‰ δD based on average value of isotopic composition of metamorphic rock, and 50 wt% oxygen and 0.28 wt% hydrogen, respectively (Field & Fifarek, 1985). On the other hand, the similarity of vein composition shown by early vein stage (i.e., ankerite-quartz±albite) which was formed during metamorphism and vein (ii) of the main stage (i.e., ankerite±quartz±albite) indicates possibly influence of metamorphic fluid.

$\delta^{34}S_{CDT}$ of pyrite is plotted on all source of sulfur (Fig. 66). However, the narrow range of $\delta^{34}S_{CDT}$ of pyrite suggests a single source of sulfur (Fig. 65). Sulfur isotope of pyrite in unaltered host rocks and aggregated fine-grained pyrite in clast of breccia are higher than in the altered host rocks and ores which is +2.2 and +3.4 ‰ (Table 9, Fig. 65). Sulfur isotope of pyrite in the altered host rocks and ores ranges from -1.8 to +0.9 ‰ (Table 9, Fig. 65). Signature of magmatic influence in the Salu Bulo prospect, aside from narrow range of sulfur isotope value, is weakly recognized i.e., Mo and W contents in intensely altered host rocks and ores in which positively correlated with Au and CO_2 and N_2 vapors in fluid inclusions. These conditions suggest during hydrothermal activity the initial sulfur was slightly changed becoming lower value influenced by magmatic sulfur source.

9.4.3 Gold precipitation mechanism

The mineral assemblage of veins of the main stage and that of matrix of breccia are identical, consisting of quartz, ankerite, calcite and albite. Because the host rocks are less reactive and less permeable, alteration halo along the main stage veins are relatively narrow. On the other hand, the stockwork and breccia host the high gold grade ores in the Salu Bulo prospect.

Geochemistry of unaltered and altered host rocks and ores shows signature of water-rock interaction during the hydrothermal activity indicated by positive correlation between Au and Ni and high Ni content in pyrite (Figs. 50-55, Appendix 5), albite alteration by decomposed of k-bearing minerals and addition of sodium from solution (Fig. 43a), carbonate alteration by introduced of CO_2 from ore-forming fluid (Figs. 43b, c); and mobility and fractionation of REE by depleted of total REE in intensely altered host rock and ores (Fig. 45). The occurrences of pyrite and native gold, electrum observed mainly in altered host rocks and breccia that consist of ankerite (±calcite), quartz, albite and pyrite along with minor sericite than in the veins suggest that the water-rock interaction played an important role for gold mineralization in the Salu Bulo prospect. Water-rock interaction facilitated chemical changes in the ore-forming fluid that favor gold precipitation (Phillips & Groves, 1984). Gold occurs as electrum and native gold with Au/(Au+Ag) ratio ranging from 66.2 to 82.3 atomic % Au (Table 6, Fig. 57).

The Fe_2O_3 content of the host rocks ranges from 5.7 to 10.2 wt%, and Fe/(Fe+Mg) molar ratio ranges from 0.6 to 0.8 (Table. 3). The mafic host rocks interacted with the ore-forming fluid and caused the wall-rock sulfidation and carbonate alteration. Ankerite was the dominant carbonate mineral formed by the process which is suitable for higher or equal to 0.5 of Fe/(Fe+Mg) molar ratio (Goldfarb et al., 2005). On the other hand, dolomite was identified as a single mineral inclusion in the matrix of crackle breccia. Sulfidation of wall rock occurred as a mechanism to form pyrite by consuming sulfur in the ore-forming fluid (Wilkinson, 2001; Phillips & Powell, 2010). Calculated pH of ore-forming fluid in the Salu Bulo prospect at 200 ^{o}C and 6 wt% NaCl equiv. is 6.07 with mass concentration of Chlorine (Cl) is 49.97 gram/liter, while calculated pH of water at 200 ^{o}C is 5.6. The dominant albite-carbonate alteration in the Salu Bulo prospect was formed by near neutral-slightly alkaline ore-forming fluid, in which gold was dissolved as $Au(HS)_2^-$ complex (Phillips & Powell, 2010). In addition, positive Eu anomaly in intensely altered host rocks and ores was probably related to low oxygen fugacity (reduced nature) of fluid which is suitable for soft base anions such as HS^-, S^{2-}, SCN^-, $S_2O_3^{2-}$, CO, CH_4, and low values of $Eu^{3+/}Eu^{2+}$, Eu is dominated by Eu^{2+} (Chen & Zhao, 1997). Formation of pyrite through wall-rock sulfidation destabilized the $Au(HS)_2^-$ complex in the ore-forming fluid to precipitate native gold and electrum (Reed, 1997; Wilkinson, 2001; Phillips & Powell, 2010). The occurrences of gold mainly as filling in fractures and pores in pyrite suggest that pyrite formed earlier, thus had a role in precipitating gold (electrochemically). On the other hand, CO_2 was removed from the ore-forming fluid to form carbonatization in the altered host rocks and ores (i.e. breccia) changing pH condition in the ore-forming fluid to precipitate native gold and electrum along with albite (Neall & Phillips, 1987). In addition, fluid boiling is also a probable mechanism to precipitate native gold and electrum in the Salu Bulo prospect.

9.5 Genetic model

Gold mineralization in the Salu Bulo prospect was epigenetic. It occurred after the metamorphism of the host rocks and related to cataclastic breccia, veins and stockworks that were formed during an episode of crustal extension forming steeply dipping normal faulting and brecciation. The gold mineralization was formed in low temperature (190 to 210 °C) and pressure (1.2 to 1.9 MPa). Meteoric water infiltrated through fracture zone facilitated by emplacement of Lamasi Complex and Toraja Formation. Connected fractures allowed the meteoric water infiltrated in the deeper level possibly about ~ 6-8 km (gradient geothermal) and increased the temperature of the fluid and extensive water-rock interaction (Nesbitt et al., 1986).

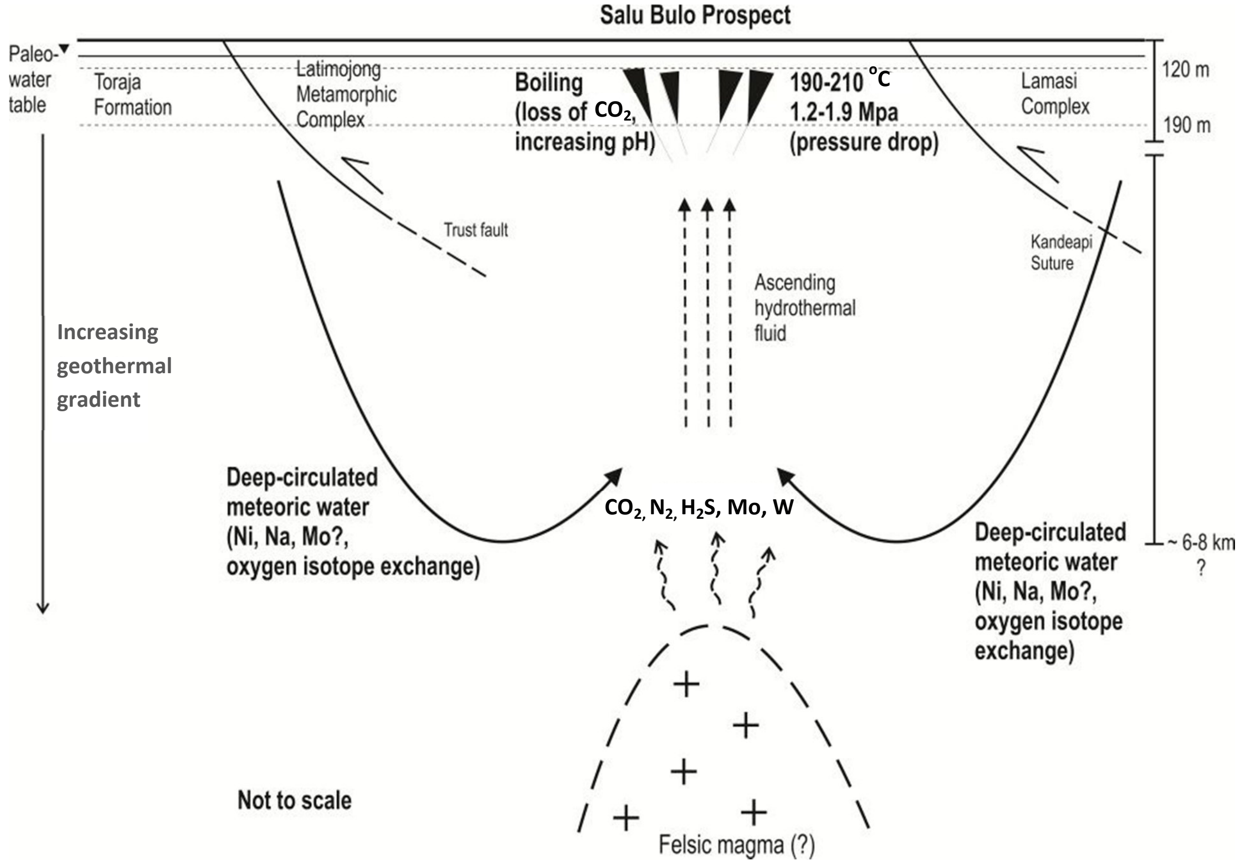

Figure 69. Genetic model of gold mineralization in the Salu Bulo prospect.

During water-rock interaction in the deeper level, the hydrothermal fluid leached Ni in the mafic wall rock and possibly Mo, enriched in Na content, and increased the initial oxygen isotope, salinity and pH and possibly CO_2 content (Fig. 69). The hydrothermal fluid was probably heated by felsic magma that contributed to volatiles (i.e., CO_2, N_2 and H_2S) and Mo and W contents in the fluid. The hydrothermal fluid cooled and rose up through fractures and related structures and precipitated gold in the Salu Bulo prospect in the shallow depth ranging from 120 to 190 meters below the paleo water table. Pressure drop during brittle deformation triggered fluid boiling that caused loss of CO_2 increasing pH of hydrothermal fluid to precipitate carbonate and albite alteration in the Salu Bulo prospect (Fig. 69). Water-rock interaction later locally occurred in deposit site caused sulfidation in the iron-rich host rocks to precipitate pyrite and later gold as filling and inclusion in pyrite in intensely altered host rocks and ores. Ni content in the ore-forming fluid was also probably locally leached from Latimojong Metamorphic Complex during water-rock interaction in the site of ore deposition.

9.6 Timing of gold mineralization and tectonic setting

Based on the genetic model, the gold mineralization in the Salu Bulo prospect was formed after or during unidentified magmatism beneath the Latimojong Region. Diorite was observed during field works on Awak Mas project and the surrounding area, but it occurrences suggest it is part of Latimojong Metamorphic Complex (Fig. 12c). Spider diagram of trace element concentrations of meta-volcanic rock and meta-volcaniclastic rock from the Salu Bulo prospect that normalized to Chondrite (Sun & McDonough, 1982) shows a similar pattern to mid-ocean ridge basalt (MORB) than ocean island basalt (OIB) (Fig. 70). On the other hand, Susilo (1998) reported meta-volcanic rocks from Latimojong Metamorphic Complex were calc-alkaline and island-arc tholeiitic rock that formed before Middle Cretaceous in the active continental margin after deposition of shallow siliciclastic deposit in the fore arc (Susilo, 1998).

White et al. (2017) dated two dacites and a felsic dyke that were emplaced between 6 and 8 Ma and 3.9 Ma, respectively that cross-cut part of the Latimojong Metamorphic Complex. Those are classified into part of Enrekang Volcanic Series based on their age, geochemistry and petrology. The dacites and felsic dyke interestingly yield similar ages and compositions to the Palopo Granite which are possibly equivalent to each other (White et al., 2017). These plutonic and volcanic rocks formed during a renewed phase of magmatism that were related to crustal extension (Maulana et al., 2016) and/or flux-melting of the mantle wedge driven by subduction produced the high-K granitoids and volcanics of Palopo Granite/Enrekang Volcanic Series in the Late Miocene to Pliocene (White et al., 2017). These conditions were probably related to D3 (brittle deformation) in the Latimojong Metamorphic Complex to form a major episode of late extension of normal faulting and brecciation which is related to gold mineralization the Awak Mas district, particularly north-south trending and dipping steeply eastward ore bodies of the Salu Bulo prospect.

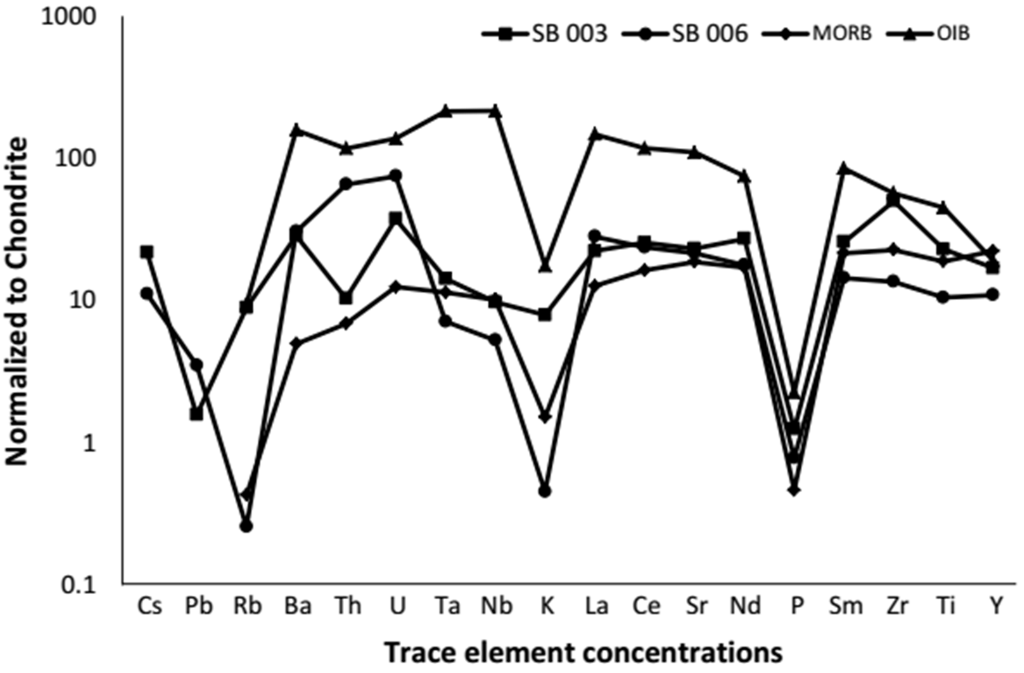

Figure 70. Trace element concentrations of meta-volcanic rock and meta-volcaniclastic rock, average N-type MORB from Saunders & Tarney (1984): and OIB from Sun (1980) normalized to the chondritic meteorites (Sun & McDonough, 1989).

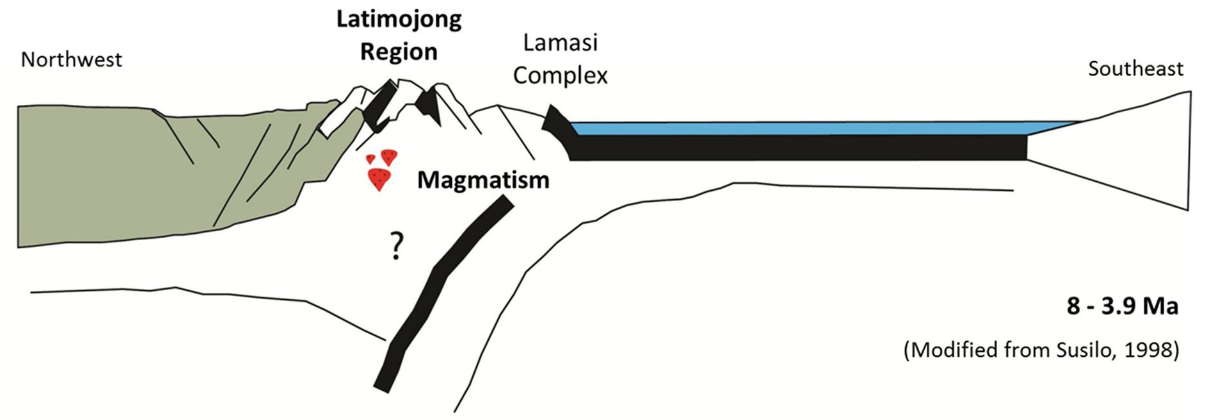

Figure 71. Tectonic setting of Latimojong region during 8-3.9 Ma (Modified from Susilo, 1998).

Based on their characteristics, the Salu Bulo prospect occurred in epithermal conditions. It was formed from low-moderate salinity deep-circulated meteoric water at temperature ranging from 190 to 210 °C and depth ranging from 120 to 190 m. It is different from the previous studies that concluded the Awak Mas project is a mesothermal or orogenic gold deposit. On the other hand, albite alteration is uncommon in epithermal gold deposits, which is usually formed in temperature approximately between 400 to 600 °C (Pollard, 1983). But it was rarely reported in the propylitic zone of alteration along with quartz, calcite, chlorite sericite, pyrite and rarely epidote in the Chelopech high-sulfidation epithermal Cu-Au deposit, Bulgaria (Georgieva, 2014). Propylitic alteration is representing low to intermediate temperatures ranging from 200 to 350 °C (Robb, 2005).

CHAPTER X: CONCLUSIONS

1. Veins were formed in three stages, classified as early, main and late stages. Gold mineralization is mainly related to the main stage veins. The main stage veins and matrix of the breccia have identical mineral assemblage, which is characterized by quartz, carbonate (mainly ankerite), albite and pyrite.
2. High-grade gold ore in the Salu Bulo prospect is associated with intense alteration, which includes carbonatization, albitization, silicification and sulfidation of the veins and breccia. The mineralogy consists of ankerite (±calcite), quartz, albite and pyrite along with minor sericite.
3. Pyrite is the most abundant sulfide, which is spatially related to native gold and electrum (< 2-42 μm in size). Pyrite is more abundant as dissemination in the altered host rocks than in the veins. Ni and Co concentrations are high in pyrite, 10 - 7780 ppm and 390 - 2710 ppm, respectively, in edges, cores and rims of py2, py3 and py5 with zoning.
4. Bulk chemical composition of intensely altered host rocks and ores shows a positive correlation between Au and Ag, Ni, Mo, Na. Whole-rock Au:Ag ratio of intensely altered host rocks and ores ranges from 1.5 to 7.0 (average 4.4). Gold occurs as electrum and native gold with Au/(Au+Ag) ratio ranging from 66.2 to 82.3 atomic % Au.
5. K_2O is consistently depleted in intensely altered host rocks and ores reflecting absent of potassic alteration. Depletion of total REE in intensely altered host rocks and ores are evidence for mobility and fractionation of REE during hydrothermal alteration through water-rock interaction.
6. Fluid inclusions in the veins and matrix of breccia are mainly two-phase liquid-rich inclusions and minor two-phase vapor-rich and single-phase liquid or vapor inclusions. Laser Raman microspectrometry detected CO_2 and N_2 gases in the fluid inclusions. Fluid

boiling occurred during trapping at approximately 120-190 m below the paleo water table.

7. $\delta^{18}O_{SMOW}$ values of hydrothermal fluid calculated from $\delta^{18}O$ of quartz from massive quartz vein of the main stage are +5.8 ‰ and +7.6 ‰. It suggests oxygen isotopic exchange between the fluid and wall rocks. $\delta^{34}S_{CDT}$ of pyrite narrowly ranges from -2.0 to +3.4 ‰ indicating single source of sulfur.
8. Sulfidation of the wall-rock reduced the activity of bisulfide in the hydrothermal fluid, which caused the precipitation of native gold and electrum.
9. Gold mineralization in the Salu Bulo prospect occurred in epithermal conditions after the metamorphism of the Latimojong Metamorphic Complex and emplacement of Palopo Granite or Enrekang Volcanic Series in the Late Miocene to Pliocene. It was formed from low-moderate salinity fluids at temperature ranging from 190 to 210 °C and pressure ranging from 1.2 to 1.9 MPa.

REFERENCES

Archibald, N. J., Power, W. L., Ketelaar, P. B., Utley, D. C., Panizza, N. and Nichols, S. N. (1996) Geology of the Awak Mas Prospect Area, South Central Sulawesi, Indonesia. Prepared for PT Masmindo Eka Sakti, Fractal Graphics, Western Australia, Unpubl, 22p.

Barton, P. B. and Chou, I. (1993) Refinement of the evaluation of the role of CO_2 in modifying estimates of the pressure of epithermal mineralization. Economic Geology, 88, 873–884.

Bergman, S. C., Coffield, D. Q., Talbot, J. P. and Garrard, R. A. (1996) Tertiary tectonic and magmatic evolution of Western Sulawesi and the Makassar Strait, Indonesia: Evidence for a Miocene continent-continent collision *in*: Hall, R. and Blundell, D. J. (eds.) Tectonic Evolution of Southeast Asia. Geological Society of London Special Publication, 106, 391-430.

Best, M. G. (2003) Igneous and Metamorphic Petrology. Blackwell, Turin, 729p.

Bodnar, R. J. (1993) A method of calculating fluid inclusion volumes based on vapor bubble diameters and P-V-T-X properties of inclusion fluids. Economic Geology, 78, 535-542.

Bodnar, R. J., Lecumberri-Sanchez, P., Moncada, D. and Steele-Maclnnis, M. (2014) Fluid inclusions in hydrothermal ore deposits. Treatise on Geochemistry 2nd Edition, Elsevier, 119-141.

Bodnar, R. J., Reynolds, T. J. and Kuehn, C. A. (1985) Fluid-inclusion systematics in epithermal systems *in*: Berger, B. R. and Bethke, P. M. (eds.) Geology and Geochemistry of Epithermal System. Society of Economic Geologist, Review in Economic Geology Volume, 73–97.

Burke, E.A.J. (2001) Raman microspectrometry of fluid inclusions, Lithos, 55, 139-158.

Burrows, D. R., Woods, P. C. and Spooner, E. T. C. (1986) Carbon isotope evidence for a magmatic origin for Archaean gold-quartz vein ore deposits. Nature, 321, 851–854.

Calvert, S .J. and Hall, R. (2007) Cenozoic evolution of the Lariang and Karama regions, North Makassar Basin, western Sulawesi, Indonesia Petroleum Geoscience, 13, 353–368.

Chen, Y. J. and Zhao, Y. C. (1997) Geochemical characteristics and evolution of REE in the Early Precambrian sediments: evidences from the southern margin of the North China Craton. Episodes, 20, 109-116.

Clayton, R. N., O'Neil, J. R. and Mayeda, T. K. (1972) Oxygen isotope exchange between quartz and water. Journal of Geophysical Research, 77, 3057-3067.

Coffield, D. Q., Bergman, S. C., Garrard, R. A., Guritno, N., Robinson, N .M. and Talbot, J. (1993) Tectonic and Stratigraphic Evolution of the Kalosi PSC Area and Associated Development of a Tertiary Petroleum System, South Sulawesi, Indonesia. In: Proceedings of the Indonesian Petroleum Association 22nd Annual Convention, 679–706.

Djuri, Sudjatmiko, Bachri, S. and Sukido (1998) Geological Map of the Majene and Western Part of the Palopo Sheets, Sulawesi (1:250,000). Geological Research and Development Centre, Bandung, Indonesia.

Elburg, M. and Foden, J. (1999) Source for magmatism in Central Sulawesi: Geochemical and Sr-Nd-Pb isotopic constraints. Chemical Geology, 156, 67-93.

Field, C. W. and Fifarek, R. H. (1985) Light stable-isotope systematics in the epithermal environtment *in*: Berger, B. R. and Bethke, P. M. (eds.) Geology and Geochemistry of Epithermal System. Society of Economic Geologist, Review in Economic Geology Volume 2, 99-128.

Georgieva, S. (2014) Albite in the propylitic zone of alteration from the Chelopech high-sulphidation epithermal Cu-Au deposit, Bulgaria: new data. National Conference with International Participation "Geosciences 2014", Bulgarian Geological Society, 21-22.

Goldfarb, R. J, Baker T., Dube, B., Groves, D. I., Hart, C., JR., Gosselin, P. (2005) Distribution, character, and genesis of gold deposits in metamorphic terranes. Economic Geology, 100th Anniversary Volume, 407-450.

Groves, D., Goldfarb, R., Gebre-Mariam, M., Hagemann, S. and Robert, F. (1998) Orogenic gold deposits: a proposed classification in the context of their crustal distribution and relationship to other gold deposit types. Ore Geology Review. 13, 7–27.

Haas, J. L. (1971) The effect of salinity on the maximum thermal gradient of a hydrothermal system at hydrostatic pressure. Economic Geology, 66, 940–946.

Hakim, A.Y.A. (2017) Genesis of Orogenic Gold in the Latimojong District, South Sulawesi, Indonesia (Ph.D. thesis). Montanuniversität Leoben, Austria, 355p.

Hakim, A. Y. A. and Melcher, F. (2016) The Sallu Bulo mesothermal gold deposit in South Sulawesi, Indonesia. GeoTirol 2016, 98 (abstract).

Hakim, A. Y. A., Melcher, F., Prochaska, W., Bakker, R. and Rantitsch, G. (2018) Formation of epizonal gold mineralization within the Latimojong Metamorphic Complex, Sulawesi, Indonesia: Evidence from mineralogy, fluid inclusion and Raman spectroscopy. Ore Geology Reviews, 97, 88-108.

Hall, R. (2002) Cenozoic geological and plate tectonic evolution of SE Asia and the SW Pacific: computer-based reconstructions, model and animations. Journal of Asian Earth Sciences, 20, 353-431.

Hamilton, W. (1979) Tectonic of the Indonesia Region. United States Geological Survey Professional Paper, 1078, 345p.

Hara, H., Kurihara, T., dan Mori, H., (2013): Tectono-straturaphy and low-grade metamorphism of Late Permian and Early Jurassic accretionary complexes within the Kurosegawa belt, Southwest Japan: Implications for mechanisms of crustal displacement within active continental margin. Tectonophysics, 592, 80-93.

Harjanto, E. (2017) Hydrothermal Alteration and Gold Mineralization of the Awak Mas Gold Deposit, Sulawesi Island, Indonesia. Mainz, G, Aachen, 200 Seiten.

Harjanto, E., Meyer, F. M. and Idrus, A., Widyanarko, H. and Endrasari, N. L. (2016) An update characteristics of Awak Mas mesothermal gold deposit, Sulawesi Island, Indonesia. Proceedings of Unconventional Exploration Target & Latest Technique and New Tools in Mineral and Coal Exploration, Bandung.

Hedenquist, J. W. and Henley, R. W. (1985) The importance of CO_2 on freezing point measurements of fluid Inclusions: Evidence from active geothermal systems and implications for epithermal ore deposition. Economic Geology, 80, 1379–1406.

Hedenquist, J. W., Izawa, E., Arribas, A. Jr. and White, N. C. (1996) Epithermal gold deposits: styles, characteristics and exploration. Resource Geology, Special Publication Number 1.

Hennig, J., Hall, R. and Armstrong, R. A. (2016) U-Pb zircon geochronology of rocks from west Central Sulawesi, Indonesia: Extension-related metamorphism and magmatism during the early stages of mountain building. Gondwana Research, 32, 41–63.

Hoefs, J. (2015) Stable Isotope Geochemistry Seventh Edition. Springer, Germany, 387p.

Idrus, A., Safruddim and Titisari, A. D. (2015) Ore mineralization, alteration and mineralizing hydrothermal fluid characteristics of the Awak Mas mesothermal gold deposit, South Sulawesi, Indonesia. Proceeding of 8th Seminar Nasional Kebumian, Academia-Industry Linkage, 434-446.

Idrus, A., Sufriadin and Nur, I. (2011) Hydrothermal ore mineralization in Sulawesi: A view point of tectonic setting and metallogenesis. Proceeding Joint Convention Makassar 2011, The 36th Himpunan Ahli Geofisika Indonesia and the 40th Ikatan Ahli Geologi Indonesia Annual Convention and Exhibition.

Idrus, A., Warmada, I. W., Nur, J., Sufriadin, Imai, A., Widasaputra, S., Marlia, S. I., Fadlin, Kamrullah (2010) Metamorphic rock-hosted orogenic gold deposits type as a source of Langkowala placer gold, Bombana, Southeast Sulawesi, Indonesia. Proceedings PIT IAGI Lombok 2010.

Jaya, A. and Nishikawa, O. (2013) Paleostress reconstruction from calcite twin and fault-slip data using the multiple inverse method in the East Walanae fault zone: Implications for the Neogene contraction in South Sulawesi, Indonesia. Journal of Structural Geology, 55, 34-49.

Jensen, E. P. and Barton, M. D. (2000) Gold deposits related to alkaline magmatism. Reviews in Economic Geology, 13, 210–314.

John, D. A., Hofstra, A. H., Fleck, R. J., Brummer, J. E. and Saderholm, E. C. (2003) Geologic setting and genesis of the Mule Canyon low-sulfidation epithermal gold–silver deposit, north-central Nevada. Economic Geology, 98, 425–464.

Katili, J. A. (1978) Past and present geotectonic position of Sulawesi, Indonesia. Tectonophysics, 45, 289-322.

Kavalieris, I., Van Leeuwen, Th. M. and Wilson, M. (1992) Geological setting and styles of mineralization, north arm of Sulawesi, Indonesia. Journal of Souteast Asian Earth Sciences, 7, 113-129.

Kerrich R. and Fyfe W.S. (1981) The gold-carbonate association: Source of CO_2 and CO fixation reactions in Archaean lode deposits. Chemical Geology, 33, 265–294.

Kusnadi, D. and Setiawan, D. L. (2009) Penyelidikan geokimia daerah panas bumi Bittuang Kabupaten Tana Toraja, Provinsi Sulawesi Selatan. Prosiding Hasil Kegiatan Lapangan Pusat Sumber Daya Geologi, 171-187.

Liu, J. Z., Deng, Y. M., Liu, C. Q., Zhang, X. C. and Xia, Y. (2006) Metallogenic conditions and model of the superlarge Shuiyindong stratabound Au deposit in Zhenfeng County, Guizhou Province. Geology in China, 33,169–177 (in Chinese with English abs.).

Maulana, A., Imai, A., van Leeuwen, T., Watanabe, K., Yonezu, K., Nakano, T., Boyce, A., Page, L. and Schersten, A. (2016) Origin and geodynamic setting of Late Cenozoic granitoids in Sulawesi, Indonesia. Journal of Asian Earth Sciences, 124, 102-125.

McLennan, S. M. (1989) Rare earth elements in sedimentary rocks: influence of provenance and sedimentary process. In: Lipin, B. R. and McKay, G. A. (eds), Geochemistry and mineralogy of rare earth elements. Reviews in Mineralogy, 21, 169-200.

Metcalfe, I. (2011) Paleozoic – Mesozoic history of SE Asia, *in*: Hall, R., Cottam, M. A. and Wilson, M. E. J. (eds.) The SE Asian Gateway: History and Tectonics of the Australia-Asia Collision. The Geological Society of London, Special Publication, 355, 7-36.

Neall, F. B. and Phillips, G. N. (1987) Fluid-wallrock interaction around Archean hydrothermal gold deposits: a thermodynamic model. Economic Geology, 82, 1679-1694.

Nesbitt, B. E., Murowchick, J. B,, and Muehlenbachs, K. (1986) Dual origins of lode gold deposits in the Canadian Cordillera. Geology, 14, 506–509.

Phillips, G. N. and Groves, D. I. (1984) Fluid access and fluid-wallrock interaction in the genesis of the Archaean gold-quartz vein deposit at Hunt mine, Kambalda, Western Australia *in*: Foster, R. P. (eds.) Gold 82: The Geology, Geochemistry and Genesis of Gold Deposits. Balkema, Rotterdam, 389-416.

Phillips, G. N. and Powell, R. (2010) Formation of gold deposits: A metamorphic devolatilization model. Journal of Metamorphic Geology, 28, 689-718.

Pollard, P. J. (1983) Magmatic and post-magmatic processes in the formation of rocks associated with rare element deposits. Trans Inst Min Metall, 92, B1-B9

Priadi, B., Polve, M., Maury, R. C., Bellon, H., Soeria-Atmadja, R., Joron, J. L. and Cotten, J. (1994) Tertiary and Quaternary magmatism in Central Sulawesi: Chronological and petrological constraints. Journal of Southeast Asian Earth Sciences, 9, 81-93.

Querubin, C. D. and Walters, S. (2011) Geology and mineralization of Awak Mas: A sedimentary hosted gold deposit, South Sulawesi, Indonesia. Proceedings of The Sulawesi Mineral Resource, Masyarakat Geologi Ekonomi Indonesia – Ikatan Ahli Geologi Indonesia, 211-222.

Reed, M. H. (1997) Hydrothermal alteration and its relationship to ore fluid composition, *in*: Barnes, H. L. (eds.) Geochemistry of Hydrothermal Ore Deposits, 3rd ed. John Wiley & Son, USA, 303-365.

Ridley, J. R. and Diamond, L. W. (2000) Fluid chemistry of orogenic lode gold deposits and implications for genetic models. Reviews in Economic Geology, 13, 141–162.

Riogilang, H., Itoi, R. and Taguchi, S. (2012) Origin of hot spring water in the Kotamobagu geothermal field, Northern Sulawesi, Indonesia. Journal of the Geothermal Research Society of Japan, 34, 151-159.

Robb, L. (2005) Introduction to Ore-forming Process. Blackwell, United Kingdom, 373p.

Roedder, E. (1984) Fluid Inclusions. Reviews in Mineralogy, 12, 644p.

Rosso, K. M. and Bodnar, R. J. (1995) Microthermometric and Raman spectroscopic detection limits of CO_2 in fluid inclusions and the Raman spectroscopic characterization of CO_2. Geochimica et Cosmochimica Acta, 59, 3961-3975.

Saunders, J. A., Hofstra, A. H., Goldfarb, R. J. and Reed, M. H. (2014) Geochemistry of hydrothermal gold deposits. Treatise on Geochemistry 2nd Edition, Elsevier, 383-424.

Saunders, A. D. and Tarney, J. (1984) Geochemical characteristics of basaltic volcanism within back-arc basin *in*: Kokelaar, B. P. and Howells, M. F. (eds.) Marginal Basin Geology. Geological Society of London Special Publication 16, 59-76.

Seaward, T. M., Williams-Jones, A. E. and Migdisov, A. A. (2014) The chemistry of metal transport and deposition by ore-forming hydrothermal fluids. Treatise on Geochemistry 2nd Edition, Elsevier, 29-57.

Simmons, S. F., White, N. C. and John, D. A. (2005) Geological characteristics of epithermal precious and base metal deposits. Economic Geology, 100th Anniversary Volume, 485-522.

Smillie, R. W. (1996) Geological Overview of the Awak Mas Gold Deposit, South Sulawesi, Unpubl, 19p.

Sun, S. S. (1980) Lead isotopic study of young volcanic rocks from mid-ocean ridges, ocean island and island arcs. Philosophical Transactions Mathematical Physical & Engineering Sciences, 297, 409-445.

Sun, S. S. and McDonough, W. F. (1982) Chemical and isotopic systematics of eceanic basalt: Implications for mantle composition and processes *in*: Saunders, A. D. and Norry, M. J. (eds.) Magmatism in Ocean Basins. Geological Society of London Special Publication, 42, 313-345.

Susilo, J. (1998) Metamorfosa Pada Komplek Latimojong, Sulawesi Selatan dan Makna Tektoniknya, ITB, master thesis, Unpubl, 85p.

Taylor, Jr. H. P. (1974) The application of oxygen and hydrogen isotope studies to problems of hydrothermal alteration and ore deposition. Economic Geology, 69, 843-883.

Tetra Tech (2013) Salu Bulo Gold Project Sulawesi, Indonesia. Technical Report, Prepared for One Asia Resources Limited, Unpubl, 104p.

Van Leeuwen, T. M. (2018) Twenty Five More Years of Mineral Exploration and Discovery in Indonesia. Masyarakat Geologi Ekonomi Indonesia, 10th Anniversary Special Publication, 319p.

Van Leeuwen, T. M. and Pieters, P. E. (2011) Mineral deposits of Sulawesi. Proceedings of the Sulawesi Mineral Resource, Masyarakat Geologi Ekonomi Indonesia – Ikatan Ahli Geologi Indonesia, 1-110.

Wajdi, M. F., Santoso, S. B., Kusumanto, D. and Digdowirogo, S. (2011) Metamorphic hosted low sulphidation epithermal gold system at Poboya, Central Sulawesi: A general descriptive review. Proceedings of the Sulawesi Mineral Resource, Masyarakat Geologi Ekonomi Indonesia – Ikatan Ahli Geologi Indonesia, 201-210.

White, P. (1999) Petrology Report on 21 Samples From Awak Mas for PT Masmindo Dwi Area, Kingston Morrison, Unpubl, 40p.

White, L. T., Hall, R., Armstrong, R. A., Barber, A. J., Fadel, M. B., Baxter, A., Wakita, K., Manning, C. and Soesilo, J. (2017) The geological history of the Latimojong region of western Sulawesi, Indonesia. Journal of Asian Earth Sciences, 138, 72-91.

Wilkinson, J. J. (2001) Fluid inclusions in hydrothermal ore deposits. Lithos, 55, 229-272.

Yamamoto, J. and Kagi, H. (2006) Extended micro-Raman densimeter for CO_2 applicable to mantle-originated fluid inclusions. Chemistry Letters, 35, 610-611.

Yanagisawa, F. and Sakai, H. (1983) Thermal decomposition of barium sulfate-vanadium pentaoxide-silica glass mixtures for preparation of sulfur dioxide in sulfur isotope ratio measurements. Anal. Chem., 55, 985-987.

Zaccarini, F. and Garuti, G. (2008) Mineralogy and chemical composition of VMS deposits of northern Apennie ophiolites, Italy: evidence for the influence of country rock type on ore composition. Mineralogy and Petrology, 94, 61-83.

APPENDICES

Appendix 1: Sampling location maps.

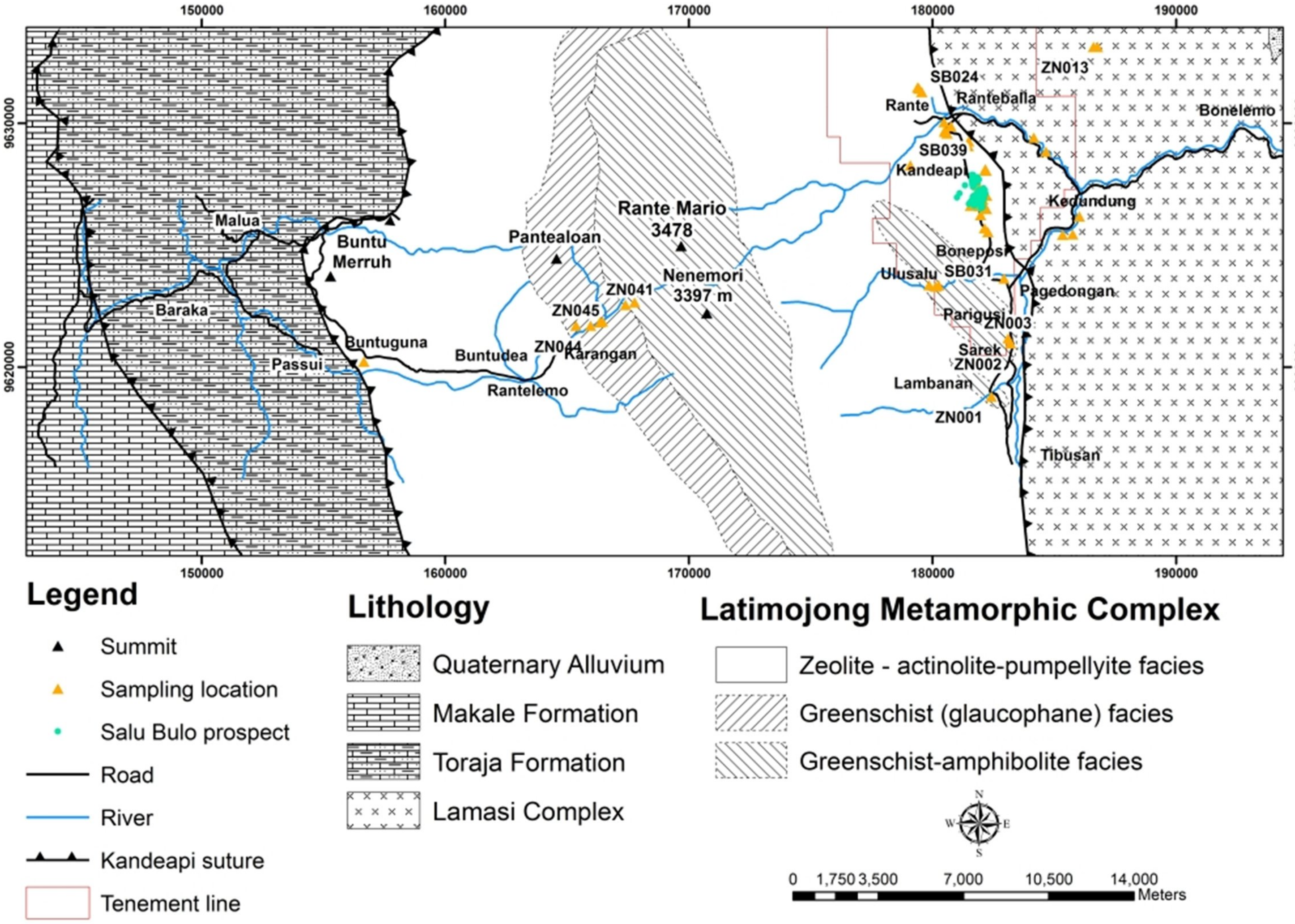

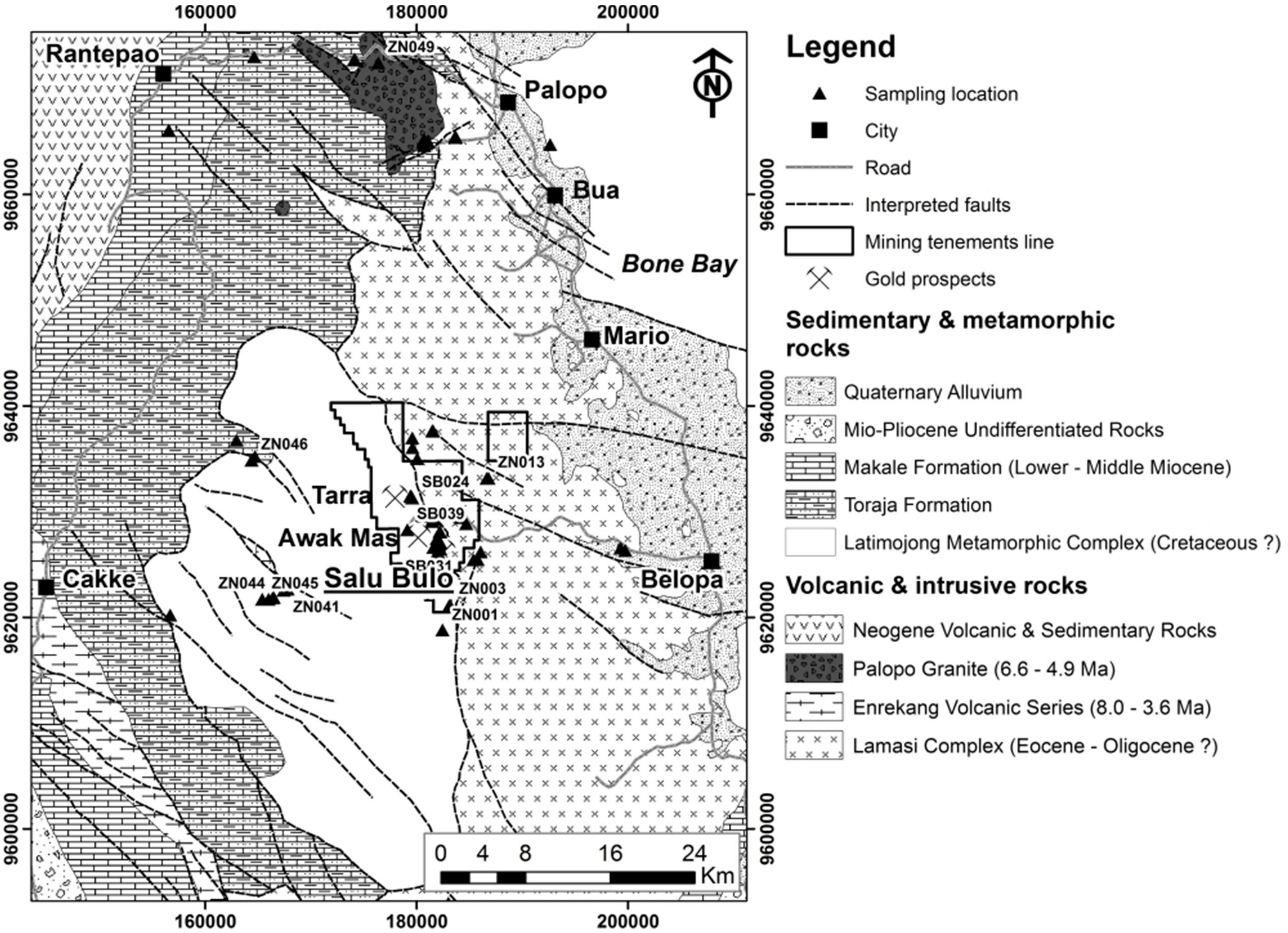
160000
180000
200000
9660000
9640000
9620000
9600000
Rantepao
ZN049
Palopo
Bua
Bone Bay
Mario
N
ZN046
ZN013
SB024
Tarra
SB039
Awak Mas
SB031
Salu Bulo
ZN003
ZN001
ZN044
ZN045
ZN041
Cakke
Belopa
0 4 8 16 24 Km
Legend
Sampling location
City
Road
Interpreted faults
Mining tenements line
Gold prospects
Sedimentary & metamorphic rocks
Quaternary Alluvium
Mio-Pliocene Undifferentiated Rocks
Makale Formation (Lower - Middle Miocene)
Toraja Formation
Latimojong Metamorphic Complex (Cretaceous ?)
Volcanic & intrusive rocks
Neogene Volcanic & Sedimentary Rocks
Palopo Granite (6.6 - 4.9 Ma)
Enrekang Volcanic Series (8.0 - 3.6 Ma)
Lamasi Complex (Eocene - Oligocene ?)

Appendix 2: Drill core sample list and megascopic description.

No.	Drill hole code	Depth (m)	Au (g/t)	Sample code	Description
1	**SBD069**	22.05-22.15	1.160	01	Meta-(hematitic) mudstone, qz-pl±cb vein parallel to foliation, pre-existing vein react with HCl, it cut foliation and veinlet, no occurrence of py.
2		23.43-23.50	8.940	02	Meta-(hematitic) mudstone, py fills foliation and disseminated, veinlet and folded qz-cb, qz-pl±cb cut foliation.
3		25.16-25.28	7.460	03	Meta-(hematitic) mudstone, stockworks or initial brecciation, py, qz-pl vein fills foliation as well in thin layer and cut foliation, qtz-car vein parallel to foliation.
4		25.28-25.40	7.460	04	Meta-(hematitic) mudstone, qz-pl-cb parallel to foliation, py parallel to foliation and disseminated, py in boundary between vein and host rock is abundant.
5		25.80-25.87	4.200	05	graphitic mudstone, qz±cb vein parallel to foliation, boudiaged and folded, pyrite, alteration halo along vein.
6		27.05-27.12	0.940	06	sheared rock, early vein boudinage, dissolved py sheared fill foliation in boundary between host rocks and ore.
7		38.00-38.06	4.970	07	Albitization, qz-cb vein, black mineral?, breccia (re-activation), py (?), vein fill space when breacciation or early vein breccia.
8		39.05-39.20	6.000	08	Meta-(hematitic) mudstone, albitization, brecciated, qz-cb-pl, py disseminated and fills foliation.
9		46.78-46.83	2.900	09	Meta-siltstone, qz-cb-pl vein cut and parallel to foliation, low py occurrences, albitization spotted close to vein.
10		51.05-51.20	7.410	10	Meta-(graphitic) mudstone, qz-cb vein, py at altered host rock, vuggy vein (as late vein or indicator of open space).
11		52.06-52.10	16.000	11	Altered host rocks, multistage brecciation, qz-cb vein.
12		53.60-53.70	14.000	12	Altered host rocks, multistage brecciation, qz-cb vein cut foliation.
13		54.08-54.17	13.000	13	Intense alteration, py disseminated, black vein as late vein.
14		54.65-54.85	13.000	14	Intense alteration, fragment of host rock, qz-cb vein, py.
15		57.07-57.17	0.880	16	Barren qz vein.
16		63.54-63.62	<0.01	17	Meta-volcaniclastic, shearing process, no alteration, no py visible.
17		64.50-64.55	3.450	18	Intense alteration, qz-cb vein cut foliation, py occurrences, vuggy texture.

18		64.62-64.72	3.450	19	Meta-volcaniclastic or -(chloritic) mudstone, become fragment, py, v.ii, albitized.
19	**SBD053**	13.30-13.35	<0.01	01	Basalt/meta-volcanic clastic, no py, no vein, vuggy and qz vein, no albitized.
20		38.45-38.50	<0.01	02	Meta-volcaniclastic, alterated to chlorite, no vein, no albitized, fault breccia.
21		68.13-68.20	0.030	03	Meta-volcanic, chloritic, low py, no vein, no albitized.
22		80.10-80.20	4.790	04	Breaccia ore of v.ii, v.ii as fragment or plagioclase growth, py disseminated in large size, albitized.
23		80.25-80.32	4.790	05	Breaccia ore of v.ii, v.ii as fragment or plagioclase growth, py disseminated in large size, albitized, dark vein.
24		86.40-86.62	3.300	06	Intense alteration, albitized, v.i, composition of black vein, cut v.i, host rock composition.
25		95.65-95.80	6.540	07	Alteration-breccia, fragment composition, v.ii late, v.ii as fragment as well, py diss and agregate.
26		97.20-97.32	1.230	08	Alteration, vein formation, vein composition, v.ii, py, fragment composition, low py contact.
27		102.50-102.67	6.440	09	Sandstone/basalt, albitized in boundary between vein and hostrock, py diss in alterated host rock, vuggy (composition) of v.ii or v.iii.
28		103.82-103.90	2.330	10	Alterated in boundary.
29		104.75-104.80	2.330	11	Meta-(graphitic) mudstone, py in foliation, stock and of py, albitized, brx of v.ii, py diss in v.ii.
30		105.80-105.90	0.900	12	Meta-volcaniclastic, early vein parallel to foliation, v.ii cut foliation, shear sense, and composition, host rocks, low py and albitized.
31		108.80-108.93	0.030	13	Breccia ore of v.ii, high albitized of fragment, py disseminated, v.ii as fragment as well, high albitized.
32	**SBD019**	37.30-37.40	2.370	01	Stockwork of v.ii, diss py, albitized, vuggy.
33		47.80-48.00	4.260	02	v.ii, stockwork v.ii, vein formation, v.ii become fragment (boudin), late vein, py diss.
34		51.10-51.20	12.300	03	High albitized, host rock as fragment, v.ii as fragment, py disseminated, breccia ore.
35		62.60-62.80	1.180	04	Meta-volcanic (?), albitized, py diss and aggregate, v.ii stockwork, vuggy.
36		67.40-67.58	0.560	05	Breccia ore, silicified, why different with mineralized brx, vein composition-SB001, rock fragment (?) low albitized, vuggy
37		68.00-68.10	0.370	06	v.ii breccia, stockwork, diss py, veinlet in host rock.

38		72.70-72.82	0.500	07	Meta-volcanic/sandstone?, no py, low albitized, chloritic, v.ii/v.iii in dilational jog or open space.
39		74.92-75.00	1.470	08	Meta-volcanic, v.ii paralle and cut foliation, silicified, py disseminated, albitized, cut by carbonate vein.
40		79.14-79.22	1.950	09	Brecccia ore of v.ii, v.ii as fragment, matrix in high alterated host rock, diss py, high albitized, meta-volcanic clastic.
41		86.90-87.00	1.770	10	silicified, sheared rock/meta-volacnic, low diss py, v.ii cut foliation.
42		87.70-87.75	1.770	11	Folded early vein, v.ii cut early vein, shear sense, if early py exist in foliation plane.
43		107.28-107.37	0.680	12	Barren vuggy vein, py in rare, clay mineral in porous (?).
44	**SBD105**	20.00-20.08	0.090	01	Clay alteration, sheared zone, v.i barren, no py visible.
45		21.30-21.43	0.090	03	Least silicified, clay alteration, sheared zone, diss fine-grained py, wigglet iron layer, v.ii (?).
46		22.40-22.50	1.690	04	Silicified, breccia ore of v.ii, no visible py, sandstone/ hematitic mudstone.
47		24.42-24.50	0.005	05	Meta-(hematitic) mudstone, folded v.i, stockwork, chloritic in vein, no py visible, low albitized.
48		30.60-30.70	0.005	06	Meta-(chloritic) mudstone, iron layer, no py visible, v.i irregular, no albitized.
49		56.35-56.50	0.005	07	Basalt/diorite, v.i albite (?), no py, no albitized.
50		82.57-82.84	0.010	08	Clay alteration, sheared zone, folded, foliated, low py visible, iron layer folded, v.ii, D2.
51		90.67-90.90	3.370	09	Sandstone/basalt (?), breccia of v.ii, py diss in rare, vuggy, albitized of host rock.
52		94.00-94.25	0.280	10	Sandstone, albitized, breccia of v.ii, py diss is rare, vuggy, stockwork of v.ii.
53		104.19-104.20	0.005	11	Meta-volcanic, albitized, no py, stockwork of vein carbonate (v.i) (?).
54	**SBD109**	40.60-40.70	2.870	01	Py stringer.
55		40.80-40.87	2.870	02	Meta-(hematitic) mudstone, v.ii //, vein carbonate cut foliation and irregular, no py visible, no rock albitized.
56		48.15-48.25	2.310	03	Meta-(hematitic) mudstone, stockwork v.ii, low albitized, no py visible.
57		66.15-66.24	1.750	06	Meta-(hematitic) mudstone, albitized, breccia of v.ii, py disse aggregate in in hematitic mudstone.
58		66.33-66.45	1.750	07	Meta-(hematitic) mudstone, laminated v.i parallel to foliation, no py visible, low albitized.

59	**SBD006**	11.75-11.88		01	Quartz vein with vuggy texture, similar with outcrop vein.
60		16.40-16.50		02	Meta-(graphitic) mudstone, v.i, py, albitized (?), vein formation, carbonate vein fill foliation, boudinage.
61		20.15-20.25	5.440	03	Meta-volcanic clastic, vein, breccia with disseminated py.
62		46.00-48.00	3.360	04	Sandstone/arenite, silicified/albitized, disseminated py, low foliated, py cubic.
63		52.20-52.15	1.030	05	Meta-(chloritic) volcanic (?), discordant ore body (silicified/albitized withh disseminated py, cut by early boudinage (?) vein.
64		56.50-56.60	2.190	06	Boudin of sandstone (early vein), shear zone, silica vein cut foliation/cleavage, matrix in albitized and disseminated py.
65		56.92-56.97	2.190	07	Sillicified, sandstone, breccia network and vuggy vein, disseminated fine-grained py.
66		57.60-57.70	2.190	08	Breccia ore, albitized, v.ii, pyrite, multistage brecciation.
67		59.23-59.30	3.130	09	Breccia ore, no albitized (sandstone)/volcanicclastic, breaccia fragment.
68		61.00-61.10	5.740	10	silicified, sandstone, vein breccia cut foliation, vein form breccia, fill fracture surrounding, qtz became vein as fragment,
69		62.80-62.90	2.290	11	Breccia ore, v.iii, alteration, silicified, sandstone, vuggy/open fracture/vein.
70		63.28-63.42	2.290	12	Breccia ore, open space represent brittle deformation, variation of alteration grade of fragment, disseminated fine-grained py.
71		63.55-63.60	2.290	13	Breccia (ore), high albitized, foliated fragment, early carbonate vein become fragment, open space.
72		66.00-66.10		14	Silicified, sandstone, folded, fill by folded qtz vein, cut by brx vein, diss fine-grained py.
73		66.75-66.85	2.080	15	(Graphitic) phyllite, disseminated py fill foliation (boudin), other sulfide, cut by qtz-car-plag vein.
74		67.50-67.60	2.080	16	Graphitic-chlorite phyllite, meta qtz, py diss fill foliation, cut by qtz-plag-carb, albitized/silicified.
75		72.70-72.90	0.190	17	(Graphitic) phyllite, early vein (meta qtz vein ?) folded, cut/fill by carbonate-qtz vein with py, and cut by silica vein late.
76		93.35-93.40	2.660	18	Meta-(chloritic) mudstone, disseminated minor pyrite.
77		93.70-94.00	2.660	19	Meta-(chloritic) mudstone, disseminated minor py, cut by qtz-plag-carbonate (?), early vein (boudin)/meta quartz.
78		103.95-104.00	0.840	20	Graphitic-chloritic phyllite, open fracture parallel to foliation fill by silica, diss fine-grained py.

79		104.15-104.20	0.920	21	Graphitic-chloritic phyllite (siltstone), qtz vein fill foliation, some folded and boudinage, minor disseminated py.
80		104.80-104.95	0.920	22	Silicified/albitized, siltstone/sandstone, diss py, qtz-plag-car (?) fill foliation, folded, with vuggy, late (qtz) visible cut foliation.
81	**SBD008**	29.15-29.30	2.250	01	Basalt/fine-grained sandstone, vein/breccia ore, plag-qtz-car, slightly silicified HR, sisseminated cubic pyrite, vuggy vein.
82		34.10-34.20	3.370	02	Basalt/ fine-grained sandstone, veinlet of qtz-carb in marginal part, low pyrite concentration.
83		45.62-45.78	3.300	03	Breccia ore, disseminated pyrite and aggregate, late vein (qtz).
84		53.40-53.45	3.600	04	Vein parallelto foliation, pyrite parallel to foliation, silicified/albitized, cut by qz vein.
85		57.10-57.25	1.530	05	Breccia ore, qz-pl-cb vein, high albitization of fragment, disseminated py in fragment, plagioclase (?) vein.
86		60.23-60.40	3.680	06	Sandstone, silicified, breccia, filled by qtz-plag (?)-car, disseminated minor py.
87		60.73-60.90	3.680	07	Vein composition + stage, why not albitized, silicified, siltstone (?), qtz-plag-car brx diss py.
88		65.30-65.35	1.240	08	diss cubic py folded.
89		65.35-65.42	1.240		Breccia, qz-pl-cb, folded.
90		65.42-65.48	1.240	09	Early vein (?), folded, diss py, py stringer.
91		65.56-65.62	1.240	11	Meta-(chloritic) mudstone/volcanic.
92	**SBD009**	32.00-32.15	1.530	01	Meta-(graphitic) mudstone, albitized/silicified, breccia ore, qz-cb (?)-plag fill foliation, red trace, diss fine-grained py.
93		47.50-47.60	4.330	02	Breccia or of v.ii, vein formation and composition, diss fine-grained py.
94		48.85-48.95	3.180	03	fFne-grained sandstone, cut by v.ii vein cut foliation, diss fine-grained py, boudin (?), v.i, v.ii vuggy/comb.
95		54.02-54.45	2.740	04	Fine-grained sadstone, breccia ore, qtz-plag-car, composition, vuggy (open space), diss fine-grained py.
96		54.35-54.45	2.740	05	Fine-grained sandstone, diss py, qtz-plag-car cut foliation, open/vuggy v.ii.
97	**SBD072**	8.80-9.00	4.560	01	Sandstone, low-high silicified/albitized, v.ii parallel to foliation and stockwork in edge, aggregate sulfides.
98		9.60-9.70	0.780	02	Fine-grained sandstone, chloritic, silicified, low brecciated, diss low py.
99		14.10-14.15	6.220	03	Oxidized, diss cubic py, v.ii fill foliation, meta-(hematitic) mudstone.

100		17.00-17.10	0.100	04	Meta-(chloritic) mudstone/fine-grained sandstone, quartz vein in irregular, diss low py, low silicification/albitization close to v.ii.
101		24.70-24.80	1.730	05	Meta-(hematitic) mudstone, pores caused by release of clay minerals (?).
102		31.77-31.85	0.005	06	Fine-grained sandstone/mudstone, chlorite, v.iii/I carbonate, irregular.
103		68.30-68.35	1.270	07	Meta-(chloritic) mudstone/sandstone, qz-pl-cb vein cut host rock, diss py in marginal part, pores vein.
104		72.15-72.50	0.005	08	Sandstone, rock composition, no silicified/albitized, no py, veinlet carbonate.
105		72.80-73.05	12.500	09	Albitized, diss/stringer of py, porous vein, qtz-plag-car, v.ii.
106		75.75-75.90	1.380	10	Vein formation, why not albitized, vein growth, v.i cut by v.ii (vuggy), chloritic sandstone/mudstone.
107		87.15-87.23	0.200	11	Meta-(chloritic) sandstone/mudstone, carbonate vein cut rock, no py visible.
108		89.20-89.30	1.860	12	Vuggy texture.
109		103.15-103.20	1.370	15	Quartz vein, vuggy/comb, porous, py disseminated.
110	**SBD047**	21.30-21.40	0.020	01	Meta-(hematitic) mudstone (carbonatan), v.i folded in veinlet carbonate.
111		74.00-74.25	4.130	02	Meta-(hematitic) mudstone, v.ii // foliation, clay alteration (?).
112		78.80-78.90	1.770	03	Intense alteration, multistage breccia, inside alteration, v.ii.
113		79.18-79.28	1.770	04	Meta-siltstone (?), albitized, v.ii cut and parallel to foliation, py disseminated, initial to stockwork and breccia.
114		82.50-82.65	<0.01	05	Sheared rock, v.i folded anaf boudinage, vein composition, shear sense, py (if available).
115		84.30-84.40	0.420	06	Meta-(graphitic) mudstone (?), albitized, v.ii, vein composition, cross cutting relationship.
116		85.95-86.00	0.130	07	Breccia ore, low grade, v.ii (?).
117		99.05-99.15	0.020	08	Meta-volcaniclastic, v.iii carbonate parallel to foliation and irregular, vein composition, hostrock composition.
118		100.50-100.60	9.160	09	Breccia ore, v.ii, chlorite (?), py, vein formation, high albitized.
119		104.42-104.52	3.380	10	Albitized, vein formation, diss py, v.ii, sandstone.
120		106.70-106.80	2.290	11	Meta-volacaniclastic/(chloritic) mudstone, albitized, v.ii cut and // foliation, pyrite disseminated.
121		111.75-111.85	6.230	12	Albitized, v.ii, sandstone, py disseminated.

122	**SBD102**	35.27-35.40	0.005	01	Breccia ore, fragment of hematitic mudstone/sandstone, filled by vein carbonate.
123		46.15-46.20	0.005	02	Barren vein.
124		50.70-50.85	1.280	04	Meta-(chloritic) sandstone, v.ii stockwork and py, weak-mod albitized, contact with sheared rock, v.ii parallel to foliation and boudinage.
125		51.00-51.15	4.180	05	Breccia, hematitic mudstone, v.ii, multistage vein/breccia, py disseminated, albitized.
126		53.75-53.85	0.005	07	Basalt, chloritic, no alteration, low py, cut by carbonate vein.
127		78.07-78.20	2.110	08	Stockwork, breccia of v.ii, sandstone, moderatelly albitized, pyrite band, vuggy texture.
128	**SBD121**	19.20-19.33	0.255	01	Meta-(hematitic) mudstone, low albitized, v.i/v.iii cut foliation and irregular, no much py visible, transisi between host rock and ore.
129		37.20-37.30	3.240	03	Meta-(hematitic) mudstone, weak sheared & albitized, cut breccia v.ii, no py visible.
130		38.50-38.65	0.370	04	Meta-(hematitic) mudstone, albitized and sheared, v.i carbonate, v.ii plagioclase, v.i // foliation and folded, no py visible.
131		90.95-91.20	0.500	05	Meta-(hematitc) mudstone, no albitized, v.i carbonate, // foliation and stockwork, no py visible.
132		93.25-93.40	1.830	06	Meta-(hematitic) mudstone, alteration close to v.oo cut foliation, no py visible.
133	**SBD086**	7.15-7.30	3.560	01	Meta-(hematitic) and -(chloritic) mudstone, breccia of v.ii, irregular carbonate vein, no py visible.
134		9.20-9.30	1.750	02	Meta-(hematitic) and -(chloritic) mudstone, no alteration, no visible py, stockwork carbonate vein.
135		38.15-38.30	0.370	03	Contact of meta-(hematitic) mudstone and -(hematitic) sandstone (basalt), no alteration, no py visible, irregular vein carbonate.
136		40.30-40.50	0.820	04	Basalt/hematitic sandstone, no alteration, no py visible, no foliation, v.ii vuggy (?), carbonate vein (?).
137		42.42-42.50	0.005	05	Contact of meta-(hematitic) mudstone and sandstone, no alteration, no py visible, v.ii parallel to foliation, boudin (v.ii).
138	**SBD082**	21.10-21.20	4.240	01	Oxidized, hematitic mudstone, albitized, v.ii cut and parallel to foliation, py is oxidized, no py visible.
139		21.83-21.90	4.240	02	Milky vein.
140		24.30-24.38	6.730	04	Qz-pl-cb vein, diss py, albitized/silicified, high alterated of fragment.

141		26.65-26.75	0.005	05	Chloritic sandstone, no alteration/silicified, no py visible, v.iii carbonate at v.ii.
142		36.80-36.90	1.075	06	Contact of meta-(hematitic) mudstone and -volacanic, v.i (?) parallel and cut foliation, in dilational jog, v.ii in boudinage (?), fine-grained py.
143		45.90-45.95	0.005	08	Hematitic, v.i carbonate folded anf // foliation, vein composition and formation, v.ii cut v.i.
144	**SBD132**	58.20-58.30	0.005	02	Basalt/sandstone, no silicification/albitized, no py, qtz vein vein irregular.
145		59.20-59.25	1.300	03	Basalt/sandstone, fine diss py, v.ii, irregular/stockwork, silicified, close to vein.
146		60.45-60.55	0.910	04	Basalt/sandstone, stockwork, silicified close to vein, v.ii.
147		62.10-62.20	2.970	05	Silicified, sandstone, fine diss py, v.ii stockwork.
148		64.15-64.40	3.000	06	sandstone/basalt, silicified/albitized, qtz-plag-car, breccia, py diss.
149		65.07-65.20	3.180	07	Breccia, qz-cb, v.ii as brx fragment, diss py, sandstone/basalt.
150		77.10-77.18	7.890	08	Breccia (multistage), low albitized of host rock, vein as breccia fragment (?), why no albitized.
151		77.18-77.28	7.890	09	Breccia (multistage), low albitized of host rock, vein as breccia fragment (?), qz-pl-cb (vuggy/porous).
152		78.40-78.50	0.015	10	Basalt/sandstone, fresh rock, low sil/albite parallel qtz-car vein in vuggy low foliation, small diss py.
153	**SBD044**	35.00-35.10	4.300	01	hematitic mudstone, laminated vein, v.ii // change to plag or car (?), py in hematitic mudstone, vein composition, 1 & 2 brx v.ii as fragment
154		35.30-35.40	4.300	02	Meta-(hematitic) mudstone (phyllite).
155		35.77-35.95	2.820	03	Breccia, meta-(hematitic) mudstone, qz-pl-cb vein (?), vuggy, diss py, in fragment and minor in matrix.
156		40.15-40.20	0.320	04	Silicified, chloritic sandstone/meta-volcanic clastic, v.ii as vein.
157		42.90-43.03	9.970	05	Euhedral py in fragment, late py in matrix and vein qz-pl-cb vein.
158		45.00-45.20	35.370	06	Meta-(hematitic) mudstone, laminated vein, alteration of qz-pl-cb vein, py diss and stringer.
159		45.20-45.40	35.370	07	Meta-(hematitic) mudstone, boudin of previous vein (D2), shear sense, pyrite, vein composition, sphalerite, aspy, galena.
160		55.30-55.35	8.790	08	Breccia ore, qz-pl-cb, porous/broken py, vuggy, v.ii as fragment or matrix.
161		120.10-120.20	<0.01	09	Oxidized py.

162	128.15-128.30	0.860	10	Vuggy texture of v.ii.
163	130.25-130.35	0.120	11	Meta-(chloritic) mudstone/phyllite, v.ii.
164	130.90-131.00	2.840	12	Intensely albitized/silicified, diss py, qtz-plag-car, foliation is preserved, v.ii cut foliation.

Appendix 3: Drill core and outcrop microscopic description.

No.	Sample code	Depth (m)	Analytical code	Lithology	Mineral assemblage	Alteration	Ore mineral	Vein composition
1	SB001-01	Surface		Massive quartz vein	Qz-Ab-LF	Sil	Py-Gn-Ten-Ccp	Qz±Ab vein (iii)
2	SB001-02	Surface		Massive quartz vein	Qz			Quartz vein (iii)
3	SB002-03	Surface	SB#16	Crackle breccia	Qz-Ank-Cal-Ab-Py	Sil	Py	Qz-Cal(±Ank)-Ab vein (iv)
4	SB011A-03	Surface		Milled breccia	Qz-Ank-Ab	Sil-Cab-Ab-Py	Py	Ank±Qz±Ab vein (ii); clast of Qz-Ank±Ab vein (i)
5	SB013-02B	Surface		Meta-(chloritic) mudstone	Qz-Cal-Pl-Ilt/Ms			Early Qz-Cal vein
6	SB014-01	Surface		Meta-volcaniclastic rock	Qz-Cal-Pl-Chl-Ilt-Prh/Pmp-Px-LF			Early Qz-Cal vein; Qz±Cal-Ab vein (iii)
7	SB014-02	Surface		Meta-(hematitic) mudstone/phyllite	Qz-Hem-Chl-Ilt/Ms-Ep		Py	
8	SB022	Surface		Diorite	Qz-Cal-Pl-Prh/pmp			
9	SB023	Surface		Diorite	Qz-Cal-Pl-Chl-Prh/Pmp-Ep-Px		Py	Late calcite vein
10	SB024	Surface		Diorite	Qz-Cal-Pl-Px			
11	SB031	Surface		Quartz Muscovite Schist	Qz-Ms			
12	SBD006-02	16.40-16.50	SB#23	Meta-(graphitic) mudstone	Qz-Pl-Gr-Ilt/Ms			Early Qz-Cal vein

13	SBD006-07	56.92-56.97	SB#07	Meta-sandstone	Qz-Cal-Ab-Pl-Chl?-Gr?-Rt	Sil-Ab	Py	
14	SBD006-08	57.60-57.70	SB#04	Meta-siltstone	Qz-Ank-Cal-Pl-Hem?		Py	
15	SBD006-09	59.23-59.30	SB#01	Meta-sandstone	Qz-Ank-Cal-Pl-Hem?-Gr-Rt		Py	
16	SBD006-15	66.75-66.85		Meta-(graphitic) mudstone/Phyllite	Qz-Ank-Cal-Ab-Gr-Prh/Pmp-Ilt/Ms-Py	Sil	Py	Qz-Cal(±Ank)-Ab vein (iv) cut by vein (v)
17	SBD006-16	67.50-67.60		Meta-(graphitic) mudstone/Phyllite	Qz-Ank-Cal-Ab-Gr	Sil-Ab-Py	Py-Gr	Ank±Qz±Ab vein (ii) cut by Qz-Cal(±Ank)-Ab vein (iv)
18	SBD006-19	93.70-94.00		Meta-(chloritic) mudstone/phyllite	Qz-Ank-Ab-Gr-Prh/Pmp		Py-Au-Ccp-Bn	Early Qz-Cal vein; Ank±Qz±Ab vein (ii); Qz±Cal-Ab vein (iii), Qz-Cal(±Ank)-Ab vein (iv)
19	SBD006-20	103.95-104.00		Meta-(chloritic) mudstone	Qz-Ank-Chl-Ilt-Py	Cab?	Py-Ccp-Ten-Tet	Early Qz-Cal vein
20	SBD008-03	45.62-45.78		Crackel breccia	Qz-Ank-Ab		Py	Qz-Ank±Ab vein (i)
21	SBD008-04	79.18-79.28		Phyllite	Qz-Ank-Cal-Ab-Pl-Gr-Ms-Hem	Cab	Py-Ten-Tet-Au-Ccp	Early Ank-Qz±Ab vein
22	SBD008-09	65.42-65.48	SB#08	Meta-(chloritic) mudstone	Qz-Chl-Ilt/Ms	Cab	Py	
23	SBD008-10	65.48-65.56	SB#09	Breccia	Qz-Ank	Sil	Py	
24	SBD008-12	65.62-65.85	SB#05	Meta-(chloritic) mudstone	Qz-Chl-Ilt/Ms		Py	
25	SBD009-04B	54.02-54.45		Meta-siltstone	Qz-Ank-Cal-Pl		Py	Early Ank-Qz±Ab vein

26	SBD019-02	47.80-48.00		Breccia	Qz-Cal			Microcrystaline Qz-Cal vein (v); clast of vein (ii)
27	SBD019-03	51.10-51.20	SB#10	Meta-mudstone/breccia?	Qz-Ank-Ab-Py	Cab	Py	Ank±Qz±Ab vein (ii); Qz±Cal-Ab vein (iii); Qz-Cal(±Ank)-Ab vein (iv)
28	SBD019-06	68.00-68.10	SB#20	Breccia	Qz-Ank-Ab-Rt	Cab-Ab-Py	Py	Ank±Qz±Ab vein (ii)
29	SBD019-11	87.70-87.75		Phyllite	Qz-Ank-Cal-Ab-Gr		Py	Early Ank-Qz±Ab vein cut by vein (iii) & (iv)
30	SBD044-04	40.15-40.20	SB#14	Meta-sandstone	Qz-Ank-Cal-Ab-Rt	Cab-Ser?	Py	Qz-Ank±Ab vein (i); Ank±Qz±Ab vein (ii)
31	SBD044-06A	45.00-45.20		Meta-(hematitic) mudstone/milled breccia	Qz-Ank-Ab-Hem-Py	Cah-Sil-Ab	Py	Early Ank-Qz±Ab vein?
32	SBD044-06B	45.00-45.20	SB#19	Meta-(hematitic) mudstone/breccia	Qz-Ank-Cal-Ab-Hem-Py		Py-Ccp-Au	
33	SBD044-08	55.30-55.35		Breccia	Qz-Ank	Cab-Sil	Py	Qz-Ank±Ab vein (i)
34	SBD044-10	128.15-128.30		Meta-mudstone/silicified	Qz-Ank-Ab	Sil	Py	
35	SBD044-12	130.90-131.00	SB#13	Altered rock/stockworking?	Qz-Ank-Ab-Py	Sil-Cab-Ab	Py	Early Ank-Qz±Ab vein; Qz-Ank±Ab vein (i); Ank±Qz±Ab vein (ii)
36	SBD044-13	148.17-148.27		Meta-(graphitic) mudstone	Qz-Cal-Pl-Gr-Ilt/Ms		Py-Ccp-Ten-Tet	Early Qz-Cal vein
37	SBD047-06	84.30-84.40		Meta-sandstone?	Qz-Ank-Ab-Pl-Ilt/Ms	Cb	Py	
38	SBD047-07	85.95-86.00	SB#12	Breccia	Qz-Cal-Ab?-Py	Sil		Microcrystaline Qz-Cal vein (v); clast of vein (ii) and (iii)

39	SBD047-08	99.05-99.15	SB#15	Meta-sandstone	Qz-Ank-Cal-Pl-LF-Chl	Cab		Ank±Qz±Ab vein (ii)
40	SBD047-09	100.50-100.60	SB#11	Meta-mudstone?/breccia	Qz-Ank-Ab-Py	Cab-Ab	Py	
41	SBD053-05	80.25-80.32		Breccia	Qz-Ank-Ab-Rt	Sil	Py	Ank±Qz±Ab vein (ii) cut by microcrystaline Qz-Cal vein (v)
42	SBD053-10	103.82-103.90		Meta-(chloritic) mudstone/breccia	Qz-Ank-Ab-Ms-Prh/Pmp-Ep-Py-Gr?	Sil-Cab-Ab	Py-Au	Early Ank-Qz±Ab vein; Ank±Qz±Ab vein (ii)
43	SBD053-11	104.75-104.80		Phyllite (breccia)	Qz-Ank-Ab-Hem-Py-Prh/pmp-Rt	Sil-Cab-Py	Py-Ten-Tet-Au-Ccp-Au	Early Ank-Qz±Ab vein cut by vein (i) & (iv)
44	SBD069-02	23.43-23.50		Meta-(hematitic) mudstone	Cal-Hem-Py	Qz-Ab	Py-Ccp-Au	Qz-Ank±Ab vein (i); Ank±Qz±Ab vein (ii); Qz±Cal-Ab vein (iii)
45	SBD069-06	27.05-27.12		Phyllite	Qz-Ank-Gr-Ilt/Ms	Sil		Qz-Cal vein with Rt
46	SBD069-14	54.65-54.85	SB#17	Milled breccia	Qz-Ank-Ab-Py-Rt	Sil-Cab-Py	Py-Ten-Tet-Rt-Au-Ccp	Qz-Ank±Ab vein (i)
47	SBD072-06	31.77-31.85		Meta-(chloritic) mudstone	Qz-Cal-Px-Rt			
48	SBD072-08	72.15-72.50	SB#22	Meta-sandstone	Qz-Cal-Chl-LF			
49	SBD072-09	72.80-73.05	SB#18	Meta-volcaniclastic rock/stockworking	Qz-Ank-Ab-Py	Cab-Ab-Sil	Py-Rt-Ccp-Ten-Tet-Bn-Cov-Cc	Qz-Ank±Ab vein (i); Ank±Qz±Ab vein (ii); Qz±Cal-Ab vein (iii)
50	SBD072-10A	75.75-75.90		Meta-mudstone	Qz-Ank-Cal-Ab-Ilt/Ms		Py	Qz±Cal-Ab vein (iii)

51	SBD072-10B	75.75-75.90		Meta-mudstone	Qz-Ank-Cal-Ab		Py	Qz-Cal(±Ank)-Ab vein (iv)
52	SBD072-13A	89.75-89.85		Meta-mudstone/phyllite	Qz-Ank-Ilt/Ms		Py	Qz±Cal-Ab vein (iii); Qz-Cal(±Ank)-Ab vein (iv)
53	SBD072-13B	89.75-89.85		Meta-mudstone/phyllite	Qz-Ank-Ilt/Ms		Py	Qz±Cal-Ab vein (iii); Qz-Cal(±Ank)-Ab vein (iv)
54	SBD072-15	103.15-103.20		Vein	Qz-Ank	Cab-Py	Py	Qz-Ank±Ab vein (i)
55	SBD082-03	24.05-24.15		Meta-(hematitic) mudstone	Qz-Ank-Hem-Py		Py-Ten-Tet-Ccp	Ank±Qz±Ab vein (ii)
56	SBD082-08	45.90-45.95		Meta-(hematitic) mudstone	Qz-Ank-Ab-Hem			
57	SBD086-02	9.20-9.30		Meta-basalt	Pl-Cal-Hem			Qz-Ank±Ab vein (i) with Rt cut by vein (ii)
58	SBD086-03	38.15-38.30	SB#03	Meta-basalt	Pl-Cal-Chl-Hem-Ms-Prh/Pmp	Cab		Ank±Qz±Ab vein (ii)
59	SBD086-03A	38.15-38.30	SB#21	Meta-(hematitic) mudstone	Qz-Ank-Cal-Hem			Early Qz-Cal vein cut by Calcite vein
60	SBD102-04	50.70-50.85		Meta-basalt	Qz-Ank-Ab-Pl			
61	SBD102-06	51.60-51.65		Basalt/breccia	Qz-Ank-Cal-Ab-Pl-Hem	Cab-Ab	Py-Ten-Tet-Au-Ccp-Rt-Au	Qz±Cal-Ab vein (iii)
62	SBD102-07	53.75-53.85		Meta-basalt	Pl-Cal-Chl-Ep-Prh/pmp	Cab		Qz-Ank±Ab vein (i)

63	SBD105-06	30.60-30.70		Meta-(chloritic) mudstone	Qz-Cal-Ilt-Prh/Pmp	Ser?		Qz-Ank±Ab vein (i)
64	SBD109-01	40.60-40.70		Phyllite	Qz-Ank-Ab	Sil	Py	Qz-Cal(±Ank)-Ab vein (iv) cut Ank±Qz±Ab vein (ii); Clast of Qz±Cal-Ab vein (iii)
65	SBD109-04	62.60-62.80		Phyllite	Qz-Ank-Cal-Ilt		Py	
66	SBD132-02	58.20-58.30	SB#06	Meta-volcaniclastic rock	Qz-Cal-Chl-Px-Py-LF			Late calcite vein
67	SBD132-04	60.45-60.55		Meta-(chloritic) mudstone	Qz-Ank-Cal-Ab-Chl-Ilt	Cab-Py	Py	Microcrystaline Qz-Cal vein (v); clast of vein (ii) and vein (iii)
68	SBD132-08	77.10-77.18		Milled breccia	Qz-Ank-Cal-Ab		Py	Clast of Qz-Ab vein
69	SBD132-10	78.40-78.50	SB#02	Meta-siltstone	Qz-Cal-Pl-Chl-Py		Py	Early Ank-Qz±Ab vein

Appendix 4: XRD analyses of ore and intensely altered host rocks.

1) SB003-02

Breccia ore consist of altered (silicification) meta-(chloritic) mudstone clast and matrix of quartz-carbonate-albite mineral that related to main stage vein (iv). Pyrite occurred as dissemination in altered breccia clast and rarely in matrix.

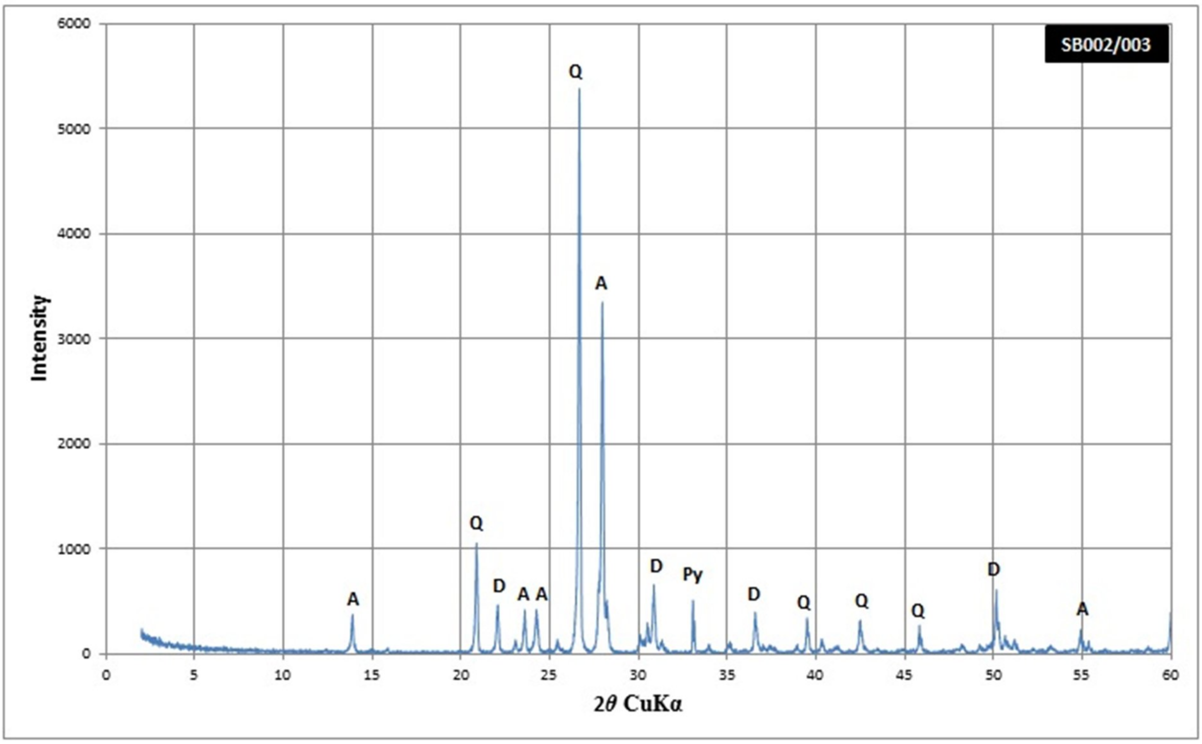

Abbreviation: A=albite; Q=quartz; An=ankerite; Py=pyrite; D=dolomite.

2) SBD044-06

Meta-(hematitic) mudstone host milled breccia (?). Pyrite is much in altered rock and often in host rock. Ankerite is dominant alteration along with quartz and albite.

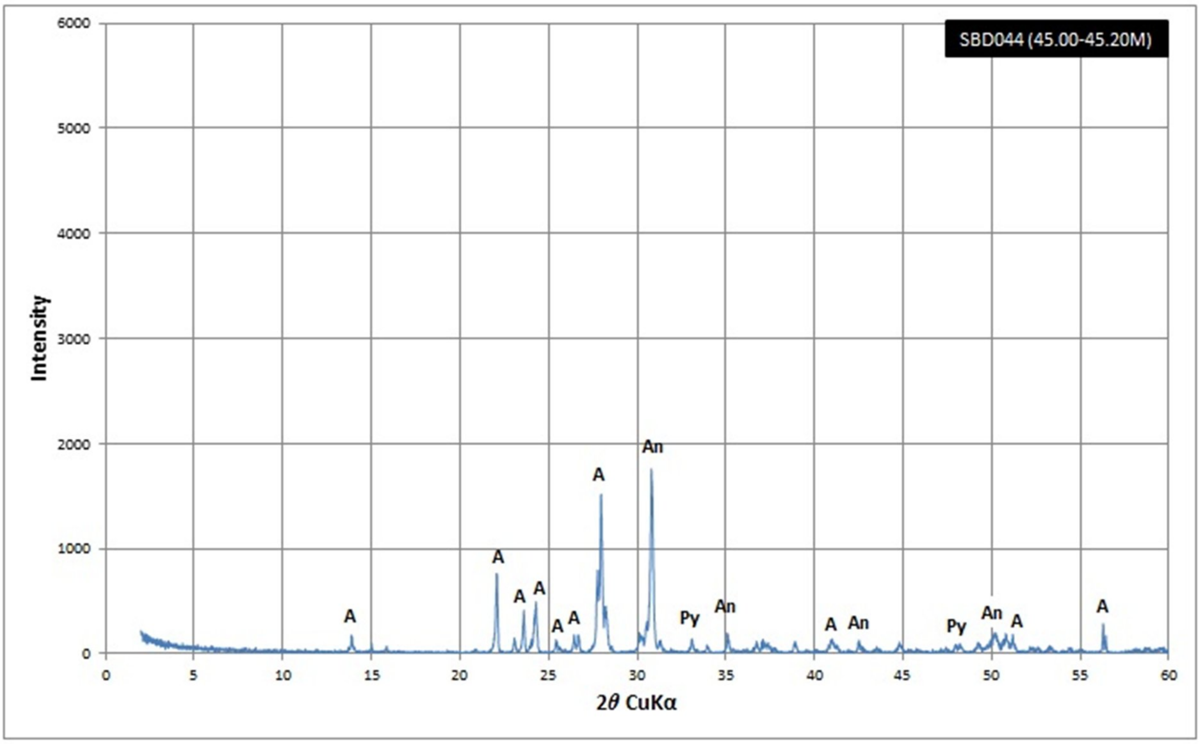

Abbreviation: A=albite; Q=quartz; An=ankerite; Py=pyrite.

3) SBD069-14

Breccia ore consist of altered (carbonate, quartz) meta-(chloritic) mudstone clast and matrix of quartz-carbonate±albite mineral that related to main stage vein (i). Pyrite occurred as dissemination in altered breccia clast and rarely in matrix.

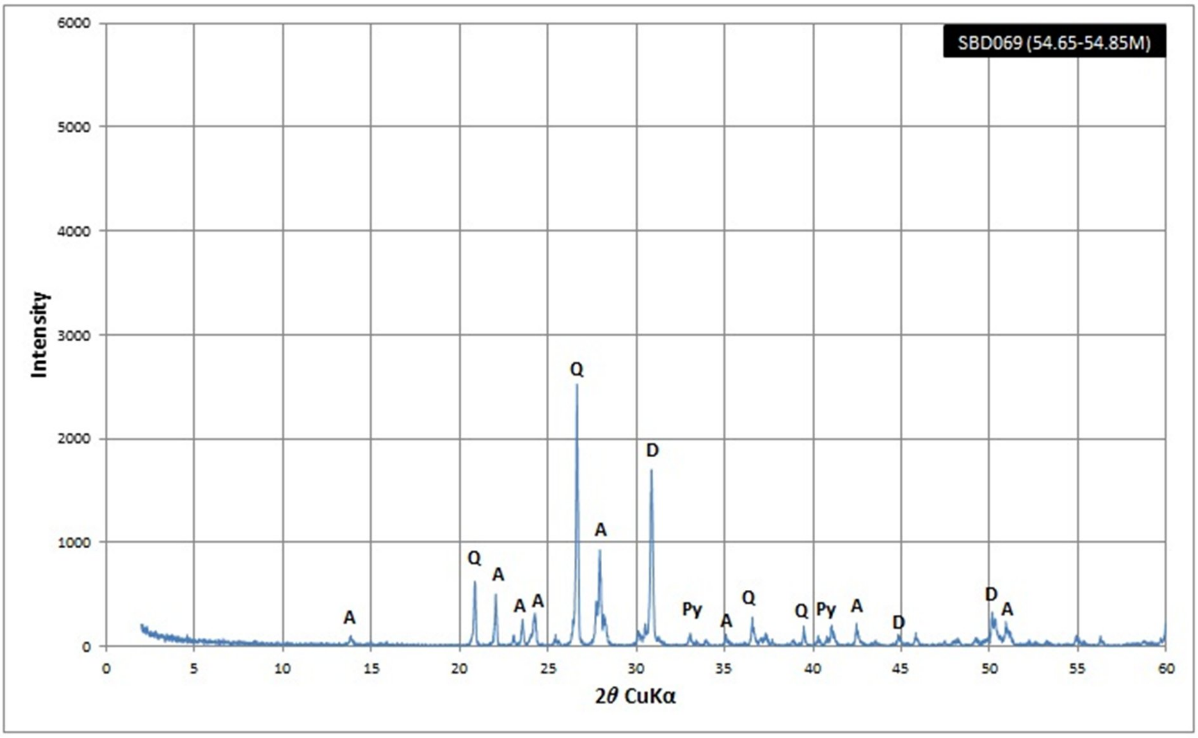

Abbreviation: A=albite; Q=quartz; An=ankerite; Py=pyrite; D=dolomite.

4) SBD072-09

Altered meta-sandstone with intensely stockwork of carbonate-quartz±albite veinlet.

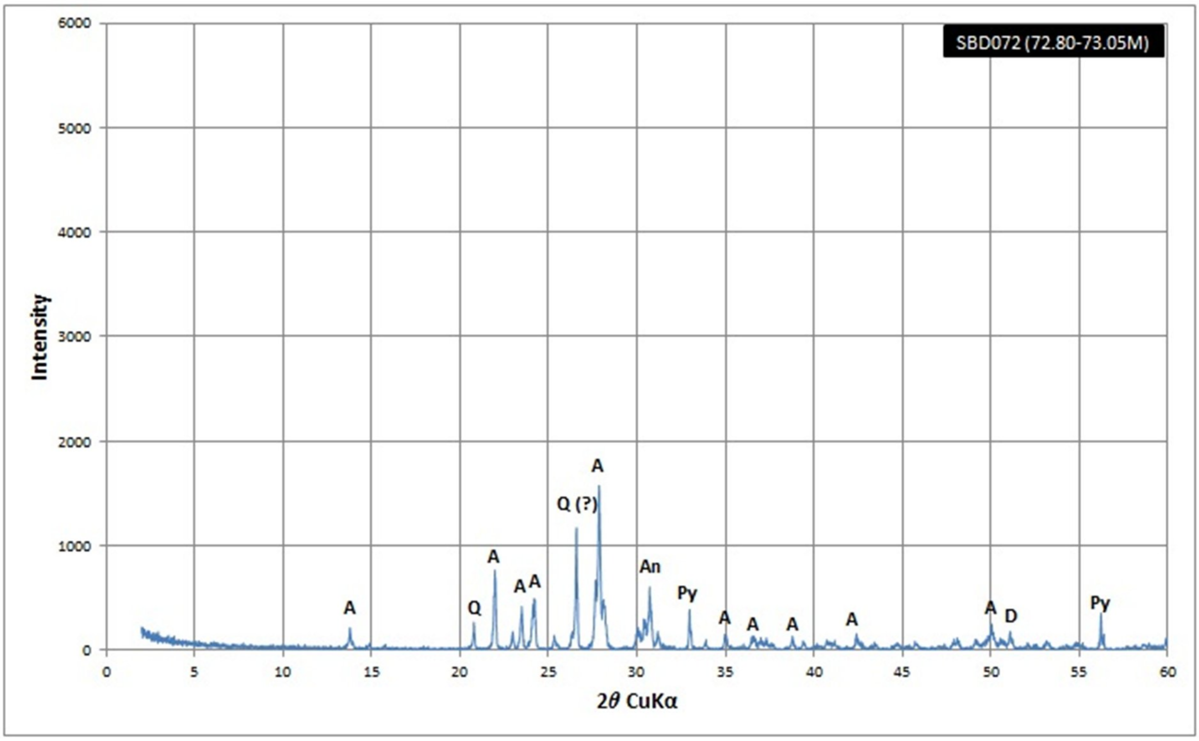

Abbreviation: A=albite; Q=quartz; An=ankerite; Py=pyrite; D=dolomite.

Appendix 5: EMPA analysis of trace element of pyrite.

Point	Point code	S wt%	Fe wt%	As ppm	Co ppm	Cu ppm	Ni ppm	Zn ppm	W ppm	Au ppm	Total wt%	Pyrite type	Description of analyzed spot
Detection limit		**0.05**	**0.02**	**143**	**79**	**242**	**80**	**296**	**237**	**194**			
Hostrocks													
SBD006 (66.75-66.85 m): phyllite, slightly silicified, related to main stage vein (iv, v).													
37	SBD006-15-1	53.524	46.206	460	680	640	nd	310	nd	nd	99.939	py2	cubic, euhedral, massive, core
38	SBD006-15-2	53.565	45.999	nd	1030	160	760	nd	nd	nd	99.759	py3	cubic, euhedral, porous, core
39	SBD006-15-3	53.246	45.796	nd	520	30	nd	nd	nd	nd	99.097	py3	cubic, euhedral, porous, edge/rim
46	SBD006-15-10	52.802	45.683	nd	790	380	930	80	nd	nd	98.703	py3	cubic, euhedral, porous, core
40	SBD006-15-4	53.448	44.753	nd	2620	nd	3240	100	600	nd	98.803	py4	cubic, euhedral, porous, core
41	SBD006-15-5	53.1	45.478	nd	1050	380	1260	170	nd	nd	98.864	py4	cubic, euhedral, porous, core
42	SBD006-15-6	53.264	46.1	nd	520	nd	10	nd	nd	nd	99.417	py4	cubic, subhedral, massive, rim
43	SBD006-15-7	53.414	45.702	nd	600	nd	100	nd	nd	nd	99.186	py4	cubic, subhedral, porous, core
SBD006 (103.95-104.00 m): meta-(chloritic) mudstone, unaltered.													
7	SBD006-20-1	52.673	45.797	510	550	900	190	580	nd	nd	98.743	py2	cubic, subhedral, massive, core
8	SBD006-20-2	52.872	45.901	nd	530	230	500	nd	nd	60	98.905	py2	cubic, euhedral, massive, core
9	SBD006-20-3	53.393	45.689	nd	490	210	260	510	nd	nd	99.229	py2	cubic, euhedral, massive, core
10	SBD006-20-4	52.925	46.028	60	660	1280	420	80	nd	nd	99.203	py2	aggregated, anhedral, massive, core
11	SBD006-20-5	53.036	46.505	nd	540	650	200	120	nd	nd	99.692	py2	cubic, subhedral, massive, core
16	SBD006-20-10	53.241	46.101	510	890	660	1110	500	nd	nd	99.709	py2	aggregated, anhedral, massive, core
12	SBD006-20-6	52.552	46.096	nd	670	400	2220	120	nd	nd	98.989	py3	cubic, subhedral, porous, core
13	SBD006-20-7	52.459	46.44	nd	620	560	170	540	nd	nd	99.088	py3	cubic, subhedral, porous, core
14	SBD006-20-8	52.633	45.563	nd	530	nd	2480	nd	nd	nd	98.497	py3	cubic, subhedral, porous, core
15	SBD006-20-9	52.745	46.573	nd	430	100	nd	290	nd	nd	99.4	py3	cubic, subhedral, porous, core
18	SBD006-20-12	53.437	46.133	nd	730	20	nd	510	nd	nd	99.696	py3	cubic, euhedral, porous, core
20	SBD006-20-14	52.969	46.008	10	460	160	30	310	600	nd	99.08	py3	cubic, subhedral, porous, core
17	SBD006-20-11	53.472	46.163	10	450	470	30	470	600	nd	99.784	py4	cubic, euhedral, porous, edge/rim
19	SBD006-20-13	52.759	46.61	nd	630	210	30	nd	4800	nd	99.504	py4	cubic, euhedral, porous, edge/rim
Alteration halo													
SBD053 (104.75-104.80 m): meta-(graphitic) mudstone, pyrite parallel to foliation, related to main stage vein (ii), carbonatization.													
35	SBD053-11-15	52.08	45.857	nd	610	nd	nd	nd	700	nd	98.005	py2	cubic, euhedral, less porous, edge/rim
24	SBD053-11-3	53.642	46.339	nd	680	310	2280	20	nd	nd	100.31	py3	cubic, euhedral, porous, core
25	SBD053-11-4	53.27	46.114	nd	1060	nd	3290	nd	nd	nd	99.819	py3	cubic, euhedral, porous, core

27	SBD053-11-6	53.548	46.523	nd	840	nd	1330	nd	nd	nd	100.288	py3	cubic, euhedral, porous, core
28	SBD053-11-7	53.77	46.703	nd	490	20	1040	nd	nd	nd	100.628	py3	cubic, euhedral, porous, core
32	SBD053-11-12	51.953	46.445	nd	860	600	670	nd	nd	nd	98.611	py3	cubic, euhedral, porous, core
36	SBD053-11-16	53.709	45.423	nd	480	540	170	nd	5000	nd	99.301	py3	cubic, anhedral, massive, core
22	SBD053-11-1	53.824	46.318	nd	790	490	930	nd	nd	nd	100.363	py4	cubic, euhedral, porous, core
23	SBD053-11-2	53.181	46.573	nd	710	150	220	60	nd	nd	99.868	py4	cubic, euhedral, less porous, edge/rim
26	SBD053-11-5	52.755	46.765	nd	390	nd	100	nd	nd	nd	99.569	py4	cubic, euhedral, massive, edge/rim
29	SBD053-11-8	53.021	45.975	nd	1320	570	2630	330	1500	nd	99.496	py4	cubic, euhedral, massive, edge/rim
30	SBD053-11-9	52.816	46.243	50	780	430	560	200	nd	nd	99.261	py4	cubic, euhedral, less porous, core
31	SBD053-11-11	53.329	45.965	nd	970	nd	1170	nd	nd	nd	99.508	py4	cubic, euhedral, massive, edge/rim
33	SBD053-11-13	53.682	45.472	nd	1030	nd	2120	nd	nd	nd	99.469	py4	cubic, euhedral, massive, edge/rim
34	SBD053-11-14	53.074	45.236	nd	1610	380	7240	nd	nd	nd	99.233	py4	cubic, euhedral, less porous, edge/rim

Ores

SBD069 (54.45-54.65 m): breccia ore, pyrite in silicified clast of breccia, rewlated to main stage vein (i?).

75	SBD069-14-13	52.091	45.025	200	2560	680	820	490	nd	nd	97.591	py1	aggregated, subhedral, core
83	SBD069-14-21	53.039	46.09	nd	860	nd	150	220	nd	nd	99.252	py1	aggregated, subhedral, core
79	SBD069-14-17	52.646	45.255	nd	670	190	2600	nd	2700	nd	98.274	py2	cubic, euhedral, massive, core
85	SBD069-14-23	53.083	46.459	nd	550	180	nd	nd	nd	nd	99.615	py2	cubic, eubhedral, less porous, core
66	SBD069-14-4	51.542	45.708	nd	650	470	210	300	nd	280	97.441	py3	cubic, anhedral, massive, core
70	SBD069-14-8	52.015	45.549	nd	620	nd	1800	nd	nd	nd	97.806	py3	cubic, subhedral, less porous, core
76	SBD069-14-14	53.781	45.53	nd	960	340	70	80	nd	nd	99.456	py3	cubic, eubhedral, less porous, core
81	SBD069-14-19	52.695	46.156	nd	630	130	nd	20	3600	nd	98.965	py3	cubic, subhedral, less porous, core
86	SBD069-14-24	53.49	46.225	nd	560	880	nd	nd	nd	nd	99.859	py3	cubic, euhedral, less porous, edge/rim
88	SBD069-14-26	52.598	46.742	30	500	390	640	90	nd	nd	99.505	py3	cubic, euhedral, less porous, edge/rim
89	SBD069-14-27	52.145	45.86	nd	650	180	6860	nd	nd	230	98.797	py3	cubic, eubhedral, less porous, core
90	SBD069-14-28	52.005	46.347	nd	570	nd	500	30	nd	nd	98.462	py3	cubic, euhedral, massive, edge/rim
63	SBD069-14-1	52.548	45.649	nd	680	620	1310	nd	nd	nd	98.458	py5	cubic, euhedral, massive, core
64	SBD069-14-2	52.918	46.088	nd	690	nd	nd	50	nd	nd	99.08	py5	cubic, euhedral, massive, core
65	SBD069-14-3	53.026	45.831	nd	640	110	nd	60	nd	nd	98.938	py5	cubic, anhedral, massive, core
67	SBD069-14-5	52.764	45.996	nd	630	nd	nd	320	nd	nd	98.855	py5	cubic, anhedral, massive, core
69	SBD069-14-7	52.884	45.479	nd	730	nd	nd	nd	nd	nd	98.436	py5	cubic, anhedral, massive, core
71	SBD069-14-9	53.236	45.965	nd	460	140	nd	nd	nd	nd	99.261	py5	cubic, subhedral, massive, edge/rim
73	SBD069-14-11	52.796	46.228	nd	420	530	550	nd	nd	nd	99.174	py5	cubic, euhedral, massive, core
80	SBD069-14-18	53.719	45.788	nd	620	nd	nd	120	1100	220	99.614	py5	cubic, euhedral, less porous, edge/rim

SBD109 (40.60-40.70 m): silicification-albitization, related to main stage vein (ii).

48	SBD109-01-2	53.524	45.318	nd	2710	50	7780	nd	1300	30	99.912	py3	iregular, subhedral, porous, core
49	SBD109-01-3	52.723	45.623	nd	680	nd	2760	nd	nd	nd	98.69	py3	iregular, subhedral, porous, edge/rim
51	SBD109-01-5	52.979	45.825	10	760	nd	nd	320	nd	nd	98.913	py3	cubic?, subhedral, porous, core
52	SBD109-01-6	53.315	45.939	nd	520	nd	nd	nd	2800	nd	99.334	py3	cubic?, subhedral, porous, core
54	SBD109-01-8	53.689	45.771	nd	510	nd	10	nd	nd	nd	99.512	py3	cubic, subhedral, porous, edge/rim
55	SBD109-01-9	53.509	46.007	nd	580	320	nd	30	nd	80	99.617	py3	iregular, anhedral, porous, core
56	SBD109-01-10	52.782	45.445	nd	580	nd	nd	nd	nd	nd	98.285	py3	cubic, subhedral, porous, core
57	SBD109-01-11	52.783	45.805	nd	540	80	180	80	900	nd	98.685	py3	iregular, subhedral, porous, core
58	SBD109-01-12	52.423	45.738	nd	630	nd	10	400	nd	nd	98.265	py3	iregular, subhedral, porous, core
59	SBD109-01-13	52.596	46.065	nd	870	nd	590	510	nd	nd	98.858	py3	iregular, subhedral, porous, core
61	SBD109-01-15	52.866	46.079	nd	590	480	900	240	nd	40	99.17	py3	iregular, anhedral, porous, core
62	SBD109-01-16	52.35	45.628	nd	700	150	4420	nd	nd	nd	98.505	py3	iregular, anhedral, massive, core
47	SBD109-01-1	52.729	45.863	60	830	350	920	10	nd	260	98.835	py4	iregular, subhedral, porous, edge/rim
50	SBD109-01-4	52.577	45.717	nd	510	170	260	360	nd	nd	98.424	py4	cubic?, subhedral, porous, edge/rim
53	SBD109-01-7	53.076	45.918	nd	550	nd	860	150	400	nd	99.154	py4	cubic?, subhedral, porous, edge/rim
60	SBD109-01-14	53.412	45.918	nd	870	180	3340	640	nd	nd	99.833	py4	iregular, anhedral, less porous, edge/rim